Hydrodynamics of the Yucatan peninsula carbonate aquifer: surface flow, inland propagation and mixing

by

Aaron Coutino

A thesis
presented to the University of Waterloo
in fulfillment of the
thesis requirement for the degree of
Doctor of Philosophy
in
Applied Mathematics

Waterloo, Ontario, Canada, 2021

Examining Committee Membership

The following served on the Examining Committee for this thesis. The decision of the Examining Committee is by majority vote.

External Examiner:	Adrian Werner Professor, College of Science and Engineering, Flinders University
Supervisor(s):	Marek Stastna Professor, Dept. of Applied Mathematics, University of Waterloo
Internal Member:	Mike Waite Assistant Professor, Dept. of Applied Mathematics, University of Waterloo
Internal Member:	Kevin Lamb Professor, Dept. of Applied Mathematics, University of Waterloo
Internal-External Member:	Christine Dow Assistant Professor, Dept. of Geography and Environmental Management, U

Author's Declaration

This thesis consists of material all of which I authored or co-authored: see Statement of Contributions included in the thesis. This is a true copy of the thesis, including any required final revisions, as accepted by my examiners.

I understand that my thesis may be made electronically available to the public.

Statement of contributions

Aaron Coutino is the sole author of Chapters 1, 4, and 5 which were written under the supervision of Prof. Marek Stastna. Chapter 4 will be used as the basis of manuscript which will be submitted for publication after thesis submission. Chapters 1 and 5 were not written for publication.

This thesis consists in part of two manuscripts written for publication. Chapter 2 has been published in the Journal of Hydrology. The publisher Elsevier allows for reproduction of the article in a thesis thus no copyright statement is required. Chapter 3 has been submitted for review in Geophysical Research Letters (GRL). Citations for Chapters 2 and 3 are:

Coutino, A., Stastna, M., and Reinhardt, E.G. "Interaction of mangrove surface coverage and groundwater inputs on the temperature and water level near Tulum, Quintana Roo, Mexico: Observations and modelling." Journal of Hydrology 583 (2020): 124566.

Coutino, A., Stastna, M., McNeill-Jewer, C.A., and Reinhardt, E.G. "Inland tidal oscillations within the Yucatan Peninsula." Geophysical Research Letters. Submitted. 2020GL090117.

Abstract

This thesis is a collection of three investigations into the hydrodynamics and hydrogeology of the Yucatan Peninsula, Mexico. The first investigation models potential mangrove-groundwater interactions as a box model. We use field sensor data to calculate various parameters and use the model to show that the proposed mangrove flooding mechanism can reproduce the observed effects. The second investigation reports on tidal oscillations detected within far inland water bodies of the Yucatan Peninsula. The tidal records were verified using null hypothesis testing. This result has major implications for the region as it indicates that previously thought to be isolated water bodies are in fact directly connected to the grater aquifer and thus the ocean. The proposed mechanism to allow such far in land oscillations is the presence of large fracture zones in the rock throughout the peninsula which may allow the pressure wave to easily propagate. The third investigation simulates a potential mixing event within the Yucatan aquifer, specifically within one of the many cave passages throughout the region. Parameters (Sc, 'fudge factor') were varied to better understand the dynamics of this system and how common approximations made for the sake of computational efficiency affect the dynamics. We found that while there is some leeway with the numerical choice of Schmidt number and 'fudge' factor (constant factor increasing all diffusivities), making large changes to these values leads to growing differences in energy calculations which are particularly important for mixing. Reductions in initial density difference (i.e. temperature profile) showed a significant dynamical difference compared to the base case. Particularly, differences in how the instability manifests and its effects on the density beyond the initial range created were observed. Together these studies help build a better understanding of the dynamics within the Yucatan aquifer particularly within the large caves and conduits where traditional porous media theory does not apply.

Acknowledgements

I would like to thank everyone who contributed to my work throughout my graduate career. I want to thank all my friends in the lab, both those who are still there and those who have moved on, especially David and Kris. I want to thank everyone at Zero Gravity and CINDAQ, all of the volunteers and divers who were instrumental in placing the sensors. I want to thank my colleagues and friends at McMaster who I never would have known without this project. I especially want to thank my fiance and best friend Dr. Chelsi who I met during this project. I want to give a special thanks to Marek for all his support these eight years, your support and friendship has made me the scientist I am today. I finally want to thank my parents for their love and support throughout all my education.

Table of Contents

List of Tables

List of Figures

Chapter 1

Introduction

Through increasing human development (Pelas, 2011; Garcia-Flores et al., 2008) and usage (i.e, consumption, pollution, alteration of catchments; (Novelo et al., 2009; Metcalfe et al., 2011; Mutchler et al., 2007; Herrera-Silveira et al., 2004)), the groundwater systems of the Yucatan Peninsula have come under increased stain. It is expected that in the coming decades further challenges will stem from anthropogenic climate change, including sea level rise and increased hurricane intensity and incidence (Werner and Simmons, 2009; Mendoza-González et al., 2013). Thus understanding the past and present dynamics of these coastal groundwater systems is of the utmost importance to ensure proper planning and protection of important natural resources such as drinking water. Modeling the groundwater system in the Yucatan Peninsula must account for a diversity of local conditions (e.g. vegetation types) and is further complicated by to the presence of large conduits within the subsurface (Bauer-Gottwein et al., 2011; Smart et al., 2006) as well as the vertical density stratification (due to variations in temperature and salinity) of the water column (González-Herrera et al., 2002; Gondwe et al., 2010; Kambesis and Coke, 2013; Werner et al., 2013). The dimensions of these conduits are on the order of meters to tens of meters (Bauer-Gottwein et al., 2011; Marin, 1990; González-Herrera et al., 2002; Charvet, 2009). At this scale, the flow is no longer in the low Reynolds number regime thereby breaking one of the foundational assumptions of Darcy's Law (Bair, 2016). Since the equations that govern both saturated and unsaturated flow are based on Darcy's Law (Pachepsky et al., 2003; Bair, 2016) they thus can not fully capture the dynamics within these regions. The full set of incompressible, stratified Navier-Stokes equations is necessary to correctly model the dynamics (Kundu et al., 2011). It is not computationally feasible to simulate the Navier-Stokes equations at the landscape scale due to the range of length scales that need to be resolved (Kundu et al., 2011). For these reasons methods other than traditional

groundwater modeling must be used to elucidate the dynamics of the groundwater system in this region. Three such approaches will be explored in this thesis.

1.1 Primary Science Questions

This thesis is what is what is commonly referred to as a 'sandwich' thesis, it is primarily composed of three publications: one which has been published, one which is currently in the final stages of revision, and one which is nearly ready to submit for publication.

The primary science questions motivating each chapter are as follows:

1. Can the observed lag between temperature response in the cave and the mangrove following significant rainfall be quantified? Does this support previous hypotheses?
2. How far inland does a significant tidal signal propagate?
3. How accurately can mixing in the cave passages be reasonably simulated? What approximations can be made without substantially changing the dynamics relevant to mixing?

These make contributions to

1. The representation of landscape variations in hydrological models.
2. Fundamental questions concerning the connectivity of the peninsula, and the assumption of the hydrological isolation of the inland waters used for paleoclimate reconstructions.
3. The ability of modern numerical models to represent mixing in the cave networks.

We will revisit exactly how much progress was achieved in the Conclusions and Future Work Chapter.

1.2 The Yucatan Peninsula

1.2.1 Geology and Geography

The heavily karstified limestone geology of the Yucatan Peninsula has a high permeability and porosity (14-23%) due to dissolution processes enhanced by sea level change associated with natural climate variability (Beddows et al., 2007; Smart et al., 2006; Bauer-Gottwein et al., 2011). As marine water (MaWM: marine water mass) intrudes from the coast and flows under the meteoric freshwater aquifer (MeWM: meteoric water mass), an interface forms between these water masses called the halocline. As the interface mixes it allows for enhanced dissolution of carbonate (Smart et al., 2006, 1988; Stoessell et al., 1989; Back et al., 1979) which over time creates conduits or caves. These processes have given rise to extensive coastal cave systems including the world's largest single cave (https://caves.org/project/qrss/). Close to the coast, these caves are the primary control on the flow allowing for increased transport orthogonal to the coast (Beddows et al., 2007; Beddows, 2004; Smart et al., 2006).

On a regional scale, fracture zones create areas of preferential groundwater flow and increased permeability (Bauer-Gottwein et al., 2011; Perry et al., 2003; González-Herrera et al., 2002). These fracture zones are presented in Figure 1.1. The 'Ring of Cenotes' is a regional fracture zone along the north-western coast of the peninsula formed along the Chicxulub impact site. The Sierrita de Ticul fracture zone is a north-east facing escarpment that bisects the peninsula from the Ring of Cenotes in the north-west to the Rio Hondo fracture zone in the south-east. The Holbox fracture zone runs roughly parallel to the coast from Cancun in the north to Tulum in the south. The Rio Hondo fracture zone located south of Holbox, forms parallel lines that connect Holbox and Sierrita de Ticul.

There are two dominant types of passage morphology: fissure passages and elliptical tubular passages. Fissure passages are generally taller than wider and form along a fracture line (Smart et al., 2006; Bauer-Gottwein et al., 2011). Elliptical tubular passages are generally wider than taller, and form through mixing zone dissolution (Smart et al., 2006). Currently, more than 1400 km of explored cave passages (http://caves.org/project/qrss/qrss.htm) are known within the state of Quintana Roo, with more being mapped and discovered every year (Kambesis and Coke, 2013).

A prominent feature of karstic landforms are sinkholes, regionally called 'cenotes', which are created when the roof of a cavern or cave passage breaks down to expose the subsurface (Smart et al., 2006; Gutiérrez et al., 2014).

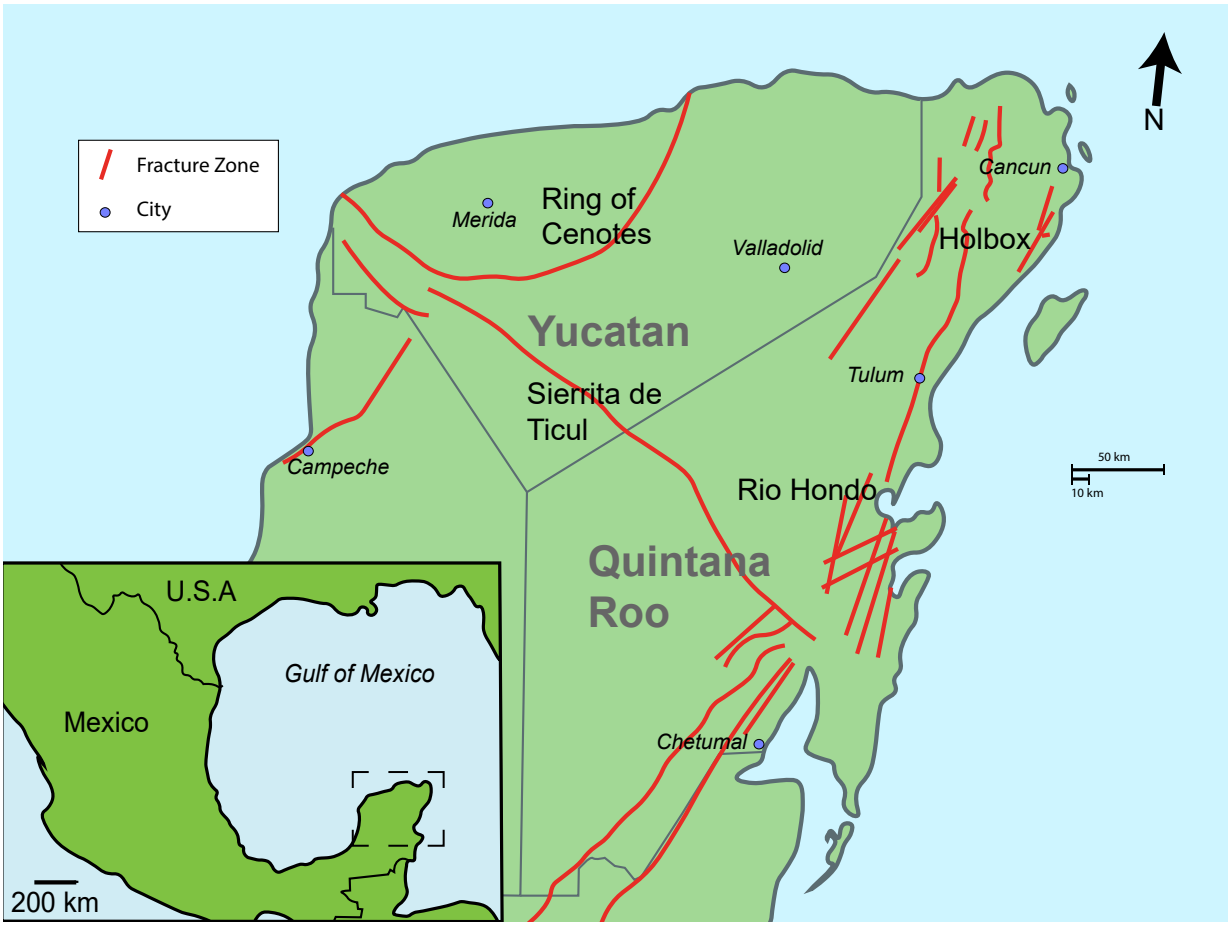

Figure 1.1: A map of the Yucatan Peninsula illustrating the different fracture zones throughout the region. The fracture zones have been taken from (Bauer-Gottwein et al., 2011).

1.2.2 Hydrology

The high porosity of the limestone (14-23%) (Beddows et al., 2007) results in very few surficial bodies of water, as rainfall quickly infiltrates to the aquifer and flows towards the coast (Emblanch et al., 2003; Stoessell, 1995; Beddows et al., 2007). Measurements of flow velocity in the cave passages typically yield values of 7 cm/s during the dry season and 10 cm/s during the rainy season, with peaks up to 30 cm/s during heavy rainfall events (Brankovits et al., 2018). The hydraulic conductivity (K) varies widely from 7×10^{-5} m/s within the limestone matrix, to 4×10^{-1} m/s in large conduits (Beddows et al., 2007;

Worthington et al., 2001).

The rainwater that percolates through the limestone forms a distinct freshwater mass (or MeWM) which is stratified on top of the marine water mass (MaWM) that intrudes from the coast and flows under the MeWM (González-Herrera et al., 2002; Gondwe et al., 2010; Kambesis and Coke, 2013; Werner et al., 2013). This marine flow is called seawater intrusion (SWI) and commonly occurs in coastal aquifers (Werner et al., 2013; Sebben et al., 2015). Where the two water masses meet an interface of mixed brackish water forms, called the halocline. This interface is generally thin (1-3 m), though it increases in vertical extent as it approaches the coast (Bauer-Gottwein et al., 2011). This is illustrated in Figure 1.2 which presents a schematic view of the the water masses. The vertical position of the halocline can change based on tides, seasonal dry periods, periods of intense rainfall or human activity. On longer time scales sea level changes may alter the geographic location of the coast. While the groundwater dynamics of relatively homogeneous geologies has been well studied, fractured and karstic aquifers remain a formidable challenge (Bakalowicz, 2005; Berkowitz, 2002). Numerical studies (Sebben et al., 2015) on fractured geology SWI have shown that the influence of fractures is likely mixed, with certain heterogeneities enhancing the extent of SWI while others act to reduce it. The authors found that vertical fractures in contact with the MaWM increase the width of the mixing zone as they allow mixing to not be constrained vertically, whereas inland in the MeWM vertical fractures have minimal impact on the seawater. This is because there is little vertical motion occurring. Horizontal fractures in the lower part of the aquifer force the MaWM seaward, whereas horizontal fractures in the MeWM enhance the wedge. Inclined fractures roughly parallel to the seawater-freshwater interface increase the landward extent of the MaWM and fractures perpendicular to the interface inhibit the wedge.

During intense rainfall events the halocline can increase in extent by mixing the surrounding MeWM and MaWM, terbey creating a mixed intermediate water mass (Coutino et al., 2017; Kovacs et al., 2017). Coutino et al. (2017), Kovacs et al. (2017) and Kovacs et al. (2018) showed that strong rainfall events (such as those due to hurricanes) result in mixing of the meteoric water mass (MeWM) with the marine water mass (MaWM), with subsequent re-stratification taking days to weeks to occur. Brankovits et al. (2018) examined water column mixing with regards to methane dynamics. They also reported increased mixing during the wet season compared to the dry season. Despite these preliminary streps, there are still many unknowns in regards to the dynamics of mixing, for example less intense storms have not been investigated. Since the cave networks span long distances, the terrain-type and land cover-type is expected to signficantly influence the hydrology. Given the prevalence of open cenotes with mangrove coverage in the coastal zone, it is expected that the mangroves may play a role in the dynamics of the upper aquifer

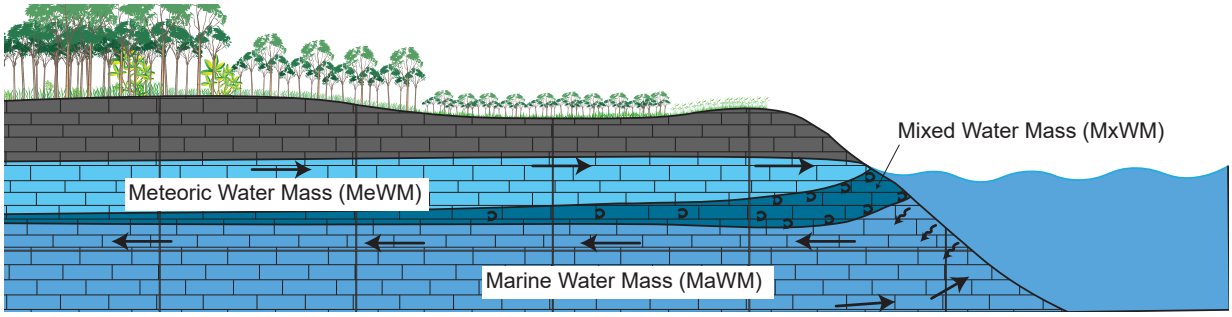

Figure 1.2: A schematic of the stratified aquifer. Due to the porosity of the limestone the marine water mass infiltrates under the meteoric water mass creating a stratified aquifer. The interface between the two water masses is generally thin inland but thickens as it approaches the coast.

(Collins et al., 2015; McNeill-Jewer et al., 2019). On a smaller scale, it is well known that rough walls will increase mixing within canonical pipe flow (Kundu et al., 2011), however the extent to which this effect occurs within the cave conduits has not been investigated.

Of particular relevance to the current research are coastal groundwater models that allow for seawater intrusion. While several groundwater models exist for coastal geographies (Jones et al., 2000; Sanford and Konikow, 1989), they typically assume that the region of interest has a homogeneous porosity (Hubbert, 1940; Wilson, 2005). One recent example of this approach is Levanon et al. (2017) who modeled sea-water intrusions in Israel. Their model used a combination of saturated flow and unsaturated flow to model the saline intrusion and freshwater lens respectively. However, due to the presence of fractures, and large scale cave networks, this model type is not directly applicable in the Yucatan Peninsula (Kambesis and Coke, 2013). One model which has shown promise within this region is MODFLOW-CFP (Conduit Flow Process) (Shoemaker et al., 2005). This extension of MODFLOW couples the groundwater model with a pipe network that represents the conduits. The coupling is a linear relationship between exchange flow rate and the difference in head between the MODFLOW cell and the pipe cell (Shoemaker et al., 2005). The model has previously been used for sub-regional scales within the Florida aquifer (Gallegos et al., 2013) which has a similar geology to the Yucatan Peninsula. More recently Martínez-Salvador et al. (2019) used MODFLOW-CFP to estimate pollutant residence time in the vicinity of Merida, Mexico. According to the authors this is the first time that a groundwater model has been applied to that region. It remains to be seen how well the model works in other parts of the peninsula.

1.2.3 Climate

The climate in the Yucatan Peninsula exhibits a bi-modal distribution of precipitation with peaks in June and September-October. The period between these peaks is a midsummer drought that is related to Sea Surface Temperature (SST) fluxes over the tropical Pacific (Magaña et al., 1999; Méndez and Magaña, 2010). During the rainy season, regional rainfall maxima can reach rates of up to 1500 mm/y, (Giannini et al., 2001; Bauer-Gottwein et al., 2011). Many climate phenomena have exhibited some level of influence on the Yucatan climate such as the Intertropical Convergence Zone (ITCZ), El Niño Southern Oscillation (ENSO), North Atlantic Oscillation (NAO), and Atlantic Multidecadal Oscillation (AMO) as well as changes in tropical North Atlantic SST and Sea Surface Salinity (Giannini et al., 2000; Magana et al., 2003; Wu et al., 2017). The ITCZ is a low pressure band along the trade winds that is composed of deep convective clouds (Lechleitner et al., 2017) located around 5 to 15 degrees above the equator (Gill, 1976). The southward migration of the ITCZ during El Niño years has been shown to be correlated to periods of drought in the Yucatan Peninsula (Magaña et al., 1999).

1.2.4 Field Sites

Six locations were studied as part of the current investigations. These locations have been highlighted in Figure 1.3. These locations were chosen either based on previous scientific work (i.e. Pac Chen, Chichancanab, Yax Chen (Krywy-Janzen et al., 2019; McNeill-Jewer et al., 2019; Hodell et al., 2005a)) or ease of access through El Centro Investigador del Sistema Acuífero de Quintana Roo A.C. (CINDAQ), our partner organization.

Yax Chen

Yax Chen (20°7'45.37"N, 87°28'7.86"W) is a 2.7 km long subsection of cave passage which is part of the larger Ox Bel Ha cave system. It is located approximately 9 km south of the city of Tulum, Quintana Roo (Figure 1.3) near the southern end of the Holbox fracture zone. The primary entrance to the cave is located within cenote Yax Chen, 200 m from the coast. At approximately 270 km long, Ox Bel Ha is the second largest underwater cave system in the world. The cave passages generally trend in a NW to SE in direction (https://caves.org/project/qrss/qrss.htm). Seven cenotes open along the primary cave passage. The passage is relatively shallow with a depth of approximately 8 m in the downstream portion and 10 m to 11 m in the upstream section. Flow within the passage

Figure 1.3: A satellite image of the Yucatan Peninsula with the field sites labeled.

is coast-wards with an average velocity of 10 cm/s increasing to 25 cm/s during heavy rainfall (Moore et al., 1992; Brankovits et al., 2018).

Pac Chen

Pac Chen (20°38'9.89"N, 87°35'12.55"W) Lake has an average depth of 16 m with an area of 0.04 km^2. It is located approximately 40 km inland from the Caribbean coast (Figure 1.3). The surface salinity of Pac Chen is 0.5 ppt, the limit of freshwater. Within the cenote, there is a minor vertical density change associated with the thermocline. The base of the lake contains a thick drape of organic sediment. Krywy-Janzen et al. (2019) reconstructed

the flooding history of Pac Chen using multiple sediment cores to show that it flooded and developed in accordance with rising sea level during the Late Holocene. The authors also measured water depth over 6 months and showed diurnal, and semi-diurnal tidal variations indicating a strong link to the aquifer, but the degree of connectivity between lake water and the aquifer has not been investigated (Krywy-Janzen et al., 2019).

Laguna Chichancanab

Chichancanab (19°52'25.84"N, 88°45'58.65"W) is a narrow lake located roughly in the middle of the peninsula, along the Sierrita de Ticul fault line and the intersection of Yucatan and Quintana Roo (Figure 1.3). The lake is roughly 15 km long and 0.7 km wide with an area of 5.4 km^2. It has an average depth of 4 meters and a max depth of 15 meters (Hodell et al., 2005a). Due to the high concentrations of gypsum and celestite the lake is saturated with dissolved salts (Perry et al., 2002). The high saturation of gypsum along with a thick drape of organic sediment along the bottom has made this location useful for the extraction of sediment cores to infer paleo-droughts (Hodell et al., 1995; Hodell, 2001; Hodell et al., 2005a). As decreases in rainfall result in more evaporation, the high saturation of gypsum eventually precipitates out of solution and is recorded in the sediment (Hodell et al., 1995; Hodell, 2001; Hodell et al., 2005a). One of the primary assumptions for this interpretation is that the drape of sediment seals the lake from the larger aquifer, forming a leaky or isolated water body allowing for gypsum to record droughts. However this assumption that the lakes are essentially closed to the larger aquifer has not been verified.

Sotuta de Peon

Sotuta de Peon (20°43'55.39"N, 89°34'28.89"W) is a small town approximately 25 km south of Merida (Figure 1.3). It is located approximately along the Ring of Cenotes. On the property of a Hacienda, there are several small cenotes that are used for freshwater and swimming. The closed cenote that was measured is located within a small cave with an average water depth of 3 m. There are no known large passages from this cenote, though small fractures can be seen throughout the cave.

Chukum

Cenote Chukum (20°43'15.27"N, 88°4'33.78"W) is a large pit cenote located within a tourist Hacienda. It is located approximately 15 km east of Valladolid (Figure 1.3), placing

it close to the western part of the Holbox fracture zone. The cenote has a diameter of 40 meters and a depth of over 20 meters. There appear to be some cave passages connected to the cenote near the bottom however they have not been explored and the their extent remains unknown. The cenote is mostly closed with a small skylight opening (https://www.haciendachukum.com/home/)

Laguna Campechen

Campechen (20°4'26.74"N, 87°29'14.85"W) is the large primary lagoon within the Sian Ka'an biosphere reserve (Figure 1.3). It covers an area of roughly 25 km^2 with an average depth of 2 meters (Padilla et al., 1993). The lagoon has several openings between the barrier islands where the brackish water of the lagoon is discharged. Gondwe et al. (2010) found evidence of fractures through out the biosphere reserve including a fracture that runs below the lagoon. There are numerous 'blue holes' that connect the lagoon directly to the cave passages.

1.3 Theory

As Chapters 2, 3, and 4 are written for publication in particular journals with specific limitations on the format and length; extra theoretical material that is useful in understanding the methods used in the publications will be explored in this section.

1.3.1 Saturated and Unsaturated Flow

The equations that govern the dynamics of saturated flow (flow where the media is fully saturated with liquid) are a simplification of the more general unsaturated flow (flow where the media has both liquid and gas phases), we will thus consider the latter. The equations for unsaturated flow are based on conservation of mass and Darcy's Law. Following Section 8.4 in Brutsaert (2008), if we assume a rigid porous media, that the fluid mass per unit volume is $\rho\theta$, where ρ (Kg/m^3) is the density and that the mass flux per unit area is given by ρq_i we can write conservation of mass as

$$\frac{\partial}{\partial x_i}\left(\rho q_i\right) = -\frac{\partial}{\partial t}\left(\rho\theta\right), \tag{1.1}$$

where q_i is the specific flux (m/s), θ is the volumetric water content and ρ is the constant fluid density. We will be adopting Einstein summation convention for the equations in this section. Darcy's Law is written as

$$q_i = -k_{ij}\frac{\partial H}{\partial x_j}, \tag{1.2}$$

where k_{ij} (m^2) is the permeability tensor and $H = h(\theta) + z$ (m) is the hydraulic head. The hydraulic gradient is defined as

$$\frac{\partial H}{\partial x_i} = \frac{\partial z}{\partial x_i} + \frac{1}{g\rho}\frac{\partial p}{\partial x_i}, \tag{1.3}$$

where z (m) is the vertical position of the free surface, p (Pa) is the gauge pressure, g (m/s^2) is acceleration due to gravity, and ρ is the fluid density. It is sometimes useful to replace the pressure gradient with a water content gradient to reformulate the equation as a diffusion equation, this is done by defining,

$$D_w = -k_{ij}\frac{\partial H}{\partial \theta}, \tag{1.4}$$

where D_w (m^2/s) is called the soil diffusivity. $h(\theta)$ is called the capillary head which is the head associated with capillary action in the porous media.

In mixed form, conservation of mass and Darcy's law can be combined to create Richards equation which reads,

$$\frac{\partial \theta}{\partial t} = \frac{\partial}{\partial x_i}\left(D_w\frac{\partial \theta}{\partial x_j}\right). \tag{1.5}$$

In saturation form Richards equation can be written as,

$$\frac{\partial \theta}{\partial t} = \frac{\partial}{\partial x_i}\left(\mathbf{k_{ij}}\frac{\partial H}{\partial x_j}\right). \tag{1.6}$$

This is the governing equation for unsaturated flow, for saturated flow we can further simplify by noting that the water content θ would remain constant if the medium was fully saturated and thus $\frac{\partial \theta}{\partial t} = 0$ so we are left with,

$$\frac{\partial}{\partial x_i}\left(\mathbf{k_{ij}}\frac{\partial h}{\partial x_j}\right) = 0. \tag{1.7}$$

The equation for saturated flow is a type of Laplace equation which can readily be solved depending on the form of $\mathbf{k_{ij}}$ (Haberman, 2004). Richards equation is significantly more complicated to solve than Laplace's equation as it is a degenerate elliptic-parabolic partial differential equation (PDE) (Farthing and Ogden, 2017). Specifically, unless storage effects are included the equation will change from parabolic to elliptic as the domain reaches saturation (List and Radu, 2016). This is further complicated by the equation's dependence on two highly nonlinear constitutive relations: the unsaturated hydraulic conductivity function $\mathbf{k_{ij}}$, and the capillary head function $h(\theta)$. Together this can lead to degeneracy in the equation as there is no guarantee of smoothness for these two relationships (Farthing and Ogden, 2017). These issues result in the unsaturated case of Richards equation being much more costly to solve numerically compared to saturated flow (Heath, 1983).

Unfortunately, two key assumptions for the groundwater theory outlined above are not applicable to the large conduits and fractures common throughout the Yucatan Peninsula. As discussed previously, seawater intrusion results in a significant density change vertically through the water column which cannot be accounted for in Richards equation. Another key assumption is that the Reynolds number is small which is not the case for flow in the larger fracture and conduits. The Reynolds number is defined as,

$$Re = \frac{UL}{\nu}, \tag{1.8}$$

where U is a typical velocity scale, L is a typical length scale and ν is the kinematic viscosity of the fluid. In the case of flow through porous media (such as the limestone in the Yucatan Peninsula) the typical length scale would be the size of the material pores which results in a low Reynolds number, however in the conduits and fractures the typical lengths are on the order of meters to tens of meters which results in significantly larger Reynolds numbers (Brutsaert, 2008).

A theoretical groundwater framework that includes conduits, was created by Loper and Eltayeb (2010). They derive a linear theory for conduit waves in the Woodville Karst Plain (WKP). A diagram of their theoretical framework is reproduced in Figure 1.4. For the following discussion we will be using the same notation as Loper and Eltayeb (2010). To derive their theory the authors assume that the turbulent volume flux Q in the conduit is related to the hydraulic gradient by

$$Q = -C\text{sgn}\left(\frac{\partial h}{\partial x}\right)\sqrt{|\frac{\partial h}{\partial x}|}. \tag{1.9}$$

sgn returns the sign of input, and C is the conveyance factor of the Darcy-Weisbach equation, defined as

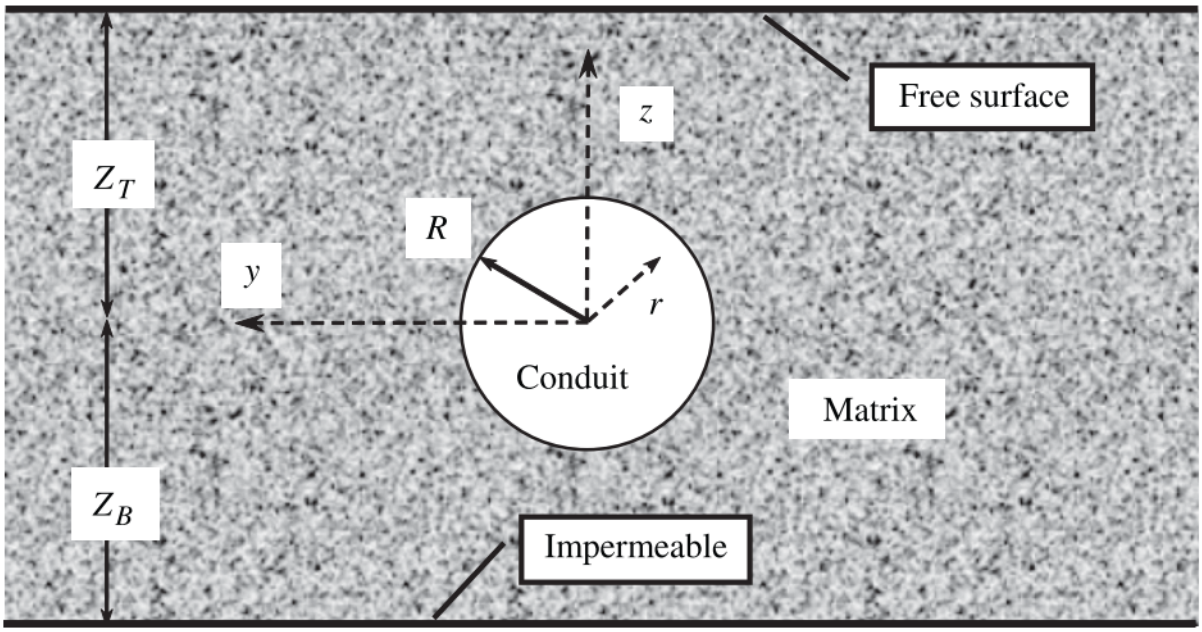

Figure 1.4: A diagram of the theoretical setup for the linear theory derived in Loper and Eltayeb (2010). This is Figure 3 from Loper and Eltayeb (2010).

$$C = 2\pi R^2 \sqrt{gR/f}, \tag{1.10}$$

R is the radius of the conduit, g is the acceleration due to gravity and f is the friction factor (determined from the Moody diagram (Jiménez, 2004)) which quantifies drag due to conduit wall roughness. Along the interface of the the conduit with the porous media conservation of flux requires that

$$\frac{\partial Q}{\partial x} = 2\pi K R \frac{\partial \overline{h}}{\partial r}, \tag{1.11}$$

where the overline denotes the azimuthal mean and K is the permeability tensor. Combining the previous three equations results in the following ODE,

$$\frac{\partial^2 h}{\partial x^2} + 2K \frac{\partial \overline{h}}{\partial r} \sqrt{\frac{f}{gR^3} \left| \frac{\partial h}{\partial x} \right|} = 0. \tag{1.12}$$

In order to use this equation the authors assume that $\left|\frac{\partial h}{\partial x}\right|$ is approximately constant which greatly simplifies the equation. Without this, due to the square root of the absolute value of $\left|\frac{\partial h}{\partial x}\right|$, the equation is not just nonlinear, its solutions are also nonunique. This is a fundamental problem for this framework as nonunique solutions imply that the theory cannot be predictive. Generally in physics the derivation of an equation with nonunique solutions points to an issue with the initial assumptions and that the problem was not initially well posed. Despite these issues, Loper and Eltayeb (2010) points to a possible avenue to incorporate conduits into the groundwater hydrology framework.

1.3.2 Navier-Stokes Equations

Within the large fractures and cave passages where the water is no longer confined within the substrate the governing equations would be the Navier-Stokes equations. The general version of these equations is valid for nearly all fluid flow, however we can make a few assumptions to simplify the equations. The first assumption is that the fluid is incompressible, this is valid for water (at most scales) as its compressibility is on the order of $10^{-10}\ Pa^{-1}$ for reasonable pressures (Fine and Millero, 1973). The second assumption is called the Boussinesq approximation which essentially states that density variations can be considered negligible except in the buoyancy (gravity) term. For specific conditions on when this approximation is valid please refer to Spiegel and Veronis (1960). With these two approximations made we can write the Navier-Stokes equations as (Kundu et al., 2011),

$$\frac{D\boldsymbol{u}}{Dt} = -\frac{1}{\rho_0}\nabla p - \frac{\rho g}{\rho_0}\hat{\boldsymbol{k}} + \nu\nabla^2\boldsymbol{u}, \tag{1.13}$$

$$\nabla \cdot \boldsymbol{u} = 0, \tag{1.14}$$

$$\frac{DT}{Dt} = \kappa_t \nabla^2 T, \tag{1.15}$$

$$\frac{DS}{Dt} = \kappa_s \nabla^2 S, \tag{1.16}$$

$$\rho = \rho(T, S), \tag{1.17}$$

where $\frac{D}{Dt} = \frac{\partial}{\partial t} + \boldsymbol{u}\cdot\nabla$ is the material derivative, $\boldsymbol{u}$ is the vector of velocities, ρ is the fluid density, ρ_0 is a constant reference density, p is the pressure, g is the acceleration due to gravity, ν is the kinematic viscosity, T is the fluid temperature, S is the fluid salinity, $\rho(T, s)$ is a non-linear equation of state, κ_t (κ_s) is the thermal (saline) diffusivity and the z axis is oriented vertically up. The equation of state used in our simulations is given below

$$\rho(T,S) = c_1 + c_2T + c_3S + c_4T^2 + c_5ST + c_6T^3 + c_7ST^2 \tag{1.18}$$

where $c_1 = -9.20601\times10^{-2}$, $c_2 = 5.10768\times10^{-2}$, $c_3 = 8.05999\times10^{-1}$, $c_4 = -7.40849\times10^{-3}$, $c_5 = -3.01036 \times 10^{-3}$, $c_6 = -3.32267 \times 10^{-5}$, and $c_7 = -3.21931 \times 10^{-5}$ (Brydon et al., 1999).

These equations are more general than Richards equation, however they are also significantly harder to compute numerically and would be essentially impossible to solve for the scales that Richards equation is typically used.

1.3.3 Time-series analysis

Time-series analysis is a major part of the study of any physical system for which measurements are available. In modern measurements of naturally occurring systems, measurements are often gathered over substantial periods of time and yield large data sets (10^6 or more). They thus include many irrelevant fluctuations, commonly grouped together as 'noise'. However, many physical processes are periodic, though the exact period may vary over time or may be on very long time-scales. The primary analysis method for periodic signals is Fourier analysis which decomposes signals into sinusoidal waves to extract period/frequency information (Stein and Shakarchi, 2011). However for signals where the periodicity changes through time, wavelet analysis is typically used as it intrinsically allow for period and temporal information to be extracted (Torrence and Compo, 1998). Wavelet analysis will be used in Chapter 2 to show the model's coherence with the sensor observations (e.g. of temperature), and will be used in Chapter 3 to calculate the lag times between water level measurements at various locations.

Fourier Analysis

The Fourier transform of some temporal record $f(t)$ is given by

$$\mathcal{F}[f] \equiv \hat{f}(\omega) = \int_{-\infty}^{\infty} f(t)e^{-i\omega t}dt, \tag{1.19}$$

where ω is the frequency, t is the time and i is the square-root of negative one (Stein and Shakarchi, 2011). The Fourier transform decomposes the function $f(t)$ into an infinite series of sine and cosine waves with differing frequencies. Provided that the function is sufficiently smooth this series will converge exactly to the original function. Two important

theorems from Fourier analysis are called the Parseval and Plancherel theorems (for proofs and additional information see standard references such as (Haberman, 2004) or (Guenther and Lee, 1988)).

Theorem 1.3.1 (Plancherel's theorem)**.** *If f and h are in $\mathbf{L^1}(\mathbb{R}) \bigcap \mathbf{L^2}(\mathbb{R})$ then,*

$$\int_{-\infty}^{\infty} f(t)h^*(t)dt = \frac{1}{2\pi}\int_{-\infty}^{\infty} \hat{f}(\omega)\hat{h}^*(\omega)d\omega, \tag{1.20}$$

where $*$ denotes the complex conjugate, $\wedge$ denotes the Fourier transform, $\mathbf{L^1}(\mathbb{R})$ denotes the space of Lebesgue integrable real functions and $\mathbf{L^2}(\mathbb{R})$ denotes the space of square integrable real functions.

Theorem 1.3.2 (Parseval's theorem)**.** *For $h = f$, that satisfies the property above, it follows that*

$$\int_{-\infty}^{\infty} |f(t)|^2 dt = \frac{1}{2\pi}\int_{-\infty}^{\infty} |\hat{f}(\omega)|^2 d\omega. \tag{1.21}$$

These two results are extremely powerful because they apply to any function h that satisfies the conditions of Plancherel's Theorem, which means that we can use Fourier transforms to analyse more exotic transforms (such as the wavelet transform). They also show us that we can relate the 'energy' (norm squared) of any function to its spectral power. These results will become important later when we consider computing the wavelet transform.

While this definition of the Fourier transform is useful in theory, in practice, data is not given by a continuous signal. Rather, it is measured at discrete times with a finite number of samples. Following (Haberman, 2004), if we assume a uniform sampling rate, and a spacing of Δt between our measurements, we can write a sample of some original function at time t as $f[t] = f[n\Delta t], n = 0...(N-1)$. Using the Dirac delta function we can write our discrete function as (Haberman, 2004)

$$f[t] = \sum_{n=0}^{N-1} f(n\Delta t)\delta(t - n\Delta t). \tag{1.22}$$

The Fourier transform of $\delta(t - n\Delta t)$ is $e^{-in\Delta t\omega}$ and so we can write the discrete Fourier transform as

$$\hat{f}[\omega] = \sum_{n=0}^{N-1} f(n\Delta t)e^{\frac{-i2\pi\omega n\Delta t}{N}}. \tag{1.23}$$

This process is very general and can be applied to all the continuous theory we will discuss. For this reason we will continue our discussion of the background theory using continuous notation but it can be easily extended to the discrete case.

The Fourier transform has been extremely influential throughout the development of modern physics, having been applied in areas from quantum theory to signal analysis (Stein and Shakarchi, 2011). However, a major drawback of the analysis is that it provides no information about the location of the frequencies in time. This effect is a result of f and $\hat{f}$ being conjugate variables, and as such must obey an uncertainty principle (Mallat, 1999). Under the Fourier transform each point in the frequency domain requires information about all points in the time domain, and vice-versa. Practically, this means that the more localized our function is in the time domain (the more precise it is) the broader its Fourier transform will be (less precise). This result also means that when we are in the Fourier domain we have zero information about the time localization and when we are in the time domain we have zero information about the frequency localization. For example consider Figure 1.5. In panels (a) and (b) we see two distinct signals that both result in an extremely similar spectrum (technically the imaginary components are different, but this is not shown in spectral plots), $|f(\omega)|$ (panels (c) and (d) respectively). This effect is a result of Fourier analysis not providing any time localization information. Since both frequencies of 10 seconds and 30 seconds appear in both signals (and with the same power) their spectra look the same. As a result of this effect, Fourier analysis is not adequate for extracting spectrum information from a signal when we would also like to know at what time a specific frequency is being activated. However, we can modify the traditional Fourier transform to acquire this information. The windowed Fourier transform, also called the Gabor transform (first introduced in (Gabor, 1946)), is similar to the traditional transform, only with the addition of a windowing function. Mathematically this is written as,

$$\hat{f}_{m,l}(\omega) = \int_{-\infty}^{\infty} f(t)g(t-m)e^{-i\omega lt}dt, \tag{1.24}$$

where $g(t)$ is the windowing function which is real, symmetric, has compact support, and is centred around 0. The windowing function allows the transform to measure the contributions of sine waves of frequency l, locally around the point m (Gabor, 1946). Traditionally, this window function and the sinusoidal components are combined and called the integration kernel, $g_{m,l}(t) \equiv g(t-m)e^{-itl}$. In relation to the uncertainty principle, the windowed Fourier transform can be thought of as losing certainty in the frequency domain but gaining some time localization information. Following the procedure in Chapter 4.1 of Mallat (1999), in order to examine the uncertainty in each domain, we must look at the properties of the power of the integration kernels, $|g_{m,l}|^2$ and $|\hat{g}_{m,l}|^2$. Our transform

no longer brings us to a one-dimensional domain, but we are now in a two-dimensional domain as a result of preserving some information from the time domain. Now consider a point in the time-frequency plane (m, l). Since our windowing function is guaranteed to have compact support, there is a specific 'width' of the function where it is non-negligible. The point (m, l) can only resolve times within this width, the same is true for frequency. To measure the extent to which each domain matters, we can calculate the variance for each domain centred around our point,

$$\sigma_t^2 = \int_{-\infty}^{\infty} (t-m)^2 |g_{m,l}(t)|^2 dt = \int_{-\infty}^{\infty} (t-m)^2 |g(t-m)|^2 dt, \tag{1.25}$$

and,

$$\sigma_\omega^2 = \int_{-\infty}^{\infty} (\omega-l)^2 |\hat{g}_{m,l}(\omega)|^2 d\omega = \int_{-\infty}^{\infty} (t-l)^2 |\hat{g}(\omega)|^2 d\omega. \tag{1.26}$$

Using the substitution $v = t - m$ and cancelling the exponential terms, we can see that the variances are independent of m and l. Thus we will have a tiling of similarly-sized boxes all across the time-frequency domain as we vary (m, l) (Mallat, 1999). This is the price that we must pay to obtain information about both time and frequency, there is uncertainty as to the exact values. A depiction of these 'Heisenberg Boxes' can be seen in Figure 1.6.

Wavelet Transform

The problem with the windowed Fourier transform is that we are limited by the choice of window, or more specifically by the maximum time-scale of our window (and correspondingly the maximum frequency-scale). Any frequency that is longer than our scales will be impossible to resolve. The wavelet transform, first developed in Grossmann and Morlet (1984), decomposes a signal into a wavelet basis, where a wavelet, ψ, is defined to have compact support, along with the following properties,

$$\int_{-\infty}^{\infty} \psi(t) dt = 0, \ ||\psi||^2 = 1. \tag{1.27}$$

Following the analysis in Chapter 4.3 of Mallat (1999) and Kumar and Foufoula-Georgiou (1994), there are two types of wavelets: real and complex. Real wavelets cannot provide amplitude and frequency information, but can easily pick out isolated peaks or discontinuities. These properties are often used to detect sharp transitions and thus predominantly used in image processing. Complex wavelets are similar to the windowed Fourier transform

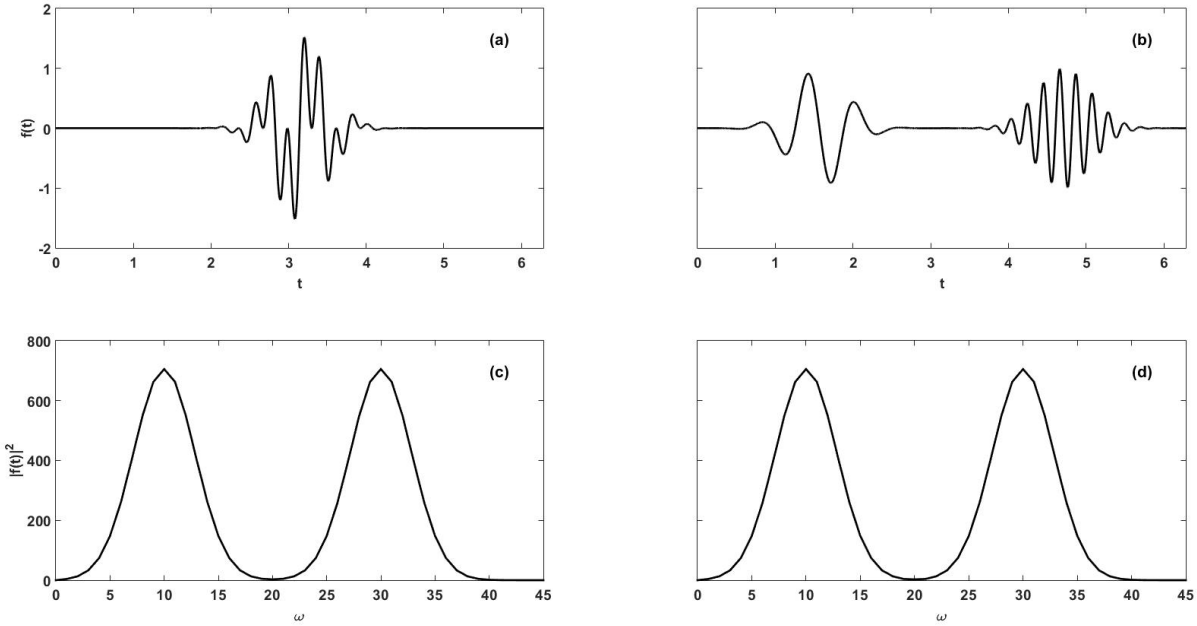

Figure 1.5: The signal in (a) is $\sin(10t)+\sin(30t)$ multiplied by a Gaussian envelope centred at π, while (b) is $\sin(10t)$ multiplied by the same Gaussian centred at $\pi/2$ plus $\sin(30t)$ multiplied by the same Gaussian centred at $3\pi/2$. Their spectra (c) and (d) respectively, appear almost identical. Since Fourier analysis does not provide any information about the time localization of the frequencies within a signal, cases where the same frequencies are active but at different times will result in the same spectra.

and are used to extract both time and frequency information. For this reason we will be focusing on complex analytic wavelets, since they are the type that will be used for signal processing. Once an original 'mother' wavelet is chosen, it is scaled and translated to form a 'dictionary' (not necessarily a basis) of 'daughter' wavelets. Mathematically, we can write this as

$$\left\{\psi_{u,s}(t) = \frac{1}{\sqrt{s}}\psi\left(\frac{t-u}{s}\right)\right\}_{u\in\mathbb{R},s>0}. \tag{1.28}$$

The continuous wavelet transform is defined as

$$\mathcal{W}[f(u,s)] = \langle f, \psi_{u,s}\rangle = \int_{-\infty}^{\infty} f(t)\frac{1}{\sqrt{s}}\psi^*\left(\frac{t-u}{s}\right)dt. \tag{1.29}$$

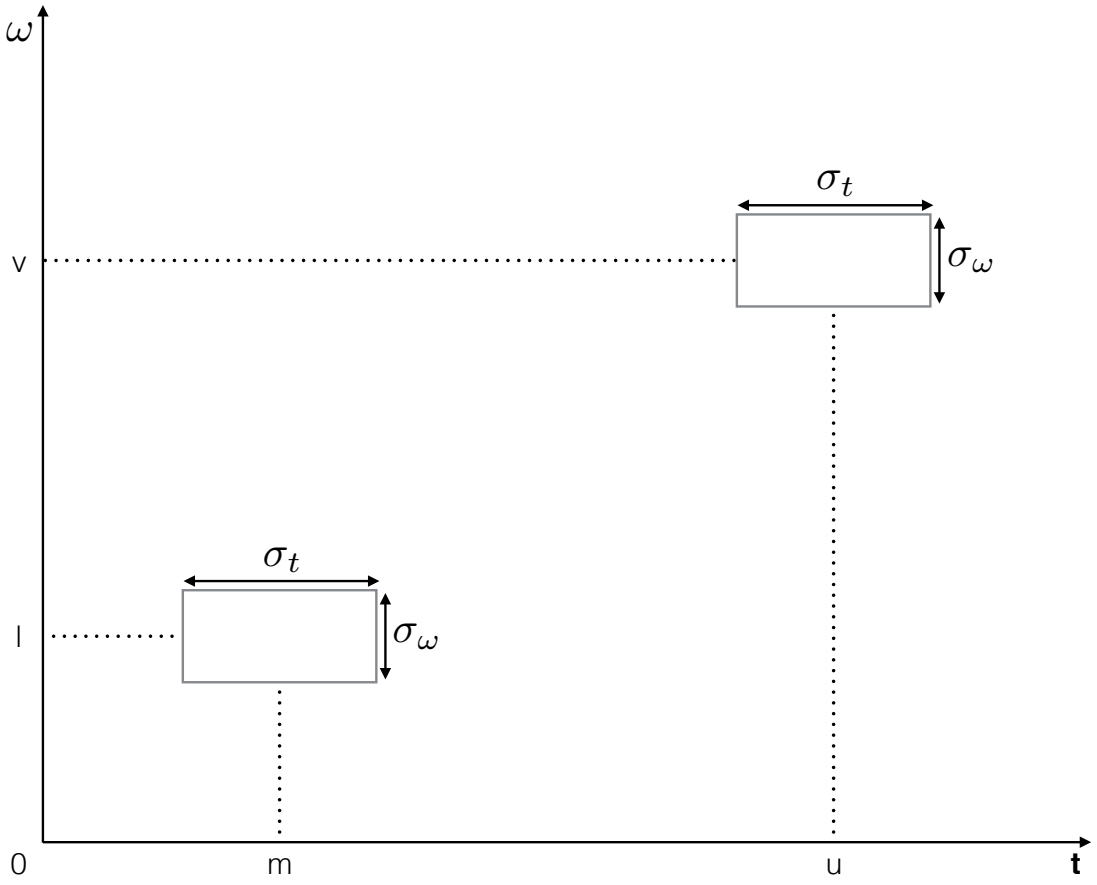

Figure 1.6: A depiction of the time-frequency (Heisenberg) boxes that tile the time-frequency plane. The time width of the box is defined by σ_t while the frequency width is defined by σ_ω. Since the variances are constant, the boxes form a symmetric tiling throughout the plane. This causes issues if we want to investigate low frequencies, which depend on much large time-scales than are resolved by the box.

The key difference and advantage of the wavelet transform over the windowed Fourier transform is in the time-frequency resolution. As for the windowed transform, we must investigate the variances of the integration kernel (in this case the wavelet), σ_t^2, and its conjugate variables variance, σ_ω^2. For the following calculations it will be useful to note that the Fourier transform of $\psi_{u,s}(t)$ is

$$\hat{\psi}_{u,s}(\omega) = \sqrt{s}\hat{\psi}\left(s\omega\right) e^{-i\omega u}. \tag{1.30}$$

This states that the $\hat{\psi}_{u,s}$ can be considered a stretched version of $\hat{\psi}$. Since ψ is centred around zero, $\psi_{u,s}$ is centred around u. Using the change of variable $v = \frac{t-u}{s}$ it can be easily shown that in the time domain we have that

$$\sigma_t^2(s) = \int_{-\infty}^{\infty} (t-u)^2 |\psi_{u,s}(t)|^2 dt = s^2\sigma_t^2, \tag{1.31}$$

with $\sigma_t^2 = \int_{-\infty}^{\infty} t^2|\psi(t)|^2 dt$. This result corresponds to a stretching of our Heisenberg box. Since $\int_{-\infty}^{\infty} \psi(t)dt = 0$, the centre of the spectrum (also called the centre of the passing band), η, is located at some point away from origin. Since the spectrum is even and negative values do not provide additional information, we will limit ourselves to the positive real line. We can find the centre of the passing band by calculating the first moment,

$$\eta = \frac{\int_0^{\infty} \omega|\hat{\psi}(\omega)|^2 d\omega}{\int_0^{\infty} |\hat{\psi}(\omega)|^2 d\omega}. \tag{1.32}$$

Using the results calculated earlier for the Fourier transform of $\psi_{u,v}(t)$, the centre of the frequency is therefore η/s, so we can calculate,

$$\sigma_\omega^2(s) = \frac{1}{2\pi}\int_0^{\infty} (\omega - \frac{\eta}{s})^2 |\hat{\psi}_{u,v}(\omega)|^2 d\omega = \frac{\sigma_\omega^2}{s^2}, \tag{1.33}$$

with $\sigma_\omega^2 = \int_0^{\infty}(\omega-\eta)^2|\hat{\psi}(t)|^2 d\omega$. These two results show that as we change our scale, we change the shape of the Heisenberg box and the frequency at which we are centred. This can also be thought of as our frequency controlling the scale: as we lower the frequency we increase the range of times considered, and the opposite is true as the frequency is increased. This results in a pyramid shaped tiling over the time-frequency domain which can be seen in Figure 1.7.

By systematically varying the scale, the wavelet transform allows us to tile the time-frequency plane much more efficiently than the windowed Fourier transform, and enables us to capture the entire range of frequencies of the original signal. This is the reason wavelet analysis was used in the following chapters over windowed Fourier analysis. Returning to the example first given in Figure 1.5, if we now use the wavelet analysis to compare the two different signals we can readily distinguish the two. In Figure 1.8 we present the same signals from Figure 1.5 where we have taken the wavelet spectrum of the time-series

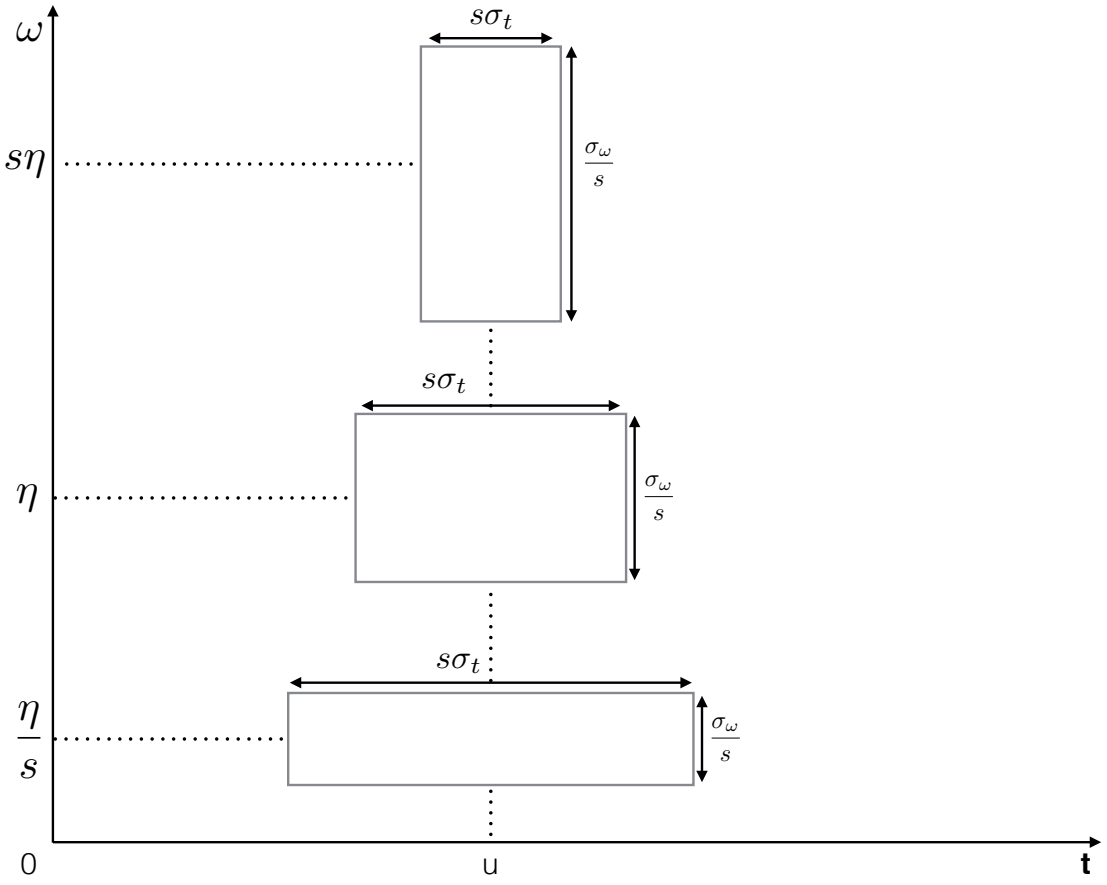

Figure 1.7: A depiction of the time-frequency (Heisenberg) boxes that tile the time-frequency plane using a complex wavelet. The time width of the box is defined by $s\sigma_t$ while the frequency width is defined by σ_ω/s. This means that as we change our scaling we also change our position along the frequency axis and the shape of the time-frequency boxes. This key feature enables sufficient temporal resolution to resolve the corresponding low frequency.

and presented a pseudocolor plot of the time-frequency domain. From this plot we can extract the same frequency information that we could from the Fourier spectrum, (though for wavelet plots it is customary to display the period), but we can also see the duration for which this signal is dominant. In the case of panels (a) and (c) both signals are dominant for the same duration, and are clearly distinct. However in panels (b) and (d) we can now

distinguish that in this case the frequencies peak at different times. This is the major gain for wavelet analysis, with the downside being that we have given up some accuracy in calculating the period (the spread of the peaks).

The changes in shape for each peak as we move to lower frequencies are due to the changing size of the time-frequency boxes and the large area of the peaks is due to our uncertainty explained above. The pseudocolor plot was interpolated which is why the time-frequency boxes are not visible due to resolution. Also note that the intensity of the smaller period was slightly less than the larger period. This is due to the energy scaling similarly to the support of the frequencies. The other contours shown in Figure 1.8 are important when presenting wavelet spectra and will be used throughout this work. The red diagonal line is called the 'cone-of-influence' and demarcates the region where boundary effects become important. Some daughter wavelets which 'fit' within the centre of time-series, when translated, would extend beyond the limits of the series, causing problems with the transform. Anything above the cone-of-influence has extended beyond boundaries and thus cannot be trusted to be correct. In general we will ignore anything beyond this boundary. The white contour lines indicate a 95% confidence interval for the signal when compared to a background distribution. In these example cases a white noise background was used. For the field data, and in general any physical phenomena, a red noise background is used. This contour helps to quickly identify regions of interest within the wavelet spectrum and provides evidence that the signal is not a random fluctuation.

Wavelet Coherence

Another useful technique using wavelets is the wavelet coherence. This allows two signals to be compared and indicates temporal regions where particular frequencies occur simultaneously. Wavelet coherence is a natural extension extension of spectral coherence which follows the same form but uses the cross and auto spectral densities rather than the cross and auto wavelet spectrum. Wavelet coherence is defined as,

$$R_n^2(s) = \frac{|S(s^{-1}W_n^{XY}(s))|^2}{S(s^{-1}|W_n^X(s)|^2) \cdot S(s^{-1}|W_n^Y(s)|^2)}, \tag{1.34}$$

where S is a smoothing operator, s is the scale and n is the position in time. This definition is extremely similar to the traditional correlation coefficient, which is why the wavelet coherence can be thought of as the localized correlation of the wavelet spectrum. The cross wavelet phase angle is simply $arg(W^{XY})$, this gives us the local relative phase angle between the two signals in time-frequency space (Grinsted et al., 2004).

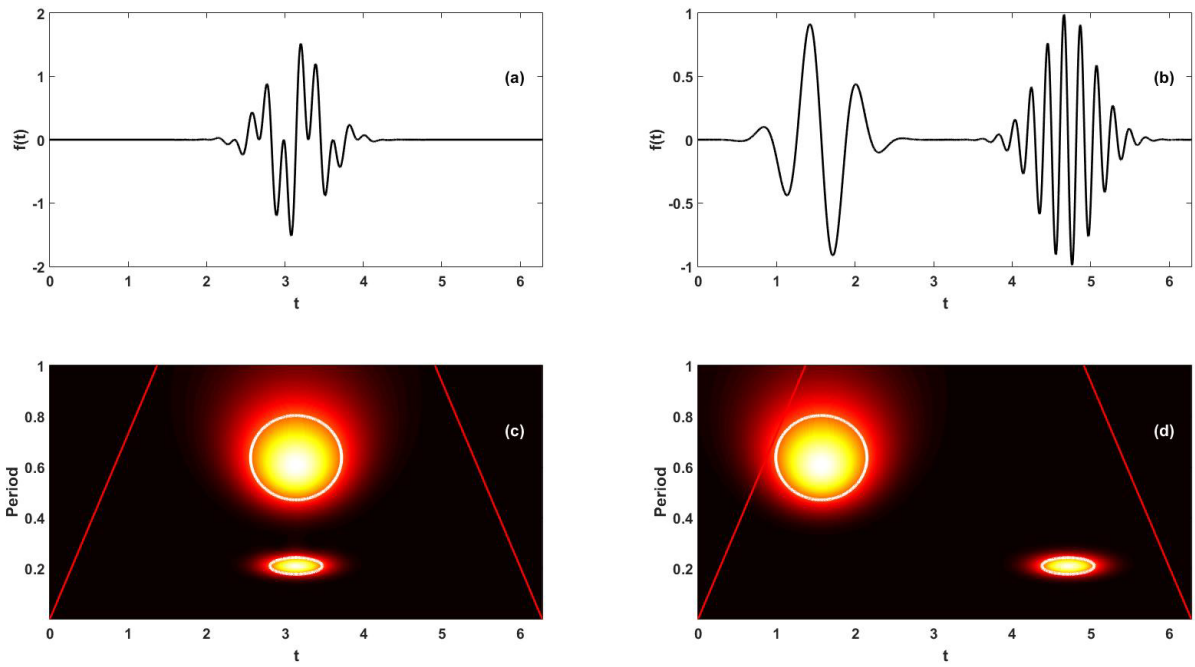

Figure 1.8: The wavelet spectrum for the same signals presented in Figure 1.5. It is important to note is that the y-axis is now given as the period thus the frequencies from Figure 1.5 are of period: $\frac{2\pi}{30}$ (0.2094) and $\frac{2\pi}{10}$ (0.6283). Due to the uncertainty from our time-frequency boxes, the specific frequencies are not exact but rather slightly spread in the time-frequency domain. However, they are sharply spiked at a specific frequency

To calculate the wavelet coherence we first begin by taking the continuous wavelet transform (CWT) (Torrence and Compo, 1998; Mallat, 1999; Kumar and Foufoula-Georgiou, 1994; Pinsky, 2009). For the wavelet coherence we will be following the procedure of the builtin MATLAB functions which are based off the work by (Grinsted et al., 2004). If we have the CWTs of two time series W^X and W^Y, we can compute the cross wavelet spectrum as $W^{XY} = W^X W^Y *$ where $*$ denotes the complex conjugate. Using these spectra we can create the wavelet coherence and the cross wavelet phase angle.

To illustrate these ideas more clearly Figure 1.9 shows the wavelet coherence of six relatively simple cases. In these plots, the arrows indicate the relative phase shift between the signals (rightward pointing arrow indicates in phase while leftward point indicates half period out of phase). The white dashed line indicates the cone-of-influence (COI) which denotes the area of the graph where edge effects (daugther wavelets extend beyond edges)

impact the results. The first panel compares a simple sine wave($\sin(t)$) with one that has been phase shifted by $\pi/2$ ($\sin(t - \pi/2)$). While there are differences around the edges of the plot, in general the two signals are coherent (mostly yellow) and the phase angles are all shifted by $\pi/2$. We see a similar story in the second panel which compares the sine wave to one shifted by $\pi/4$ ($\sin(t - \pi/4)$). In this case the edge effects do not appear to be a pronounced. The third panel compares a sine wave with a π shift ($\sin(t - \pi)$), and in this case there are no edge effects and the signal is completely coherent with the arrows pointing to the left. In the fourth panel we have increased the amplitude of the sine wave($A\sin(t)$) and as expected there is no difference in the coherence. In the fifth panel we have added white noise to the sine wave ($\sin(t) + \mathcal{N}(0, 1)$). In this case the lower periods (higher frequencies) are no longer coherent but the higher ones still are. For the final panel we have shifted the wave by $\pi/2$ and added noise ($\sin(t - \pi/2) + \mathcal{N}(0, 1)$). We see a similar response to that shown in the previous panel, with a lack of coherence at the lower periods, we also see a similar response at the high periods similar to the first panel. However in the region around the period of the wave we see a strong coherence and the phase correctly is shifted by $\pi/2$. Overall we can see that the arrows nicely indicate the phase shift between the two signals and that if we ignore effects near the edges the coherence clearly shows the periods and times that match.

The key advantage of using wavelets rather than spectral coherence is that we retain temporal information rather than solely having spectral information. This is highlighted in Figures 1.10 and Figure 1.11. In these cases we have packets that are localized in space unlike the sine wave. In Figure 1.10 one signal has three packets, one at 3, one at 6 and one at 9, the other signal only appears at 6. In the wavelet coherence we distinctly see coherence at the 6 second mark while nothing at 3 and 9. We also note that the phase arrows are pointing in the rightward direction since the signals are the same. Another feature we can notice, that is in fact a property of wavelets, is that since the peak is fairly narrow we have a spike downwards in the periods that are coherent. This is due to the type of mother wavelet used (Morlet) and this feature is commonly used in image processing for edge detection (Mallat, 1999). In Figure 1.11, we have a wide wave packet centred at 6 and a very small amplitude sine wave with the same period as the packet. A small amount of noise has also been added to the signals. We again can see that there is a very strong spike in coherence where we expect it centred at 6. We also see that the arrows are rightward facing as we would expect. We can also note the small amounts of coherence throughout the signals due to the noise. That we can have access to both temporal and spectral information from our analysis is the primary reason to use wavelet coherence over spectral coherence, especially for the time-series we consider which are intermittent.

Recently wavelet coherence has been extended to include significance testing for non-

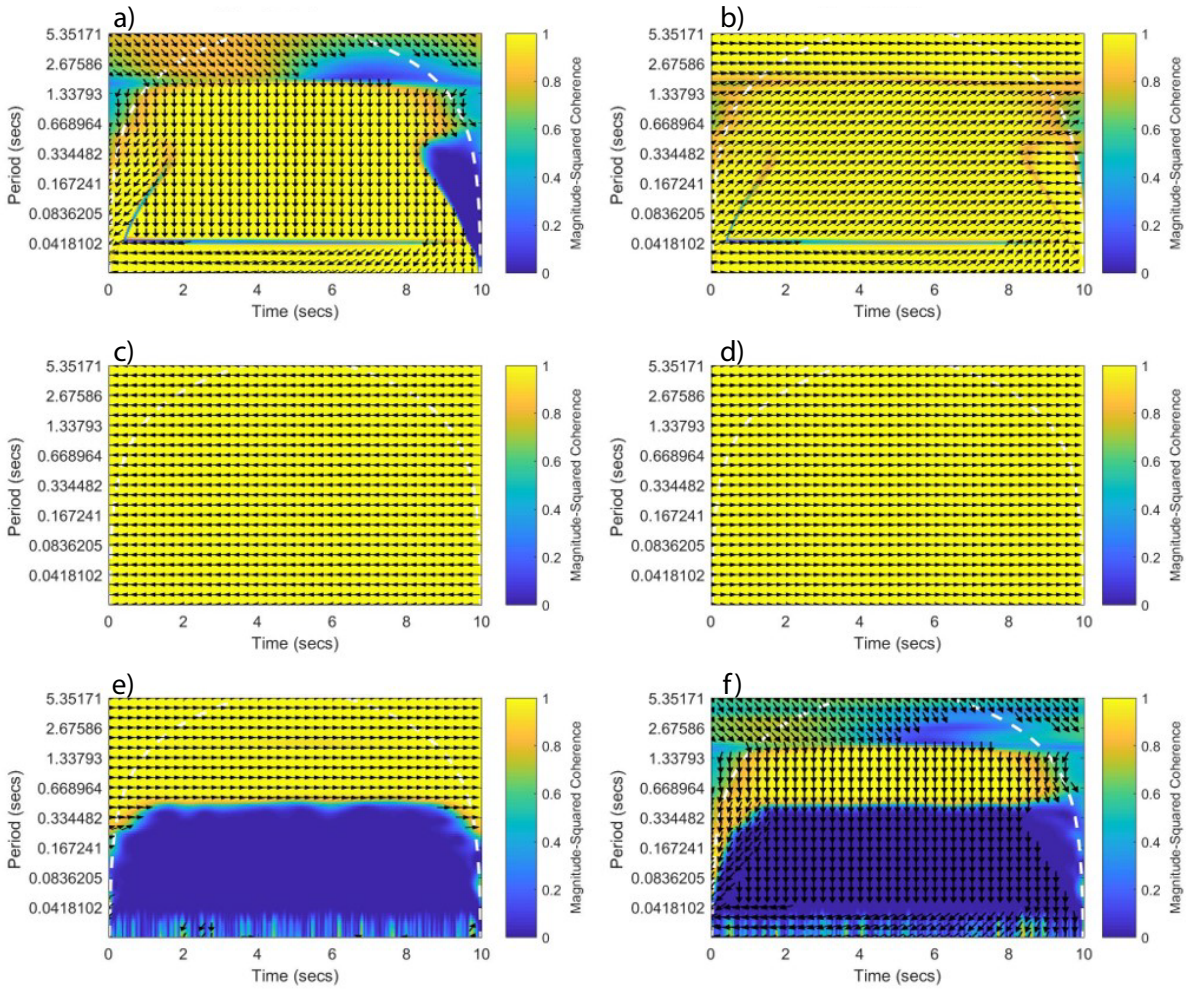

Figure 1.9: Panel (a) shows the wavelet coherence of two sine waves that are off-set by $\pi/2$. All phase angles are shifted by $\pi/2$. Panel (b) is the wavelet coherence of two sine waves off-set by $\pi/4$. Panel (c) is the wavelet coherence of two sine waves off-set by π. Panel (d) is the wavelet coherence of two sine waves with differing amplitudes. Panel (e) is the wavelet coherence of two sine waves where one has had white noise added to it. The final panel (f) is sine waves where one has white noise added and a $\pi/2$ phase shift.

stationary data-sets. (Chavez and Cazelles, 2019) developed an algorithm that uses wavelet

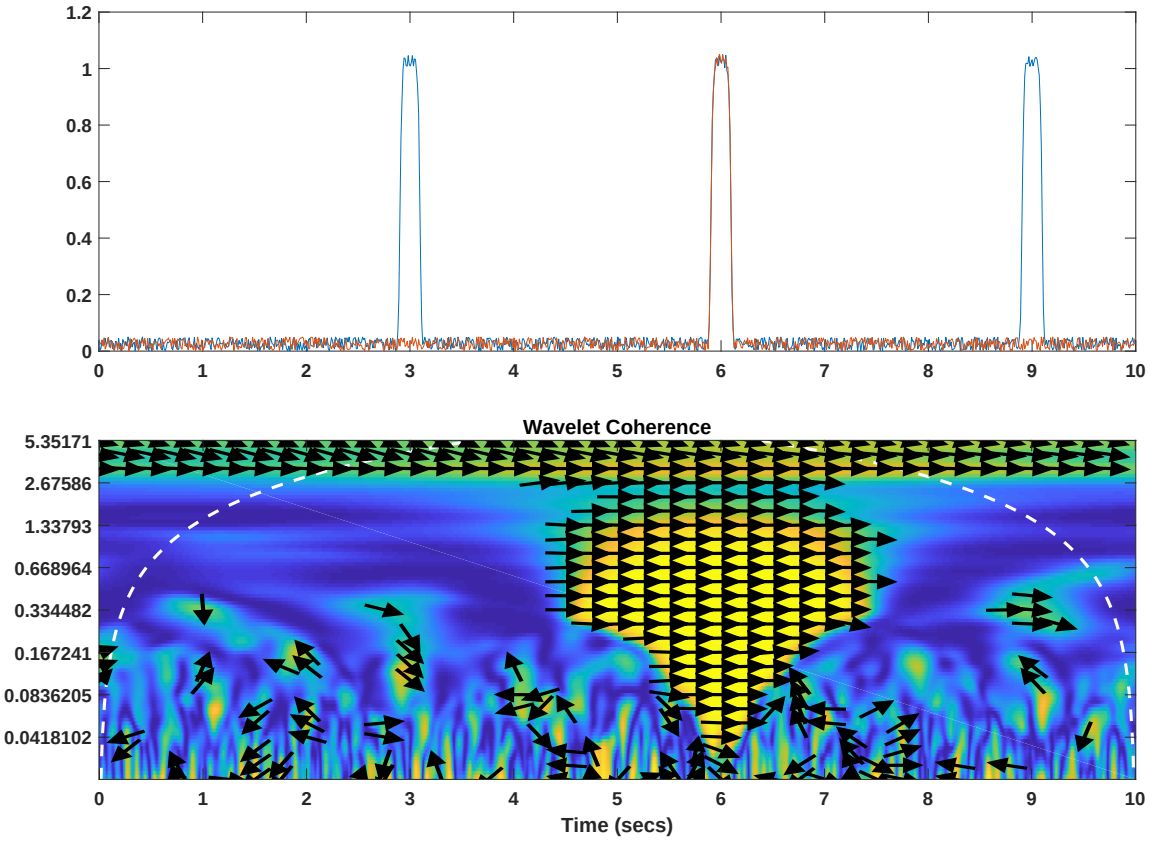

Figure 1.10: In the case of localized wave packets or events the wavelet coherence plot (bottom) only picks up the event where both signals (blude and red) occurred simultaneously (time 6; top).

coherence along with a surrogate data technique to properly compute non-stationary significance. Surrogate data techniques re-samples the original series without making any assumptions about the underlying generating process. Unfortunately the re-sampling method is extremely computationally inefficient and does not function on the very long time-series that were considered in this thesis (over 100 GB of RAM was required to use the method). However should the efficiency become increased this extension provides a general method for comparing non-stationary times-series which is extremely important given lack of sta-

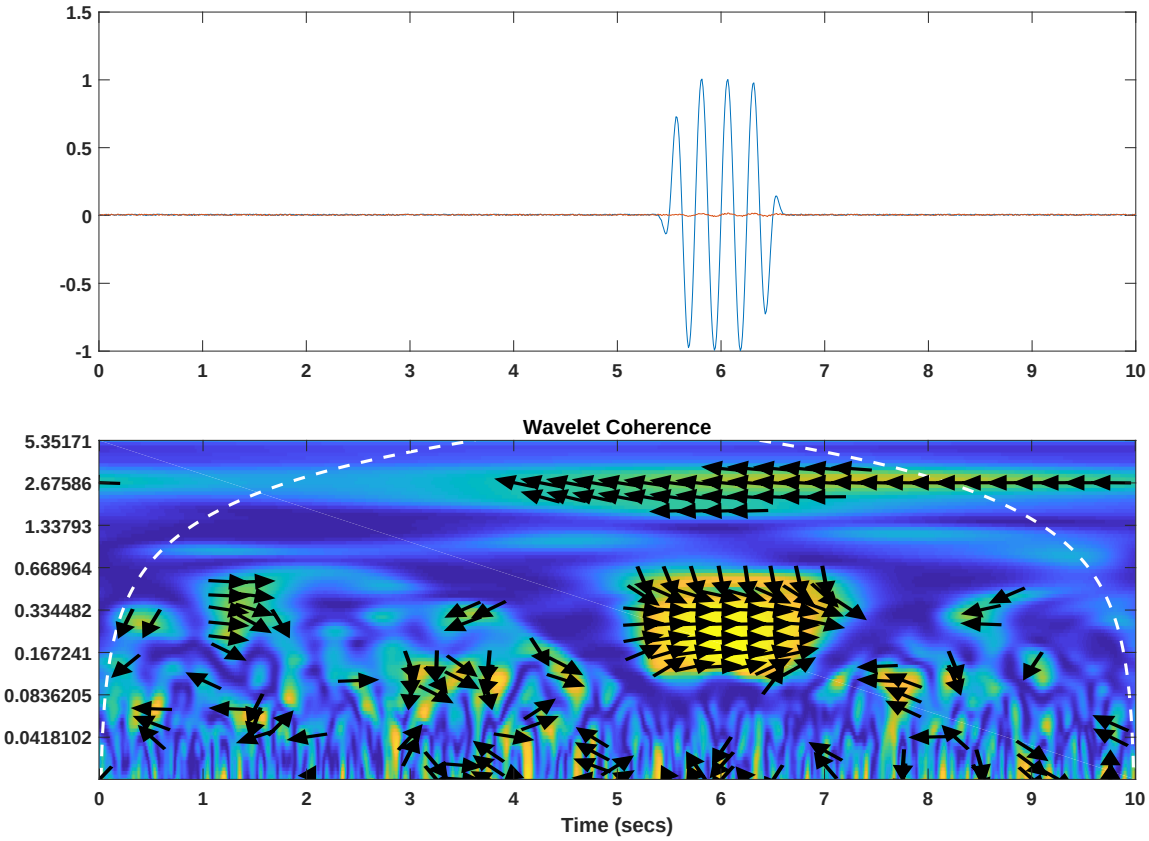

Figure 1.11: Even in the case where one of the signals considered has a very low amplitude (top, red), the wavelet coherence still picks up the periodicity and indicates coherence.

tionarity in environmental signals.

Null Hypothesis Testing

In spectral analysis it can be of interest if the largest peaks in the spectra of some observational measurements are a result of random processes or corresponds to real periodicity that may be hidden in the random noise. This question has two parts: choosing a null

spectra and computing the confidence levels. While white (uncorrelated) noise is commonly used by statisticians for hypothesis testing, most physical processes are positively correlated (Gilman et al., 1963). The simplest version of this is red noise, or an AR(1) (Autoregressive) process. Once a null spectra has been computed we can write (Wilks, 2007):

$$C_k^2 > \frac{S_0(f_k)}{\nu}\chi_\nu^2(1-\alpha) \tag{1.35}$$

where C_k^2 is the squared amplitude at frequency f_k, $S_0(f_k)$ is the null spectrum, ν is the degrees of freedom, and α is the confidence level. Picking an $\alpha = 0.95$, we can create a curve above which any peaks in our original spectra that surpass this level can be said to not be due to random processes.

1.4 Computation

The direct numerical simulations (DNS) in Chapter 5 were computed using the pseudospectral incompressible Navier Stokes equation solver (SPINS) (Subich et al., 2013). The solver uses a spectral approximation for the spatial derivatives implying that the accuracy of the simulation scales with the number of grid points (Trefethen, 2000), while time-stepping is implemented via a variable-step third order Adams-Bashforth method. The solver is fully-parallelized, and since the simulations in question do not require boundary topography, the solver is in its optimal scaling configuration allowing for efficient computation (see, Deepwell (2018) for details of scaling). This code has been extensively validated using standard physically relevant sample problems, as well as through continuous use in publication, especially for internal solitary waves, see (Olsthoorn et al., 2013; Soontiens et al., 2015; Grace et al., 2019; Xu and Stastna, 2019; Xu et al., 2019). Subich et al. (2013) validates the code using Kelvin-Helmholtz billows (e.g. growth rates), dipole-wall interactions and internal wave generation over topography.

An important aspect of analysing DNS is quantifying the evolution of energy components, and thereby understanding how the dynamics are manifest through transformations of energy. Traditional energy frameworks found in such works as Winters et al. (1995) break down energy into: kinetic energy, available potential energy, background potential energy, internal energy, and external energy (see Figure 1.12). The arrows indicate potential pathways for energy to move from one component to another. The colours indicate different pathways for the energy, red is the external pathway, green is the internal pathway and blue is the primary pathway. Kinetic energy is the energy associated with the velocity

of the fluid. Available potential energy is the portion of the potential energy available to be converted to kinetic energy. This is important as not all the potential energy can be transferred to other components; there is a minimum potential energy the system has. This is called the background potential energy. Internal energy is the energy not associated with motion, normally heat. External energy can act as a source or sink for the system, as the cases we will be considering do not have an external energy source, we can ignore the red energy pathway. For an example of how this energy framework can be used in an ocean setting, refer to Lamb and Nguyen (2009).

While this framework is very successful, the references above explicitly do not consider two component density systems nor a nonlinear equation of state. Recently this framework was extended to double diffusive systems with a two-component, linear equation of state by Middleton and Taylor (2020). The authors developed a criteria to quantify the transfer of energy from the background potential energy (BPE) to available potential energy (APE) based on the angle between the gradients of temperature and salinity, and the diffusivity ratios. Transfer of energy from BPE to APE is not possible in a single-component fluid with a linear equation of state. The finding that BPE can be converted into APE when double diffusive effects are present implies the interpretation of the APE from Winters et al. (1995) does not hold for a double-diffusive fluid (see dark blue arrow in Figure 1.12). In particular this complicates the definition of 'mixing efficiency' as it is commonly calculated Gregg et al. (2018). We will be following the methodology outlined in Winters et al. (1995) and Middleton and Taylor (2020) for calculating the BPE in Chapter 4. The total density field is sorted in 1D and then interpolated onto the z-grid. This interpolated density field is then repeated in each dimension to create a 3D array where each column is the sorted vector and used to calculate the BPE. This can then be subtracted from the total potential energy to get the APE.

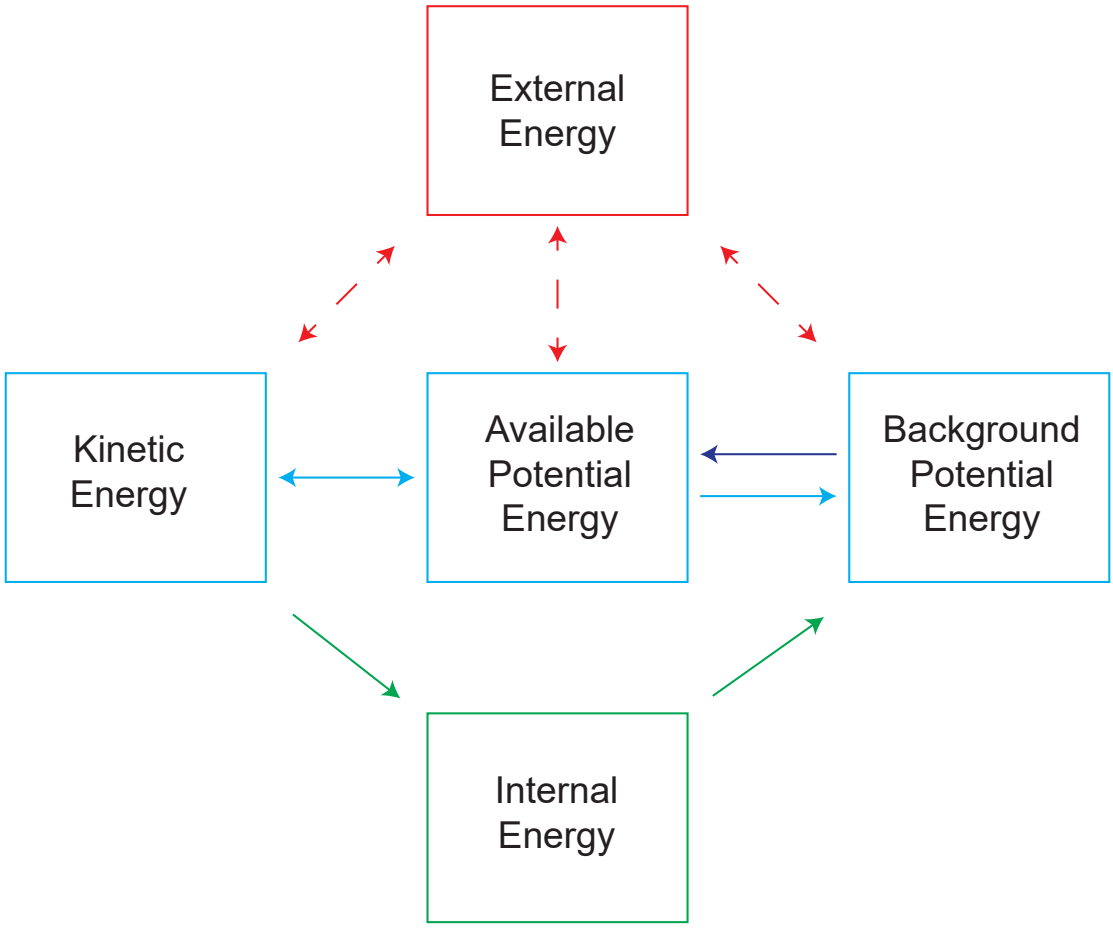

Figure 1.12: A diagram of the energy framework found in such works as Winters et al. (1995). Arrows indicate directions of possible energy transfer. The external energy is in Red to indicate that it will not be considered in this thesis.

Chapter 2

Interaction of mangrove surface coverage and groundwater inputs on the temperature and water level near Tulum, Quintana Roo, Mexico: Observations and modelling

2.1 Introduction

Despite containing the number one tourist destination in Mexico (Cancun), significant continuing development within the Mayan Riviera (Pelas, 2011; Garcia-Flores et al., 2008) and risks due to climate change (Mendoza-González et al., 2013), the hydrology of the Yucatan Peninsula remains incompletely understood. Previous research has shown that the dominant drivers of Yucatan aquifer dynamics are sea-level fluctuations and changes in the hydraulic head (Whitaker and Smart, 1990; Beddows et al., 2007), however, it is only recently that the impact of short-term intense rainfall events on the aquifer have been examined. Coutino et al. (2017), Kovacs et al. (2017) and Kovacs et al. (2018) showed that hurricane rainfall results in mixing of the meteoric water mass (MeWM) with the marine water mass (MaWM), with subsequent re-stratification taking days to weeks to occur. However, the mixing dynamics of less intense storms have not been investigated nor the role of surficial terrain on the hydrology. Given the prevalence of open cenotes with mangrove coverage in the coastal zone, it is expected that the mangroves may play a role

in the upper aquifer dynamics (Collins et al., 2015; McNeill-Jewer et al., 2019). This study documents the hydrology of a cave subsystem in coastal Quintana Roo over a two-year period to understand the effect of surficial vegetation on the aquifer in response to varying rainfall. A box model of the interactions between cenote/groundwater and mangrove water was developed and validated.

During the time period of May 2016 to May 2018 a series of depth, salinity and temperature sensors were positioned in the MeWM ($\sim$ 2 m depth) throughout the Yax Chen (which is part of the larger Ox Bel Ha) cave system (Fig. 2.1). The sensors recorded various rainfall events: Hurricane Earl in August 2016, Hurricane Franklin and Hurricane Harvey in August 2017, Hurricane Nate in September 2017 and Tropical Storm Philippe in October 2017. Over this period it was observed that rainfall events caused differing response in the temperature, water depth and salinity of the MeWM with rainfall amount and duration. Further differences were noted between groundwater areas with predominant mangrove coverage compared to forested terrain. Mangroves can trap and accumulate organic debris within their root systems and over time form extensive peat deposits that act as an aquitard which prevents or dampens downward flow of rainfall through the underlying karst (Twilley and Chen, 1998). Collins et al. (2015) and McNeill-Jewer et al. (2019) found large rainfalls raised the water table resulting in, mangrove water flowing into the cenote as water level decreased post rainfall. The mangrove water mass (MgWM) would be warmer, compared to the cenote water, due to a high residence time and heating due to direct solar radiation and its contact with the overlying warmer atmospheric air. Thus as this warmer water mass was draining into the cenotes it would cause an increase in groundwater temperatures. In contrast, the upland forest terrain would experience only a minimal change in groundwater temperature as the rainfall (which is cooler than the groundwater) would directly percolate through the overlying karst into the MeWM (see Figure 2.3). To test this hypothesis, a box model of the mangrove-cenote/groundwater interaction was created and validated using a flow switch for the mangroves if a certain water level is reached. When rain data from 2017 was used, the box model results matched the observations, validating the mangrove flooding hypothesis which was hypothesised in Collins et al. (2015) and McNeill-Jewer et al. (2019) based on prior sediment transport and accumulation data.

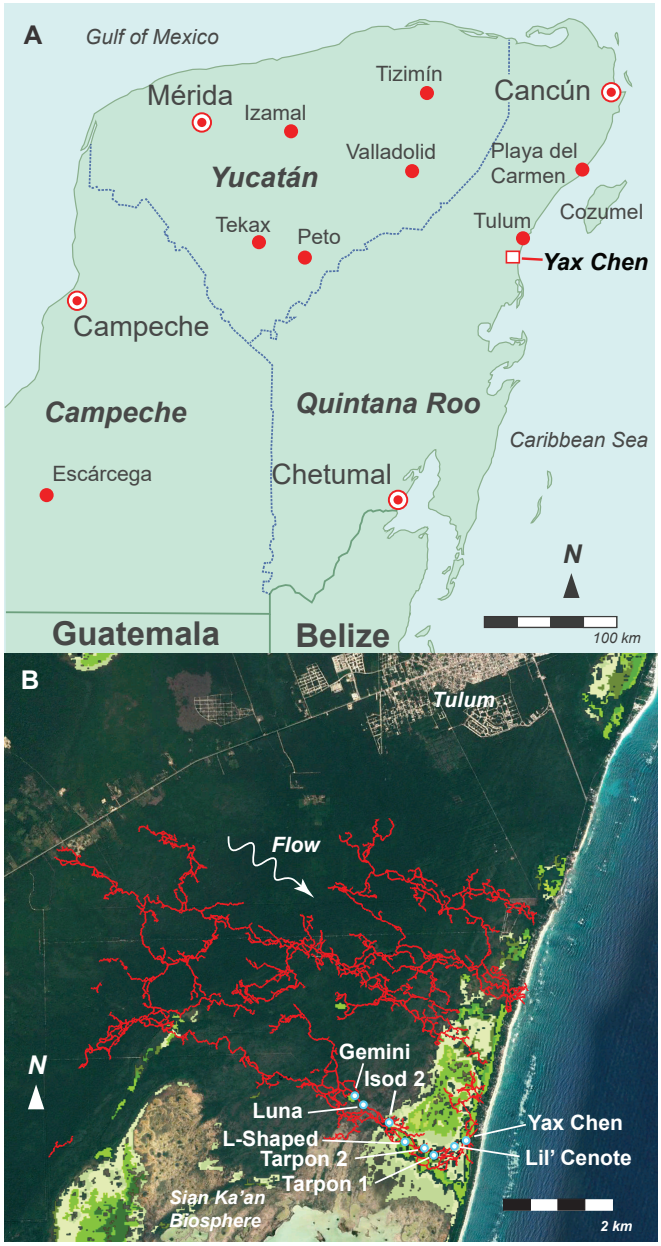

Figure 2.1: A map of the Yucatan Peninsula, Mexico (A). The study location, Yax Chen, is highlighted by a white and red square. Close up satellite image of the site highlights its position relative to the city of Tulum, the surrounding vegetation and the groundwater flow direction (B).

2.1.1 Yucatan Hydrogeology

The Yucatan Peninsula (which encompasses three Mexican states) is composed of Miocene to Late Pleistocene biogenic limestone with a total area of 165,000 km^2. The limestone has undergone intense dissolution through cycles of sea-level change creating a karst topography over much of the peninsula (Weidie, 1985).

A prominent feature of karstic landforms are sinkholes and cave systems, which are created through mixing zone dissolution (Ford and Williams, 2013; Smart et al., 2006). The dominant class of sinkhole in the eastern part of the Yucatan Peninsula consists of points of bedrock collapse, regionally called cenotes, that form when the roof of a cavern or cave passage breaks down to expose the subsurface (Smart et al., 2006; Gutiérrez et al., 2014). Cenotes have also been further classified based on water residence time. Lotic cenotes are well connected with the groundwater and have low residence times, compared to lentic cenotes which are also connected but have slow flow and long residence times (Schmitter-Soto et al., 2002).There are two dominant types of passage morphology: fissure passages and elliptical tubular passages (Smart et al., 2006). Currently, more than 1400 km of explored cave passages (`http://caves.org/project/qrss/qrss.htm`) are known within the state of Quintana Roo, with more being mapped and discovered every year (Kambesis and Coke, 2013). Additionally, the high porosity of this limestone (14-23%) (Beddows et al., 2007) results in no surficial rivers, as rainfall quickly infiltrates to the aquifer and flows towards the coast (Emblanch et al., 2003; Stoessell, 1995; Beddows et al., 2007). Measurements of flow velocity in the cave passages typically have values of 7 cm/s during the dry season and 10 cm/s during the rainy season, with peaks up to 30 cm/s during heavy rainfall events (Brankovits et al., 2018). On a large regional scale, fracture zones create directions of preferential groundwater flow parallel to the coast (Bauer-Gottwein et al., 2011).

The aquifer is stratified with a MeWM located above an underlying MaWM. Though there can be variation throughout the region, on average the rain-derived MeWM has a lower temperature (25-30 °C) and lower salinity (1 to 10 ppt) than the MaWM (26 to 28 °C, and 35 ppt, respectively) (Stoessell and Coke, 2006; Kovacs et al., 2017; Coutino et al., 2017). In areas of open water such as lakes or cenotes, a thermocline is formed in the upper MeWM (Beddows, 2004). The temperature can increase from 27 °C in the lower MeWM to 30 °C near the surface. The interface between the water masses is a mixed brackish layer called the halocline (or mixing zone) that while generally thin, increases in vertical extent as it approaches the coast (Bauer-Gottwein et al., 2011). This stratification is well-documented for many coastal systems especially given a porous coastal geology (Cooper et al., 1964), though the hydrodynamics of this system are still not fully understood.

Specifically, while several groundwater models exist for coastal-ocean geographies (Jones et al., 2000; Sanford and Konikow, 1989), they typically assume that the region of interest has a homogeneous porosity (Hubbert, 1940; Wilson, 2005). However, due to the presence of the fractures, and in particular the large scale cave networks, this is not the case in the Yucatan Peninsula (Kambesis and Coke, 2013). The porous geology and cave networks also allow for propagation of tides further inland than is typically expected with tides, however the overall amplitude is relatively low at 0.5 cm near the coast (Beddows, 2004).

While generally understood to occur and contribute to water quality changes (Beddows et al., 2007), the specifics of mixing between the MaWM and MeWM have only recently been investigated. Kovacs et al. (2017) and Coutino et al. (2017) demonstrate the large impact that hurricanes have on the water column, specifically focusing on the Yax Chen cave system (part of the larger Ox Bel Ha system; Fig. 2.1), while Brankovits et al. (2018) has examined water column mixing with regards to methane dynamics at a more inland portion of the Ox Bel Ha system. Brankovits et al. (2018) also reported increased mixing during the wet season compared to the dry season.

2.1.2 Yucatan Climate

The climate of the Yucatan Peninsula is strongly tied to the position of the Intertropical Convergence Zone (ITCZ), the concentrated band of low pressure located between 5 to 15 degrees above the equator, which is characterized by large scale thunderstorms and precipitation (Gill, 1976). The Yucatan Peninsula is located directly under the yearly migration path of the ITCZ, thus when it moves overhead during the summer wet season, large scale precipitation occurs throughout the region. To highlight this, during the wet season (May–October) in 2017, the Yucatan Peninsula (the states of Quintana Roo, Yucatan and Campeche) had an average monthly precipitation of 552 mm/month, while during the dry season (November–April) average monthly precipitation was 103 mm/month (https://smn.cna.gob.mx/es/climatologia/temperaturas-y-lluvias/resumenes-mensuales-de-temperaturas-y-lluvias). Additionally, between June and November numerous hurricanes form in the Atlantic Ocean and bring additional rainfall (peaks up to 300 mm/day) to the region.

2.1.3 Box Models

Box models have a long history in geophysics (Stommel, 1961; Budyko, 1969; Stastna and Peltier, 2007). Box models are simple, and do not seek to fully represent a complicated

system such as the climate. Instead they use a reduced number of variables and interactions to form and test hypotheses or explain field observations.

One classical example of a box model is the Stommel (1961) two box model of the Atlantic thermohaline circulation. In the model, the North Atlantic is replaced by two well-mixed reservoirs with transfer of the primary variables, temperature and salinity, between them. Stommel was able to show that there are two stable regimes of North Atlantic circulation, one with a circulation comparable to that measured at the present time, and one with a greatly reduced circulation. Subsequently this was shown to also be present in larger more sophisticated models. This observation has had a profound influence for understanding both paleoclimate and the implications of anthropogenic climate change (Stouffer and et al., 2006; Rahmstorf, 1995).

Similar to a classical box model, a water budget model can be considered a form of box model where each box now represents the location or state of the water. Twilley and Chen (1998) created a water budget model for mangrove basin interactions which was used to develop a finite-difference hydrology model, HYMAN. This model was used to simulate the water level and salinity within 50 cm of the ground surface in Rookery Bay National Estuarine Research Reserve, Florida, U.S.A. The authors found that salinity within the ground was more sensitive to prolonged rainfall deficits at higher elevations in the intertidal zone, where tidal inundation frequency is reduced.

2.2 Study Area

Yax Chen is a 2.7 km long subsection of cave passage and part of the larger Ox Bel Ha cave system, and is located approximately 9 km south of the city of Tulum, Quintana Roo (Fig. 2.1). The primary entrance to the cave is located within cenote Yax Chen. At approximately 270 km long, Ox Bel Ha is a very large network of anastomosing cave passages that generally trends in a NW to SE in direction (https://caves.org/project/qrss/qrss.htm; Fig. 2.1). Seven cenotes open along the length of cave passage, covering a total open water cenote area of 35,000 m^2 (Collins et al., 2015). The main passage of the cave system is relatively shallow with an average depth of 8 m in the downstream portion (from the L-Shaped cenote to Yax Chen cenote) and 11 m in the upstream section (from L-Shaped cenote to Gemini cenote) (Collins et al., 2015). Flow within the passage is coastwards and is generally low at approximately 10 cm/s increasing to 25 cm/s during heavy rainfall (Moore et al., 1992; Brankovits et al., 2018).

In the study area, mangroves extend inland to the Isod 2 cenote where the vegetation transitions to an upland forest terrain that is characterized by exposed karst with no or

very thin soil coverage (Collins et al., 2015). The mangroves roots descend through the peat into the groundwater however the upper layers of the peat remain dry unless the water table rises sufficiently.

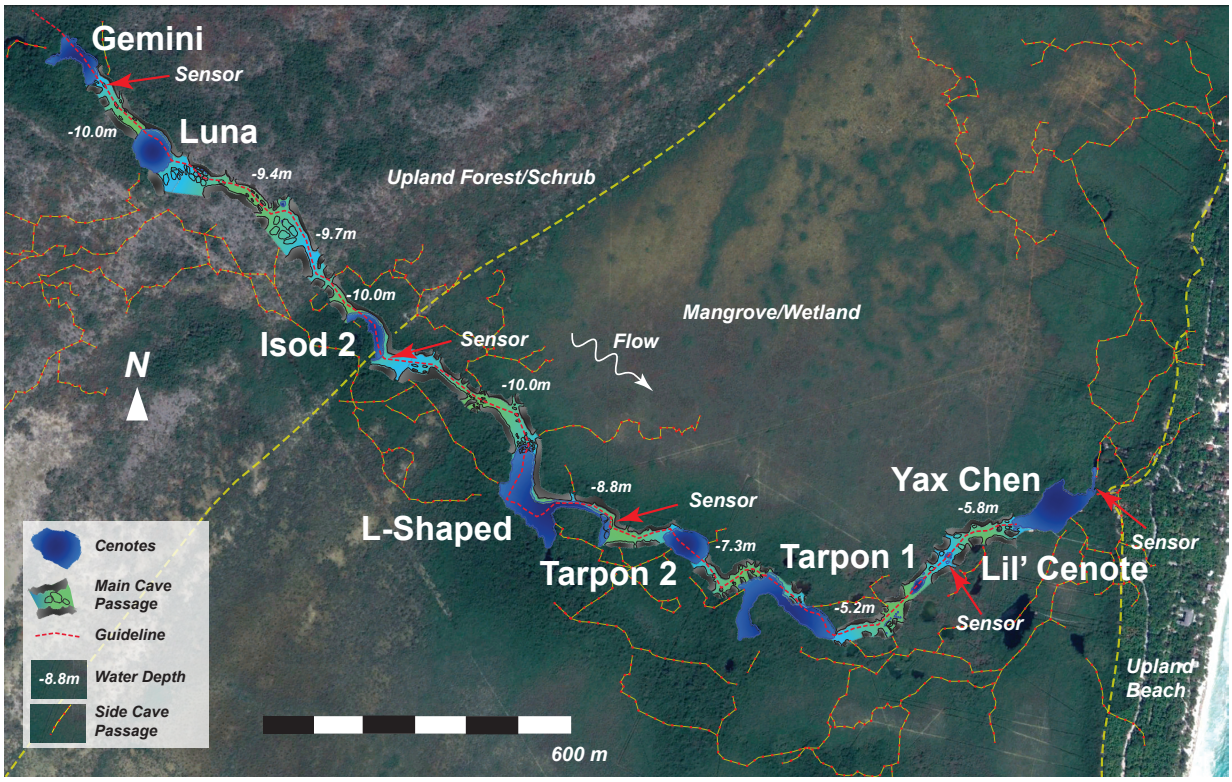

Figure 2.2: A map of the Yax Chen cave system where the sensors were deployed. The section shown here extends roughly 3 km. The red arrows indicate the location of the sensor stations located at an approximate depth of 2 m and 10-30 m downstream of open cenotes. The yellow dashed lines indicate changes in the surface vegetation from Upland Forest to Mangrove to Upland Beach.

2.3 Methods

2.3.1 Sensor Placement and Rainfall Data

All sensors were placed within the cave passage at a depth of approximately 2 m and were located 10 to 30 m downstream (coastward), from cenotes Gemini, Isod 2, L-shaped, and Lil' with the exception of Yax Chen were placed below a dock within the cenote (Fig. 2.2; red arrows). Cenote Gemini is located well within the upland forest, Isod 2 cenote is located at the border of the upland forest and mangrove coverage (Fig. 2.2; the yellow dashed line), and the remaining cenotes (L-Shaped, Lil', and Yax Chen) are located within the mangrove area. Two types of sensors were used: 1) The HOBO Conductivity Data Logger from OnSet (Model:U24-001) provides both conductivity (± 5 μS/cm) and temperature ($\pm\,0.1$°C) measurements with resolutions of 1 μS/cm and 0.01°C respectively; 2) The HOBO Water Level Data Logger from OnSet (Model:U20L-02) provides both water pressure ($\pm\,1.20$ kPa) and temperature ($\pm\,0.44$°C) measurements with resolutions of 0.04 kPa and 0.1°C respectively. Due to the lower temperature accuracy on the U20L, the U24 temperature values were used. An additional pressure sensor was affixed to a tree above a small unnamed cenote along the passage to record atmospheric pressure to properly calculate water depth. Specific conductance (μS/cm), was converted to salinity (ppt) using an empirical equation ((Fofonoff and Millard Jr., 1983)). This equation is valid for salinity values from 2 to 42 ppt which is within the range of known salinity values for the system ((Collins et al., 2015)). The sensors were left in place for two years (2016-2018), though there are several gaps due to battery failure and sensor malfunction. However, as the data from the sensors was collected every six months (in May and December), the shortest gap in data was six months. Each of the sensor sites are named after the closest upstream cenote (from furthest inland to the coast): Gemini, Isod 2, L-Shaped, Lil', and Yax Chen (Fig. 2.2). Hourly rainfall data (mm/hr) from the city of Tulum was gathered from `https://www.worldweatheronline.com`. This location was used as previous sensors had been stolen and this was the closest secure location. The weather data spanned the year of 2017. Based on this data we will refer to a 'small' rainfall event as one with a rainfall rate of less than 200 mm/day, while a 'large' event is one with more than 200 mm/day.

2.3.2 Model Development

A conceptual diagram illustrating the mangrove hypothesis proposed in Collins et al. (2015) is shown in Fig. 2.3. In mangrove covered areas, rainfall is unable to infiltrate through

the karst as the peat layer underneath the mangroves acts as an aquitard. This pooled water has a high residence time in the mangrove and is thus warmed through solar forcing. Moreover, daily tidal pumping is insufficient to flush it out. During a light rainfall event, the water table does not rise significantly and there is little surface flow from the mangroves into the open cenotes because of a low hydraulic gradient. The dominant input to the groundwater is thus direct rainfall which cools the groundwater (Byers et al., 1949; Kovacs et al., 2018). During high rainfall events, there is sufficient rainfall to raise the water table so that as the groundwater draws down post event a large hydraulic gradient is created between the open cenotes and the pooled mangrove water. Inflow of the warm water from the mangrove causes an increase in temperature in the cenote and surrounding groundwater. In the forested areas the rainfall is able to directly infiltrate through the karst (Collins et al., 2015). As the rain does not pool on the surface it is not warmed and subsequently directly cools the MeWM.

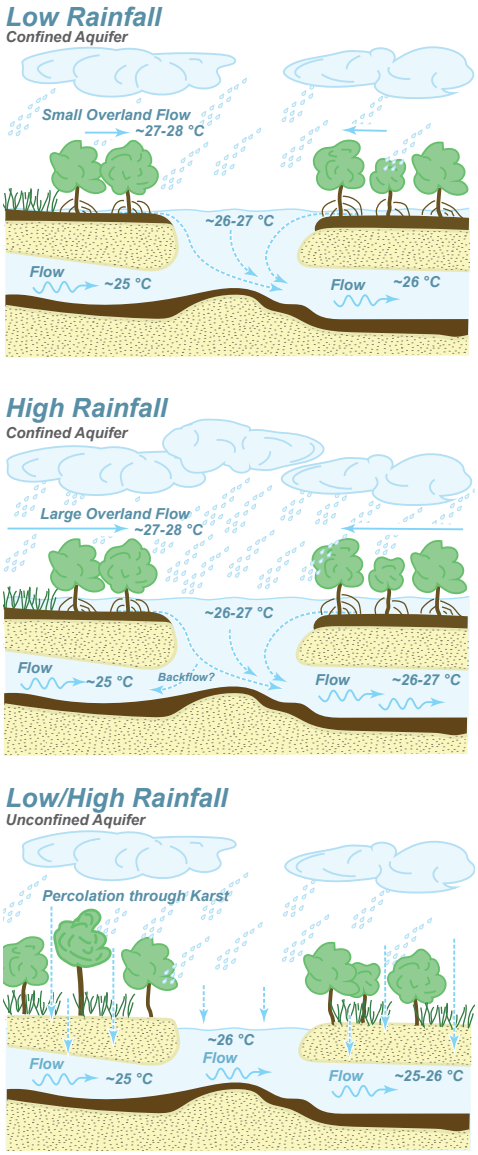

Figure 2.3: A conceptual diagram of the mangrove-groundwater/cenote interactions. In a confined aquifer there is a small hydraulic gradient post low rainfall event and so the dominant effect is net rainfall cooling. During a high rainfall event there is a substantial hydraulic gradient and warmed mangrove water enters the groundwater warming the MeWM. In an unconfined aquifer there is no aquitard to prevent percolation through the karst resulting in no hydraulic gradient.

To test the dynamics of the mangrove interaction hypotheses proposed in Collins et al. (2015) and McNeill-Jewer et al. (2019), a simplified box model of the system was created. The key mechanism within the box model is a switch that allows flow from the mangrove into the cenote only if the mangrove water level has reached a specified minimum value. A diagram of the model set up is shown in Figure 2.4. There are two boxes in the model, one representing the mangroves water and one representing the upper 2 meters of cenote water. Within these boxes both water temperature and water level are tracked. For the cenote water temperature may change due to: a day-night oscillation, rainfall and mangrove overflow. For the cenote water level may change due to: tidal oscillations, rainfall and inflow from the surrounding mangrove. Both the mangrove temperature and water level change due to the rainfall, and the water level also changes due to the inflow. Additionally all the fields are set to exponentially return to a prescribed value, to create the simplest model possible.

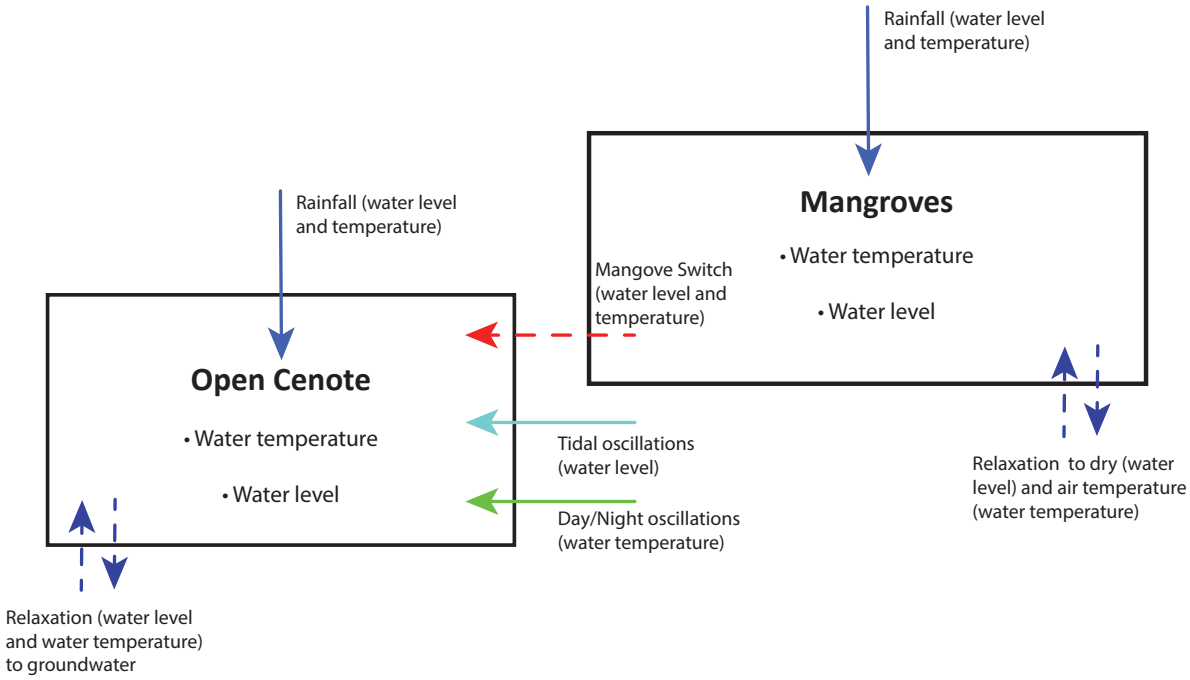

Figure 2.4: A conceptual diagram of the box model. The primary variables for the two boxes are temperature and water level. The coloured arrows indicate the various forcing to the boxes. Direct rainfall affects both the mangrove and the cenote and both the temperature and the water level. The tidal oscillations only affect the cenote water level. The day-night signal affects the cenote temperature. The mangrove switch affects both the cenote water level and temperature as well as the mangrove water level.

The set of ordinary differential equations that govern this system can be written as

$$\begin{aligned}\frac{dH_c(t)}{dt} &= R_r(t) + Ti(t) + k_1 \cdot \left(H_c^0 - H_c(t)\right)(t) \\ &\quad + k_2 \cdot H_m(t)\Theta\left[H_m(t) - H_{cr}\right], \qquad (2.1)\\ \frac{dT_c(t)}{dt} &= k_3 \cdot \left(T_c^0(t) - T_c(t)\right) + \frac{R_r(t)}{H_c(t)}\left(R_t - T_c(t)\right) \\ &\quad + k_4 \cdot \frac{H_m(t)}{H_c(t)}\left(T_m(t) - T_c(t)\right) \cdot \Theta\left[H_m(t) - H_{cr}\right] + DN(t), \qquad (2.2)\\ \frac{dH_m(t)}{dt} &= -k_5 \cdot H_m(t) - k_2 \cdot H_m(t)\Theta\left[H_m(t) - H_{cr}\right] + R_r(t), \qquad (2.3)\\ \frac{dT_m(t)}{dt} &= k_6 \cdot \left(T_m^0 - T_m(t)\right) + \frac{R_r(t)}{H_c(t)}\left(R_t - T_c(t)\right) \qquad (2.4)\end{aligned}$$

where H_c is the cenote water level, T_c is the cenote temperature, H_m is the mangrove water level and T_m is the mangrove temperature. In these equations H_c^0 is the base cenote water level, $T_c^0(t)$ is the base cenote water temperature fit, T_m^0 is the base mangrove water temperature, H_{cr} is the critical water level, R_t is the rain water temperature, and $\Theta[t]$ is the Heaviside step function. The k variables are rate constants.

We have elected to use a simple switch (via the Heaviside function) to enable flow from the mangrove box to the cenote box as a preliminary attempt. As we are primarily concerned with investigating the dynamical effects of the switch we have elected to simplify other aspects of the system, namely the mangroves are not actively heated but rather return to a higher prescribed water temperature. We are also assuming that there is a background state for which all the variables return to (water in our particular box equalizes with the rest of the groundwater), as such the equations are non-conservative. The various parameters for this model were then calculated using the full two years of data from the L-shaped location, close to the cenote entrance. Rate constants directly related to the cenote were calculated using exponential fits to the data, while the other rate constants were tuned to give the same amplitude response as what is observed in the data. The base water level was chosen to be the average depth of the open L-shaped cenote. The rain temperature of 25°C and mangrove temperature of 27.5°C were chosen based on measurements taken during May and December. The critical mangrove water level of 0.20 m was calculated using field records. All parameters were shown to fit the data best using a Markov Chain Monte Carlo algorithm using the Stan software (https://mc-stan.org/). The baseline water level, water temperature, critical water level, and rate constants are listed in Table 2.1.

The cenote water temperature was calculated using the first terms of the Fourier Series of the data

$$T_c^0(t) = 26.61 - 0.173\cos\left(6.7\times10^{-4}t\right) - 8.8\times10^{-3}\sin\left(6.7\times10^{-4}t\right). \tag{2.5}$$

The day/night signal rate was created by taking the derivative of a 24h signal with an amplitude equal to the time-averaged amplitude of the data at this period along with an additive white noise perturbation

$$DN = -1.9\times10^{-2}\sin\left(\frac{\pi}{12}t\right) + 0.01N_1^0. \tag{2.6}$$

N_1^0 indicates the standard normal distribution. The tidal oscillation rate was similarly created by taking the derivative of a diurnal and semi-diurnal oscillation with an amplitude equal to the time-averaged amplitude of the data at this period along with additive white noise perturbation

Parameter	Value
H_c^0	10 m
H_{cr}	0.2 m
R_t	25 °C
T_m^0	27.5 °C
k_1	0.0167 per day
k_2	0.001 per day
k_3	0.03 per day
k_4	0.8 per day
k_5	0.0167 per day
k_6	10 per day

Table 2.1: A list of the box model parameters that were used. These parameters were calculated either through direct fits of the data (rate constants) or by match the results to the data.

$$Ti = 9.6 \times 10^{-4} \cos\left(\frac{\pi}{12}t\right) - 8.2 \times 10^{-3} \cos\left(\frac{\pi}{12}t\right) + 0.01 N_1^0. \tag{2.7}$$

This box model was implemented in MATLAB®. As we are not concerned with the numerical analysis properties of this model and are computing over long times, a simple backwards Euler method was used for the time stepping. $\Delta T = 0.1$ h was considered sufficiently small to provide reasonable temporal resolution. Furthermore as the rain data was provided with a uniform time step, an adaptive time step would have required interpolation, and was considered to be excessively complicated for a first implementation. Both the model presented here and the data used can be found at https://git.uwaterloo.ca/acoutino/mangrove-box-model.git.

For the preliminary test case, the rainfall event is modelled by a simple Gaussian (normal) curve with a duration of 24 hours. Seasonal variations in $T_c^0(t)$ were disabled and the temperature was set to a constant value of 26.61 °C. The day-night and tidal signals were removed. We consider two cases; a 'low' rainfall event and a 'high' rainfall event. The 'low' event peaks at 10 mm/hour while the 'high' event peaks at 60 mm/hour. Fig. 2.5 (a) presents the normalized water level and temperature of the cenote. The water level reaches a maximum in the hours following the peak in rainfall (at 200 hrs), at a similar time the minimum in water temperature is observed. The water level and temperature then return to their equilibrium values 150 hrs later. The side panels (Fig. 2.5 (b), Fig. 2.5 (c), Fig. 2.5 (d), Fig. 2.5 (e)) show the physical (i.e. non-normalized) water temperature and

water level fields for both the mangroves (right) and the cenote (left). The total increase in water level of both the mangroves and the cenote is 5 cm. The water temperature in the mangroves drop approximately 0.08 °C before quickly returning to the prescribed 27.5 °C. The water temperature in the cenote drops 0.008 °C and takes 150 hrs to return to equilibrium values. The quantity of water in the mangrove was substantially less than the cenote, the rain thus proportionally cooled the mangrove more, resulting in the variation in the temperature.

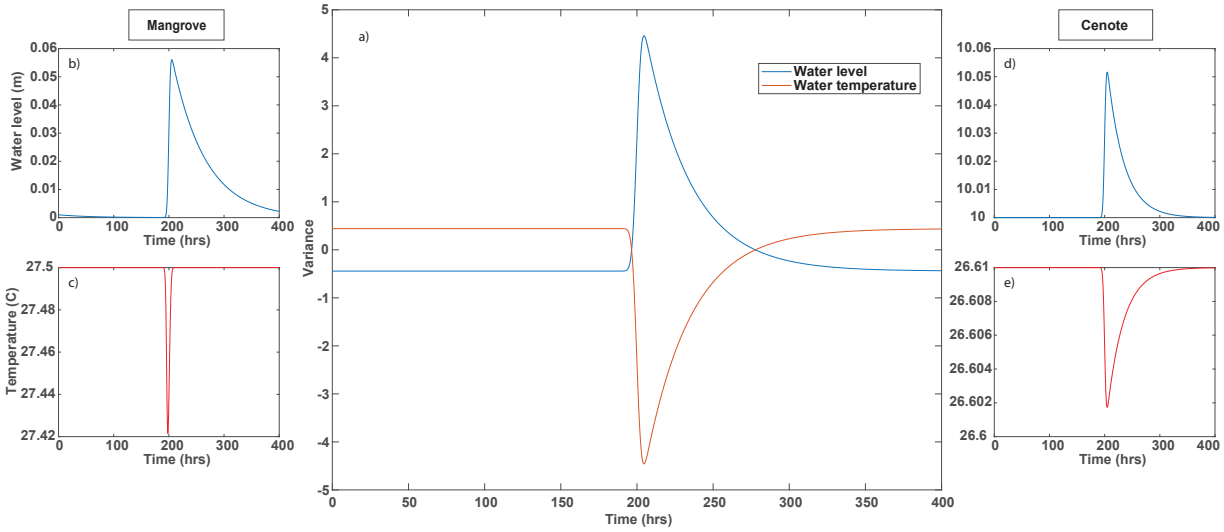

Figure 2.5: Test case of a 'low' rainfall event in the box model. Panel (a) is the normalized cenote water depth and temperature shown on the same axes. (b) and (c) are the dimensional mangrove water depth and temperature. (c) and (d) are the dimensional cenote water depth and temperature.

The water level (Fig. 2.6 (a)) follows a similar pattern as in the 'low' rainfall case, peaking a few hours after the maximum rainfall at 200 hrs. However immediately following the peak, the water level decayed slower than in the previous case until around 240 hrs when there was a cusp-like transition and then the water level decayed faster. This abrupt change was due to the switch being activated until 240 hrs, thereby reducing the draw down by adding mangrove water to the cenote box. The temperature begins dropping slightly around 200 hrs and dramatically increases in the following hours until it reaching a peak at around 230 hrs. The temperature then begins to decay slowly before reaching a cusp-like transition and then rapidly decaying to its undisturbed value. Physically, the water level in both the mangrove and the cenote increased by 30 cm (Fig. 2.6 (b) and (d)).

The mangrove water decreased by a maximum of 0.14 °C (Fig. 2.6 (c)). The temperature in the cenote decreased by 0.01 °C and then increased by 0.15 °C (Fig. 2.6 (e)).

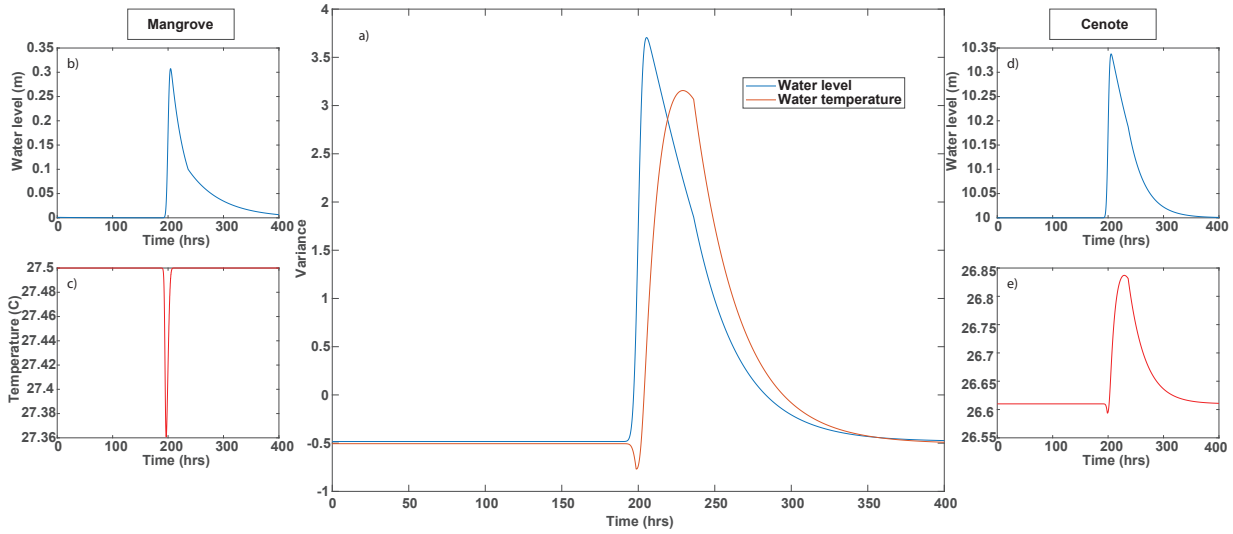

Figure 2.6: Test case of a 'high' rainfall event in the box model. Panel (a) is the normalized cenote water depth and temperature shown on the same axes. (b) and (c) are the dimensional mangrove water depth and temperature. (c) and (d) are the dimensional cenote water depth and temperature.

2.4 Results

2.4.1 Sensor Observations

The water depth (Fig. 2.7 (a)) at all locations exhibit similar long-term and short-term oscillations, with only minor differences in amplitude. Rapid increases in water depth are associated with rainfall events and are commensurate with previously observed water level changes in Yax Chen (Kovacs et al., 2017; Coutino et al., 2017). Also visible is the wet–dry yearly oscillation which exhibits a slightly elevated average water level from August to January.

Salinity (Fig. 2.7 (b)) follows a similar pattern to water depth, exhibiting longer scale seasonal oscillations as well as prominent rapid increases resulting from large rainfalls.

The behaviour across all the sensor locations follows a similar pattern, though differing slightly in salinity value. The most prominent features in the salinity graph are the large increases in salinity associated with hurricanes and tropical storms. The largest event is Hurricane Nate in October 2017. This event caused a large increase in the salinity of the upper portion of the MeWM, raising it more than 2.5 ppt across all sensor locations in less than 12 hours. Following Hurricane Nate and Tropical Storm Philippe, the previous gradient of salinity values (Yax Chen most saline to Gemini least saline) changes with the Isod 2 and L-Shaped locations becoming the least saline. The other large salinity increase is Hurricane Earl in August 2016, however it does not appear to have had as long-lasting an impact on MeWM salinity as Hurricane Nate. Smaller rainfall events are also reflected as slight increases in salinity.

The temperature records (Fig. 2.7 (c)) show less variability with the large rainfalls. The dominant responses are rapid (few hours) small decreases, followed by return to mean values over a slightly longer time (few days). The seasonal variation is visible in the temperature time series as two regular oscillations between wet and dry seasons. The other dominant feature is the difference between Yax Chen, L-Shaped, Isod 2, and Lil' Cenote which have very similar temperatures (26 ± 0.50 °C) and that of Gemini which is 1 °C cooler (25 ± 0.50 °C). This temperature difference was verified with four independent dive computers that recorded a similar temperature decrease. Isod 2 exhibits the least amount of short term variability, Gemini exhibits a moderate amount and L-Shaped, Lil' Cenote and Yax Chen all have the most short term variability which follows the distribution of mangrove, with Gemini in an upland forested terrain, Isod 2 at the transition to mangrove and L-Shaped, Lil' Cenote and Yax Chen within the mangrove terrain.

Fig. 2.8 presents the data collected during the October 2017 rainfall events (Hurricane Nate and Tropical Storm Philippe) where both events are visible as perturbations to all three records. At all locations water level increased close to 0.34 m in 12 hours. At the Gemini and Isod 2 locations, temperature, water depth and salinity all begin to increase at the same time. In contrast, at the L-Shaped location water depth and salinity begin to increase at the same time but temperature only changes afterwards. At Yax Chen small coincident peaks are observed across all the measurements followed by a decrease in water level, a maximum in temperature and finally a maximum in salinity. The pattern observed during the first event is consistent during the second event. However, during the second event the local maxima in salinity and temperature at the Gemini and Isod 2 locations coincide.

The response of the system to the October 2017 rain event (Fig. 2.8) is contrasted with the response to a smaller rainfall in early January 2017 in which water level increased by $\sim$ 0.14 m in 24 hours (Fig. 2.9). Across all locations the same pattern is observed: an

increase in water level, an increase in salinity and decrease in temperature which all begin at the same time. The local maxima in salinity and local minima in temperature coincide at the L-Shaped and Lil' locations, while they do not coincide at the Gemini and Isod 2 locations. Following the event, all the locations follow the same pattern of decreasing water depth and increasing temperature.

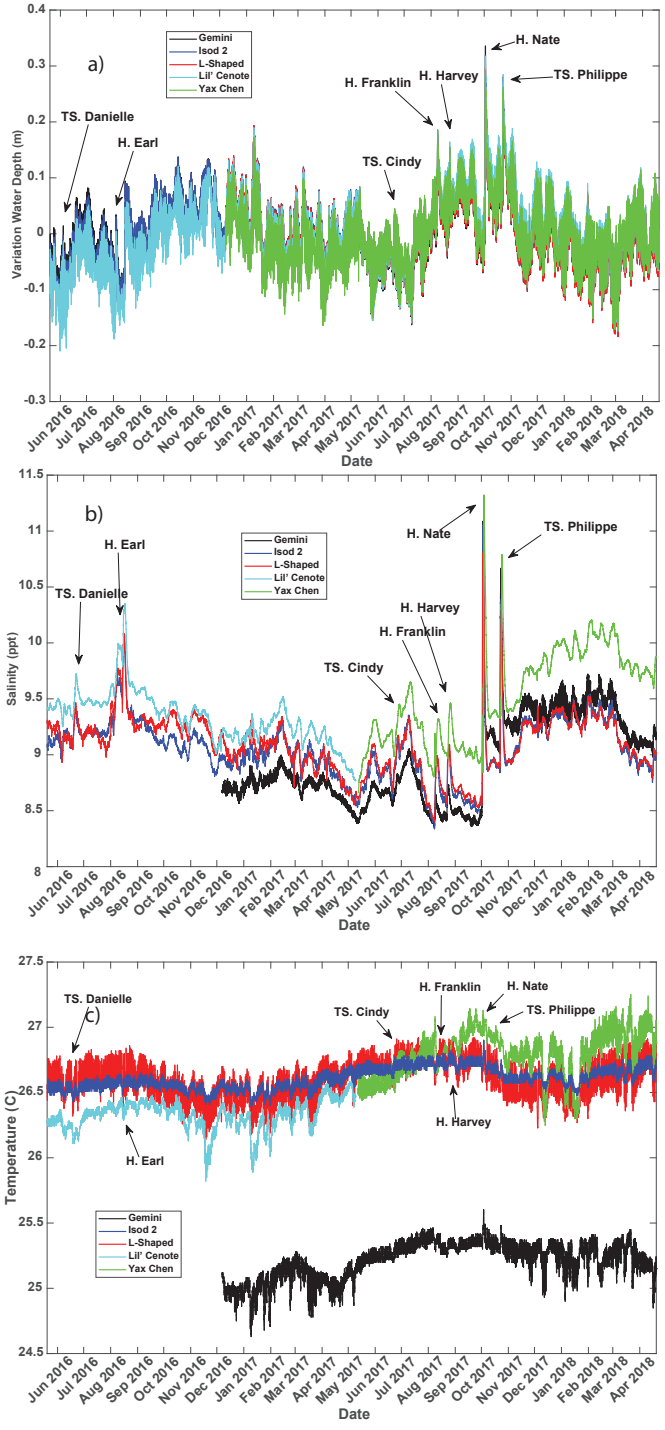

Figure 2.7: A summary of the data recorded during the two year study period. Water depth is shown in (a), salinity is shown in (b) and temperature is shown in (c) for each of the sensor stations. Black arrows indicate the name and date of known tropical storms and hurricanes that impacted the region.

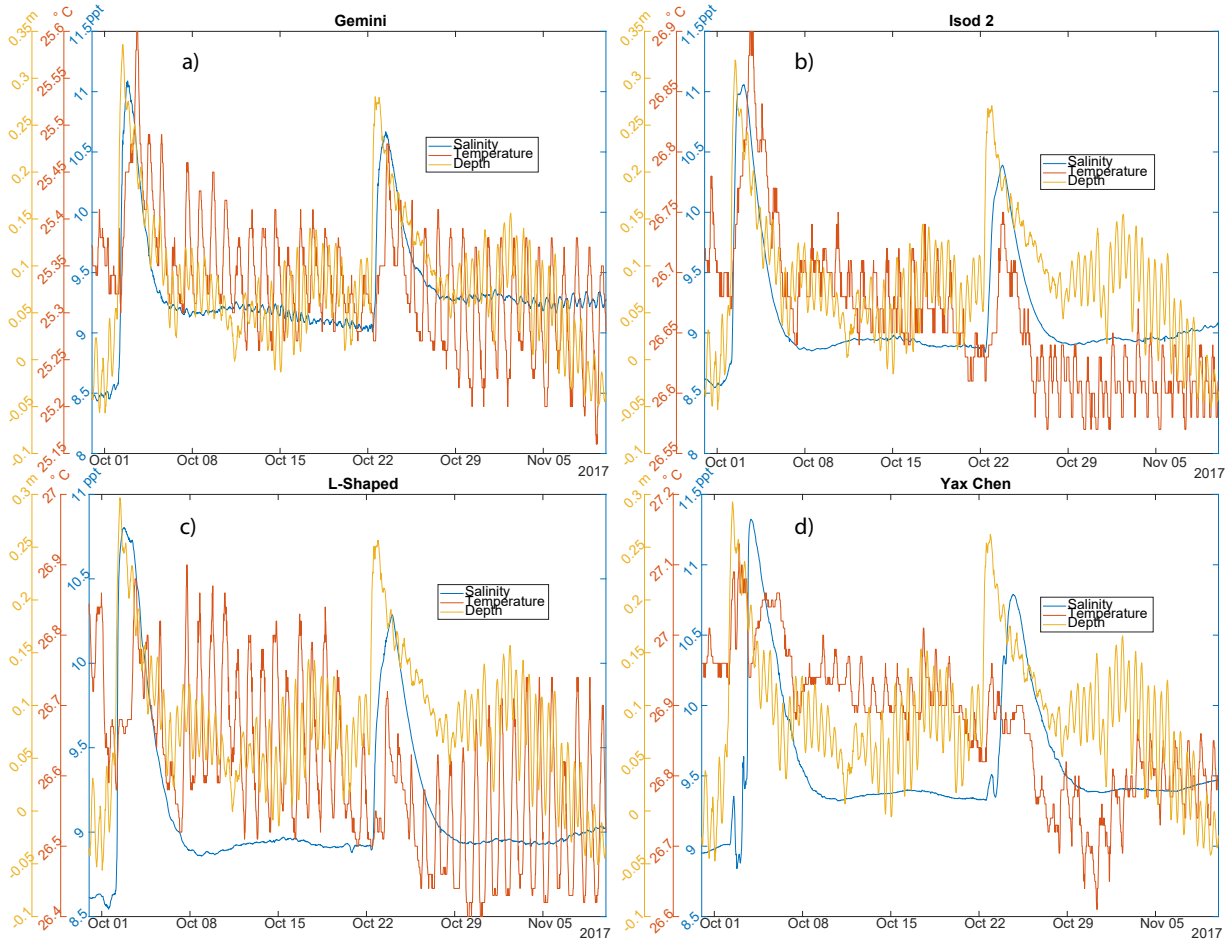

Figure 2.8: The salinity, temperature and water depth measurements at the sensor locations during the October 2017 hurricane and tropical storm. (a) Gemini, (b) Isod 2, (c) L-Shaped, and (d) Yax Chen.

Figure 2.9: The salinity, temperature and water depth measurements at the sensor locations during a rainfall event in January 2017. (a) Gemini, (b) Isod 2, (c) L-Shaped, and (d) Lil'.

2.4.2 Model Output

For model runs meant to simulate measurements, rainfall data from the city of Tulum for the year of 2017 was used as input. The results of the model were then compared to the sensor measurements from the L-Shaped location as it was within the mangroves and the data did not have any interruptions.

There is a general agreement between the model and sensor temperatures (Fig. 2.10 (a)). There are periods of time during which the model and the data align well (3000-5000 hrs), but also periods where the sensor data appears to exhibit more variation than the model (from 0-2000 hrs and 7000-8500 hrs). These periods coincide with the wet season and increased rainfall. During the Hurricane Nate rainfall ($\sim$ 6594 hrs) the model precisely matches the timing of the increase in temperature. This increase occurs 24 hours after ($\sim$ 6618 hrs) the peak in water level.

The model and sensor water depths also exhibit some agreement (Fig. 2.11). The values did not match precisely during the middle portion of the year (3000-5000 hrs) however the temporal pattern in water depth did match. Many of the rainfall events are also captured, however the model quickly returns to baseline conditions while the sensor data exhibits a slower rate of return and the measured water depth does not fully return to baseline. Further, there are discrepancies in rainfall events, with some increases appearing in one data set but not the other. The Hurricane Nate event was captured accurately, the timing of the model peak in water level was within 4 hours of the observations and reflects the post rainfall decline in water level.

To quantify the agreement between the model and the field observations we have elected to use wavelet coherence (Torrence and Compo, 1998; Grinsted et al., 2004). Due to the large number of data points, traditional cross correlation metrics do not provide meaningful values. For example, the correlation coefficient for the temperature is 0.83, and the coefficient for the depth is 0.22, however they both have a p-value of 0 indicating they are significant. Both depth and temperature exhibit coherence (Fig. 2.12) during the Hurricane Nate event ($\sim$ 6600 hrs). The model depth (Fig. 2.12 (a)) exhibits high (> 0.8) coherence with the field results particularly for the band between 96h and 512h. The model temperature (Fig. 2.12 (b)) also exhibits high coherence, however compared to the depth the temperature is coherent at a slightly shorter time band (between 64h and 130h). In both areas of coherence the arrows are pointed to the right indicating that there is essentially no phase shift.

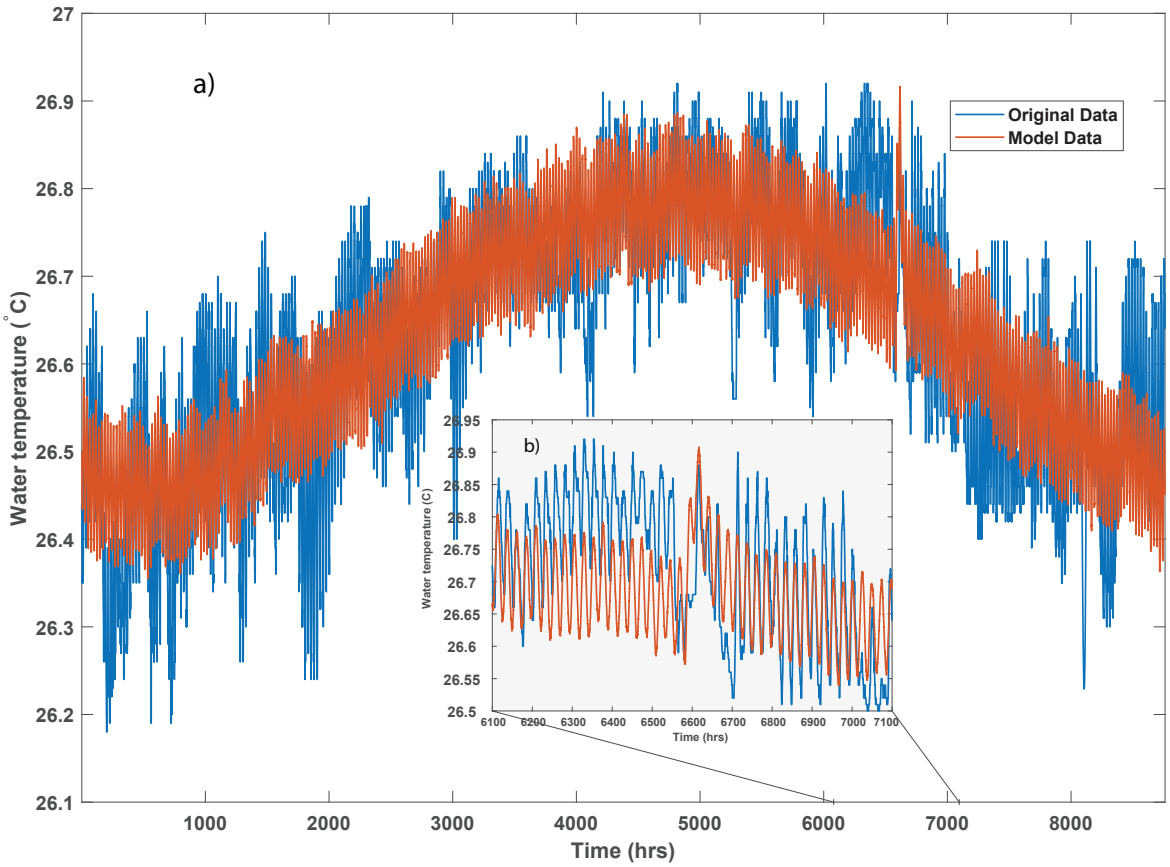

Figure 2.10: A comparison of the model temperature output with the data collected from the L-Shaped location using Tulum rainfall data. (a) The temperature comparison for the year of 2017. (b) Hurricane Nate.

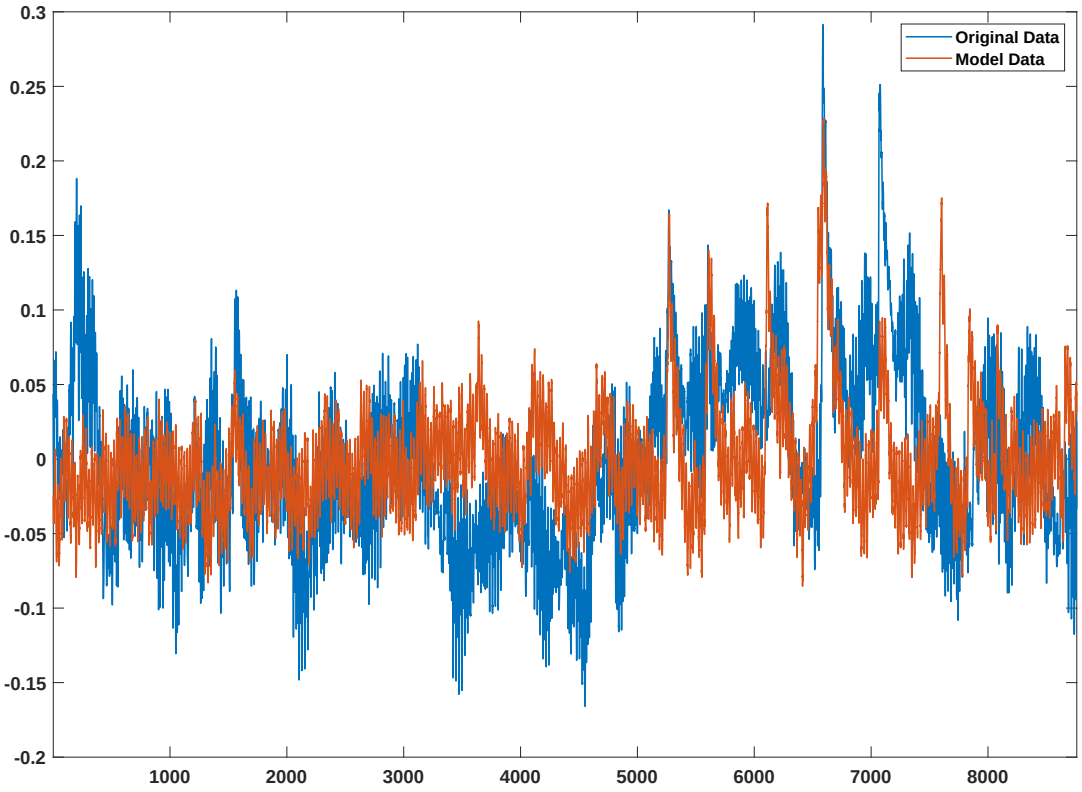

Figure 2.11: A comparison of the model water depth output with the data collected from the L-Shaped location using Tulum rainfall data.

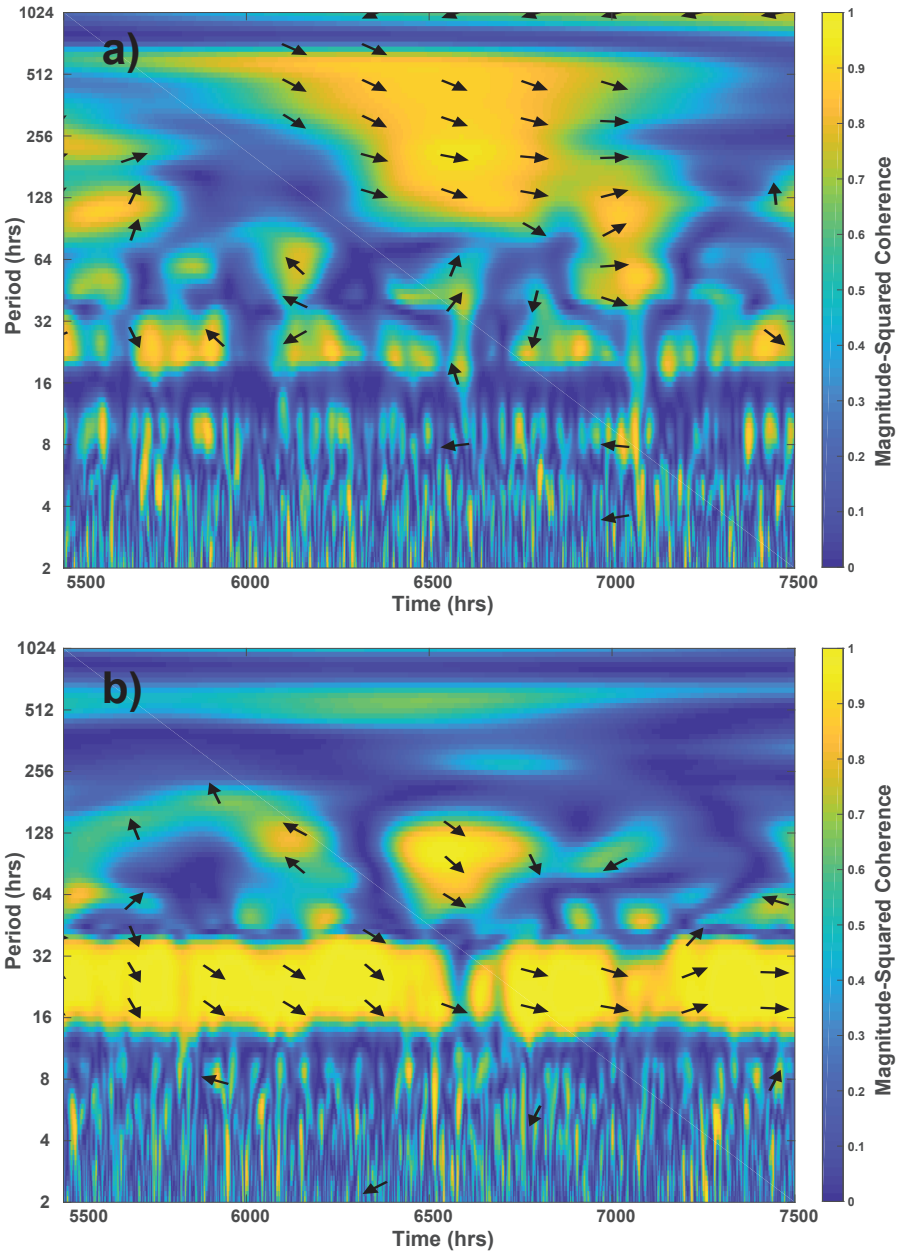

Figure 2.12: The wavelet coherence of measured and simulated depth (a) and temperature (b) during the Hurricane Nate event.

2.5 Discussion

There is a distinction between the response of the forested sensor locations (Fig 2.8 (a) and (b)) and the mangrove surrounded locations (Fig 2.8 (c) and (d)) to heavy rainfall events. During Hurricane Nate, within the forested locations, the temperature and salinity respond at the same time indicating interaction of precipitation with the underlying MaWM. In the mangrove region, the temperature and salinity responses are not coincident, indicating a different mechanism of action in comparison to the other locations. The temperature response in these areas is delayed and coincides with the decrease in water level post rainfall event. Together these responses indicate that there is a large input of warm fresh water that occurs after the rainfall. This appears to be consistent, as the same pattern occurs during Tropical Storm Philippe and provides support for the mangrove influence hypothesis (Fig. 2.3). Collins et al. (2015) used bi-annually collected sediment traps within the Yax Chen cave system to show the effects of mangrove distribution and cenote size on cave sedimentation patterns, and inferred that low-lying mangrove environments allow flushing of nutrient rich waters into the sunlit cenotes during large rainfalls, causing increased primary productivity which is then advected downstream into the cave passages. Recently, McNeill-Jewer et al. (2019) has also found that the mangroves have an impact on the elemental inputs to the aquifer. Using the same sediment trap configuration as Collins et al. (2015); McNeill-Jewer et al. (2019) detected increased levels of silica and organic matter inputs from the mangrove areas when compared to the terrestrial forest areas. These elemental signatures added support to the hypothesis proposed in Collins et al. (2015) that the mangrove dominated cenotes act as points of water collection during heavy rainfall due to concentration of rainwater within the surrounding mangrove peat. It is hypothesized that the peat aquitard prevents immediate downward percolation after rainfalls, and allows for the accumulation of nutrients within the water which later provides organic matter inputs to the cave system. In contrast, the upland forest terrain has less nutrient input into the cave system, as rainfall is able to directly percolate through the karst and into the subsurface aquifer. Although this was a plausible explanation for the pattern of deposition observed in the sediment trap data, until now there was no direct hydrological data to reinforce this interpretation. The box model created in this paper provides the hydrological connection and data to solidify this interpretation.

The difference in response across the geographic locations during heavy rainfall events is contrasted with the similarity in response across the geographic locations to small rainfall events (Fig. 2.9). While there are minor differences in timing and specific values, the general pattern of response across all the locations is consistent. The temperature response to smaller events is the opposite to what is observed during heavy rainfall events (a decrease

in temperature rather than an increase). This indicates that the mechanism which drives the differences observed during heavy rainfalls is not active during smaller ones, which further supports the mangrove influence hypothesis.

The box model was created with the intention of testing the influence of mangrove coverage, specifically the difference in timing of the responses of temperature and water level. This is illustrated in the difference in response of the model to a 'high' and 'low' rainfall event. Comparing the shape of model created curves during the 'low' rainfall event (Fig. 2.5) with those observed in the data (Fig. 2.9) we can see that the pattern is qualitatively similar. During the 'high' rainfall event, the dynamics are fundamentally different (Fig. 2.6) than in the 'low' rainfall and the dynamics are qualitatively similar to those observed in the data (Fig. 2.8). Specifically, a sharp peak in water level corresponds to a small decrease, followed by large increase in temperature. More importantly, the model captures the delay in temperature peak observed in the field data.

When the Tulum rain data is used as input for the model (Fig. 2.10 and Fig. 2.11) the results broadly reproduce what is observed. While there are differences, the focus of the model (the response to rainfall events), is faithfully reproduced. Specifically, the timing of both the peak in water level and water depth during Hurricane Nate are extremely accurate. As this model was designed to capture the dynamics of rainfall events the primary validation we are concerned with are these responses, and not the longer time-scale aquifer dynamics for which this simple model may not be suitable.

2.6 Conclusions

In this paper we have presented results from the ongoing study of the coastal Yucatan aquifer and the Yax Chen cave network. Conductivity, temperature and pressure sensors placed high in the water column have supported the results found in Coutino et al. (2017) and Kovacs et al. (2017), that significant mixing of the MeWM and MaWM occurs in response to rainfall events. The data that was collected from Yax Chen sites covering both mangrove dominated coastal areas and forested upland areas show systemic differences in their response to large rainfall events. In the forested areas the rainwater directly infiltrates into the subsurface and results in mixing of the MaWM. This is expressed by the coincident salinity and temperature increases observed in the sensor data. In the mangrove covered areas, there is a small initial decrease in temperature followed by a large increase in water temperature that is not coincident with salinity. This occurs during the water level decline that follows a rainfall event. Following the hypothesis raised in Collins et al. (2015), we suspected that this was a result of mangrove coverage surrounding the cenotes with the

underlying mangrove peat layer acting as an aquitard and forcing the water to collect in the mangroves. This water would be warmed through air temperature and solar forcing and when the water levels began to decrease post rainfall, would flow into the cenotes and warm the MeWM. This effect is contrasted by smaller rainfall events where the mangrove peat is not fully saturated and does not accumulate enough to flow into the cenotes during draw down. This is observed in the sensor data as both forested and mangrove covered areas responding similarly to these events. This hypothesis was tested by creating a box model of this interaction with a switch allowing for flow from the mangroves when a certain minimum water table level is reached. Through simplified test cases it was shown that the observed dynamics were captured by this simple model. The model was then tested by forcing using rainfall data from the city of Tulum for the year 2017. During the hurricane event there is correspondence between the model and the observations despite the simplifications and assumptions made. The results of this analysis provide quantitative support to the mangrove influence hypothesis. Understanding this pathway of mangrove water into the aquifer is important, as mangrove peat can often be a heavy metal sink, and when heavily disturbed could potentially become a source of nutrients and contaminants to oligotrophic shallow coastal zones and reef systems due to increased erosion, deforestation and degradation as the area continues developing (Clark et al., 1998; Defew et al., 2005; Bayen, 2012).

As noted previously, this model was designed specifically to capture the dynamics of rainfall events. Hence, we are not concerned with the general difference that could be observed during the non-rainy portions of the year. The box model is extremely simple and does not include many of the known forcing mechanisms and dynamics such as spring and neap tides and the suppression of tidal oscillations during the rainfall events (Coutino et al., 2017). While the rainfall data taken from the city of Tulum is relatively close to the field location, the extremely localized nature of the rainfall events in this region results in an error in the timing and magnitude of many of the events. Further, due to the connected nature of the groundwater it is possible that rainfall events from upstream of the study site can impact the observations, which would not be captured by relying solely on rainfall from Tulum.

There are many natural extensions to the model, beginning with the addition of salinity and partitioning the cenote box into two boxes, one for each of the MeWM and MaWM. With the advent of anthropogenic climate change and sea level rise, significantly more of the Yucatan platform will consist of these coastal mangrove systems, and more variable climate will result in changes to how the aquifer responds. This is particularly important given the effect of global climate change and sea level rise, which will likely submerge these mangrove areas in the coming decades. This, coupled with increased coastal development

may heavily disturb the mangrove ecosystem and could potentially change mangrove peat from a sink to a source of heavy metals and other nutrients (Kathiresan and Bingham, 2001; Marchand et al., 2011), which could have serious impacts for coastal environments.

Another avenue of further research would be a larger investigation into the effect that the tides play on mangrove inundation and the impacts that it may have on the MeWM. Due to the relatively weak coastal tidal amplitudes the effects would likely be limited to near surface waters as the mangrove water slowly flows into the cenotes, however such consistent flushing may have larger environmental effects due to micro-nutrient inputs. One possible avenue of further research would be to look at intermediate sized rainfall events and how the mangrove coverage becomes more important to the dynamics as rainfall increases.

This work has shown that the mangroves are the likely reason for dynamical differences in rainfall events, however the impact of this effect on the aquifer system remain to be documented in detail. In addition to supporting the results showing differences in geochemical signatures of the sediment input based on cenote vegetation coverage (McNeill-Jewer et al., 2019), it highlights the effect that mangroves can have on the groundwater in extremely karstic areas.

2.7 Commentary

This article was originally published as:

Coutino, A., Stastna, M., and Reinhardt, E. G. (2020). Interaction of mangrove surface coverage and groundwater inputs on the temperature and water level near Tulum, Quintana Roo, Mexico: Observations and modelling. Journal of Hydrology, 583, 124566.

The manuscript presented in this thesis differs slightly from the published version:

1. Two explanatory paragraphs that did not fit in the published version have been included in this version. One in the introduction expanding the section on box models and another in the introduction expanding the description of the cave systems.

2. Slight changes were made to the structure of the thesis to improve the flow of the article.

3. Small changes to wording were also made that hopefully increase the clarity of the text.

However the content of the results and conclusions remain unchanged.

As for Box models, they are limited by construction. As mentioned in the text, one of the classical examples of box models is Stommel (1961) two-box model of North Atlantic thermohaline circulation. The purpose of the model was not to reproduce the actual circulation in the North Atlantic but rather the model was intended to look at the stable long-time states of the system. One advantage of such simple models is that they are easy to extend so as to include a more accurate representations. For example, Sakai and Peltier (1997, 1999) extended the two-box model to a three-box model to account for abyssal waters. Other extensions include the addition of stochastic noise to investigate the stability of the solutions (Stastna and Peltier, 2007).

As with Stommel (1961), the box model that we created was not intended to fully capture the dynamics of the system, but rather was used to investigate the hypothesis that delayed mangrove water could account for the differences in water level and temperature we observed. Some of the limitations of the box model in the material above will be addressed here. The box model was built at the request of a reviewer who requested a stronger quantitative test of the proposed conceptual model of how mangroves effect temperature in the cave system after large rainfalls. This conceptual model is rooted in work on sediments. It was proposed in Collins et al. (2015) and McNeill-Jewer et al. (2019) to explain differences in the types of sediment that were collected from different portions of the Yax Chen cave system. The box model is not meant to fully encapsulate this very complicated mangrove–groundwater interaction, but was intended to test the hypothesis that the water level switch mechanism could reasonably explain the differences observed in the data. It would not be reasonable to expect a simplistic quasi-linear ODE model to be able to properly capture the dynamics of this system even if more accurate rainfall data was available. This is why we focus on the simplified cases showing how the system reacts to large and small rainfall events. This is also why we show the accuracy of the box model using wavelet coherence (refer to Section 1.3.3 for an overview). We show that in the periods of rainfall in question (e.g., how long of an affect a storm has on the system; a few days to a few weeks) for the event we are concerned with (occurring at roughly 65000 hrs). In this region the model has a coherence over 0.8 for the depth and 0.95 for the temperature. Within these regions, the 'arrows', which indicate phase shift, are predominantly pointing to the right indicating that the two signals are in-phase (refer to Subsection 1.3.3). We use these results to argue that within the time period in question, the model is coherent with the data. Wavelet coherence was used because due to the number of data points, traditional cross correlation metrics do not provide meaningful values. For example, the correlation coefficient for the temperature is 0.83, and the coefficient for the depth is 0.22, however they both have a p-value of 0 indicating they are significant.

In terms of extensions, it is unlikely that further 'tuning' of the model would prove useful. Instead, simplified models that are more closely tied to how sediment is deposited (and subsequently sampled by traps) would allow for a stronger conceptual link to sediment based studies.

Chapter 3

Inland tidal oscillations within the Yucatan Peninsula

3.1 Introduction

The Yucatan Peninsula (165,000 km^2) encompasses three Mexican states (Yucatan, Quintana Roo and Campeche) and is composed of Miocene to Late Pleistocene limestone which has undergone intense dissolution through cycles of sea-level change creating a karst topography (Bauer-Gottwein et al., 2011; Perry et al., 2003; Weidie, 1985). The high porosity of the limestone (14 to 23%) (Beddows et al., 2007) results in few surface water bodies (e.g. lakes), as rainfall quickly infiltrates through the limestone and into the unconfined aquifer which flows towards the coast through networks of caves and fracture zones (Beddows et al., 2007; Emblanch et al., 2003; Stoessell, 1995). The few surface water bodies that do exist are thought to contain draping layers of sediment which act as an aquitard (Curtis et al., 1996; Brenner et al., 2002; Hodell et al., 2005a; Krywy-Janzen et al., 2019). This effectively hydrologically isolates these water bodies from the larger aquifer-ocean water body, and implies that changes in water level correlate with evaporation/precipitation. On a regional scale, fracture zones (Figure 3.1, red lines) create areas of preferential groundwater flow and increased permeability (Bauer-Gottwein et al., 2011; González-Herrera et al., 2002; Perry et al., 2003). There is a general lack of research on the specifics of the western fracture zones, but general information has been inferred through geophysical studies of electrical resistivity (Steinich and Marín, 1996), numerical modeling (González-Herrera et al., 2002; Marín et al., 2004) and remote sensing (Gondwe et al., 2010). However, not much is known about the detailed connections to the ocean. More is known about the eastern (Holbox and

Rio Hondo) fracture zones as the conduits and cave passages are closer to the surface and thus more accessible. In these regions fissure passages can be 5 m to 10 m tall and 0.5 m to 2 m wide (Smart et al., 2006). Studies have found that within these high permeability zones the permeability (K) is on the order of 1 m^2 to 10 m^2 (Bauer-Gottwein et al., 2011; Marin, 1990; González-Herrera et al., 2002; Charvet, 2009), and hence classical (i.e. Darcy type) porous media theories do not apply (i.e. much larger permabilities).

The Yucatan aquifer has a stratified structure due to rainwater percolation into the subsurface which creates a density-stratified fresh lens above the marine water that intrudes inland from the coast (González-Herrera et al., 2002; Gondwe et al., 2010) The interface between the two water masses is a mixed brackish layer of intermediate salinity called the halocline that while generally thin (1-3 m), increases in vertical extent as it approaches the coast (Bauer-Gottwein et al., 2011). This stratification is well-documented for many coastal systems especially given a porous coastal geology (Cooper et al., 1964). The extent to which seawater infiltrates into the aquifer is not fully known, though it has been measured up to 100 km inland (Perry et al., 2002). While several groundwater models exist for coastal-ocean geographies (Jones et al., 2000; Sanford and Konikow, 1989), they typically assume that the region of interest has a homogeneous porosity (Hubbert, 1940; Wilson, 2005). One recent example of this approach is Levanon et al. (2017) who modeled sea-water intrusions in Israel (similar limestone karst geology), their model used a combination of Darcy's Law (saturated flow) and Richards' Equation (unsaturated flow). However, due to the presence of fractures, and large scale cave networks, this is model-type is not applicable in the Yucatan Peninsula (Kambesis and Coke, 2013). One model which has shown promise within this region is MODFLOW-CFP (Conduit Flow Process) (Shoemaker et al., 2005). The model has previously been used for sub-regional scales within the Florida aquifer (Gallegos et al., 2013) which has a similar geology to the Yucatan Peninsula. More recently Martínez-Salvador et al. (2019) used MODFLOW-CFP to estimate pollutant residence time in the vicinity of Merida, Mexico. According to the authors this is the first time that a groundwater model has been applied to that region. It remains to be seen how well the model works in other regions of the peninsula.

It is well known that coastal groundwater will respond to tidal fluctuations from the ocean (Fetter, 2001). In this region the tides propagate clockwise around the peninsula, with tide first rising in Campeche then along the northern coast, and finally down the eastern coast (6.5 hours later; see arrow in Figure 3.1) (https://www.tide-forecast.com/weather_maps/Mexico). For a confined homogeneous coastal aquifer, equations for tidal propagation inland have been created (Fetter, 2001; Ferris, 1951; Jacob, 1950) and used to determine aquifer properties (Schultz and Ruppel, 2002; Series, 1991; Smith, 1999; Trefry and Johnston, 1998). While these models have been extended to two-dimensions (Li et al.,

2000; Sun, 1997) and vertical dynamics (Li et al., 2002), they have also been shown to generate inconsistent estimates of aquifer parameters (Ferris, 1951; Trefry and Johnston, 1998; Schultz and Ruppel, 2002). Trefry and Bekele (2004) attempted to address these issues by including composite heterogeneity. The authors found that this addition yielded reasonable parameter estimates, however further research was needed to show its significance. Through idealized numerical experiments the authors also found that horizontal layering in aquifer conductivity was a dominant factor in theoretical estimates of tidal lag, which poses problems for the use of such theory in the Yucatan Peninsula with its extreme horizontal heterogeneity. Beddows (2004) applied Ferris' equations using rough estimates for the necessary parameters and showed that in Sistema Nohoch Nah Chich (10 km north of Tulum) the measured tidal amplitude was double that which was predicted by the equations. More recently (Krywy-Janzen et al., 2019) used sediment cores and water level reconstruction within Pac Chen (Pac Chen; site (D) in this publication; an enclosed freshwater lake approximately 42 km inland) to show that its water level evolved in response to sea level changes throughout the Holocene. Additionally, the authors also directly measured centimeter-scale oscillations in water level with a diurnal and semi-diurnal frequency during a six month period. It remains to be seen if other surface water bodies further inland also exhibit this connection. Showing that many of these inland lakes are hydrologically connected with the rest of the aquifer and coastal waters could have important implications for the range of climate proxies generated from similar lakes (Curtis et al., 1996; Douglas et al., 2015; Hodell et al., 1995, 2005a,b; Kennett et al., 2012; Medina-Elizalde et al., 2010; Krywy-Janzen et al., 2019). Previous studies have assumed that northern lowland lakes are isolated from the larger aquifer, or effectively isolated (leaky) due to draping of sediment, and thus are sensitive to changes in evaporation/precipitation (Brenner et al., 2002; Curtis et al., 1996; Hodell et al., 2005a,b). The conventional belief is that during periods of drought, water level is drawn down due to increased evaporation, although the amount of draw-down or lake volume change has not been thoroughly quantified for northern lowland lakes (Brenner et al., 2002; Hodell et al., 2005a,b; Douglas et al., 2015).

This study measures the extent of groundwater connection within the Yucatan Peninsula by measuring water level changes at far inland natural water bodies. These locations would traditionally be considered closed to the larger regional aquifer and we would thus not expect to observe tidal oscillations. Two types of water bodies were chosen; inland lakes (Lake Chichancanab and Pac Chen), and closed lentic (pit) cenotes (Sotuta de Peon and Chukum) which have relatively slow flow and long residence times (Schmitter-Soto et al., 2002). These locations were primarily chosen based on their geographic position and ease of access. A sensor was also placed within a coastal lagoon (Lagoon Campechen) south of the city of Tulum to allow for comparison of inland locations to coastal waters.

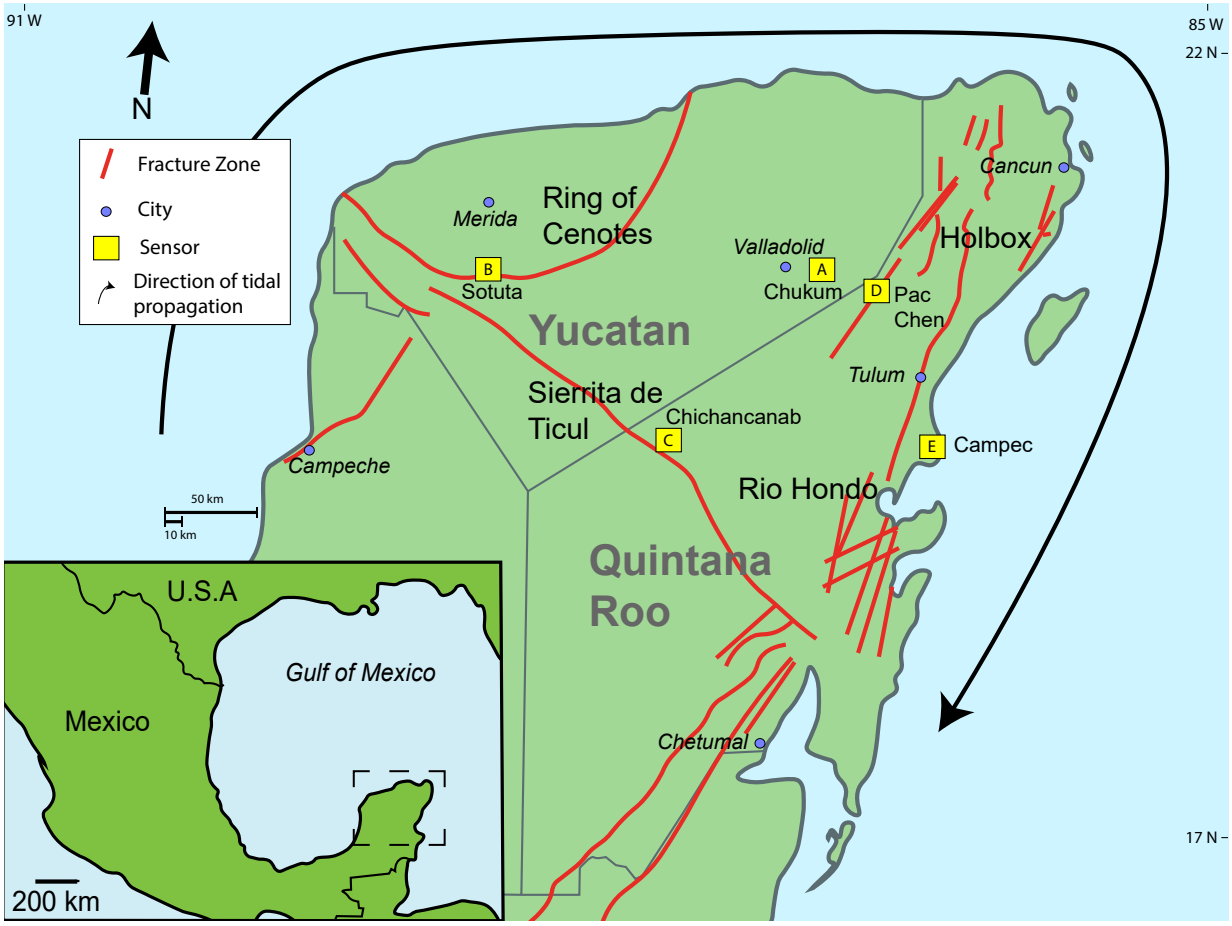

Figure 3.1: A map of the Yucatan Peninsula illustrating the different fracture zones throughout the region. In the north western region near Merida, the zone is called the Ring of Cenotes. Running north-west to south-east, the Sierrita de Ticul is situated in the centre of the peninsula. On the north-eastern coast is the Holbox fracture zones running parallel to the coast. Further south is the Rio Hondo fracture zone which is also parallel to the coast. The sensor locations used in the current study are labeled with yellow squares and data from the three most inland locations is shown for the study duration.

3.2 Methods

HOBO Water Level Data Loggers from OnSet (Model:U20L-02) were used at all the locations for water level measurements. This sensor provides both water pressure (± 1.20 kPa) and temperature (± 0.44°C) measurements with resolutions of 0.04 kPa and 0.1°C respectively. All sensors were placed 1 m to 2 m below water level. An aditional U20L-02 was placed with a rain gauge in the city of Tulum to record atmospheric pressure needed to calculate water depth. An estimate of fresh water (1000 kg/m^3) was used for the water density as salinity fluctuations within the surficial water are minimal. The sensors were in place for a six month period from May 2019 to December 2019, covering the summer dry season (May-September) and the winter rainy season (September-December). Sensors were affixed by hand to wooden dock columns at each location.

To verify that the information detected in the water level data was significant and due to more than random fluctuations, null hypothesis testing was conducted (Zhang and Moore, 2011). MATLAB's built-in Auto Regressive parameter estimator was then used to create the Null Spectra (https://www.mathworks.com/help/econ/regarima.estimate.html), and a 95% Confidence level was calculated (Wilks, 2007). To further analyze the records, wavelet coherence testing was also performed. In wavelet coherence testing, the wavelet spectra of both signals is calculated and used to compute the correlation at various times and periods. The imaginary component of the wavelet coherence can be used to calculate lag between the signals and is conventionally plotted as an arrow with rightward (leftward) pointing indicating signals that are in phase (out of phase) (Mallat, 1999; Torrence and Compo, 1998).

3.3 Results

Oscillations at the diurnal and semi-diurnal periods were observed at all three of the newly sampled locations (Figure 3.1; (A), (B), and (C)), and re-observed at Pac Chen (Figure 3.1 (D)). The full extent of these records is presented in Figure 3.2. All inland locations ((A) to (D)) exhibit an overall seasonal cycle with the lowest water level in Setember-October, and an highest in November-December. This feature coincides with known seasonal water level changes in the Yucatan aquifer (Kovacs et al., 2018).

To isolate the amplitude of the tidal oscillations, the signals from all locations were bandpass-filtered to only contain the 48 hour to 5 hour range (Figure 3.3). The Lagoon Campechen location exhibited the largest variations in amplitude (Figure 3.3 (E)). The

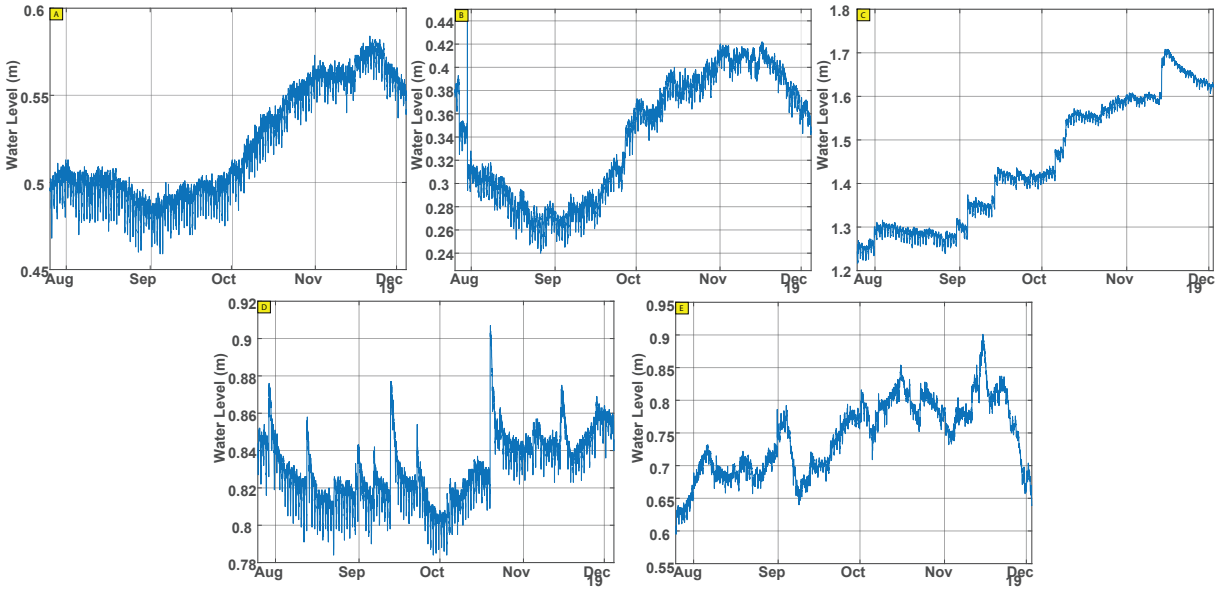

Figure 3.2: Full water level record across all study sites. (A) Hacienda Chukum, (B) Sotuta de Peon, (C) Laguna Chichancannab, (D) Laguna Pac Chen, and (E) Lagoon Campechen

Hacienda Chukum and Sotuta de Peon locations exhibited the least long term variability (Figure 3.3 (A) and (B)), while Lake Chichancanab and Lake Pac Chen exhibit intermediate variability (Figure 3.3 (C) and (D)). The lower plot of each panel is the raw spectra of the observations (blue) and the band-passed signal (red). While there are minor variations in specific amplitude, all locations exhibit the same four peaks within the bandpassed range, corresponding to in descending period, the diurnal tides (K_1, O_1, S_1, and M_1), semi-diurnal tides (M_2, S_2, and N_2), terdiurnal tides (MK_3 and M_3) and overtides (M_4, M_6, S_4, and S_6). It can also be observed that within this period range the amplitudes are on the order of one centimeter.

Figure 3.4 shows the spectrum of the Lake Chichancanab record. The large peaks have been highlighted with arrows and the corresponding frequency has been converted to period. To verify that the signal peaks observed in this data set are significant and not due to sensor error or some other confounding variable, null hypothesis testing was performed. Using the built-in MATLAB Auto-Regressive estimator an AR(2) model was fit to the Lake Chichancanab data (orange line). An AR(2) process was chosen as testing with AR(1) processes showed it could not adequately reproduce the observed spectra. The variables for the model used are: $\sigma = 0.4641$, $\rho_1 = 0.91403$, and $\rho_2 = 0.0855441$; where σ is the variance, and ρ_1 and ρ_2 are the first two autoregressive parameters. The 95%

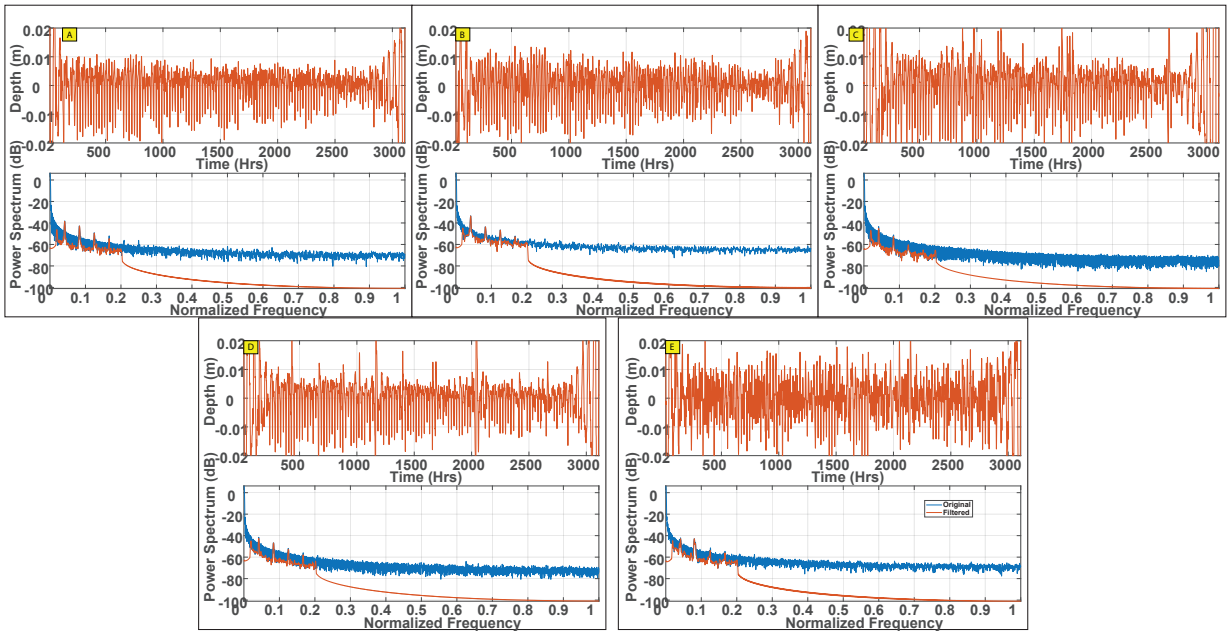

Figure 3.3: Bandpass filtered data from the sensor locations. The top panel shows the filtered data while the bottom shows the before and after spectra. (A) Hacienda Chukum, (B) Sotuta de Peon, (C) Lake Chichancanab, (D) Lake Pac Chen, (E) Lagoon Campechen.

	Chukum	Sotuta	Chichancanab	Pac Chen	Campechen
Chukum	N/A	1.34 h	0.75 h	-1.0 h	0.08 h
Sotuta	-1.34 h	N/A	-0.51 h	-1.75 h	-0.26 h
Chichancanab	-0.75 h	0.51 h	N/A	-1.55 h	0.3 h
Pac Chen	1.0 h	1.7 h	1.55h	N/A	0.3 h
Campechen	-0.08 h	0.26 h	-0.3 h	-0.3 h	N/A

Table 3.1: A table of lag times for the diurnal period calculated using wavelet coherence. Negative numbers indicate the row lags the column.

confidence interval of this spectra is then drawn (red dashed line). The diurnal and semi-diurnal spikes are well above the 95% confidence level while the terdiurnal and overtide spikes are above the null spectra but below the 95% level.

To better understand the relationships between locations wavelet coherence analysis was conducted. This was used to calculate the lag times between locations at the diurnal period. Wavelet coherence was used as opposed to spectral correlation as it allows for specific periods to be considered as opposed to the entire signal for traditional spectral correlation. The calculated lag times between all the locations are presented in Table 3.3. The lags are calculated using the phase information from the cross wavelet spectrum which is then converted to lag time using the signal period (Grinsted et al., 2004). Figure 3.5 presents an example of the data used to calculate the lags. A clear 'band' of coherence can be observed at the 24 hour period (B). Another band, (though less clear) can be observed at the 12 hour period. There are also a few areas of longer period coherence in the $\sim$ 60 hour and $\sim$ 200 hour ranges. The lag value calculated in Table 3.3 can be considered an average of the phase arrows only within the 24 hour coherence band. Panel (A) of this figure compares the spectra of both the Lake Chichancanab and Lagoon Campechen locations. Note that the overall shape of the spectra is different (the slope of the average spectrum differs especially for frequencies under 0.1 cycles per hour) and it is the relative height of the peaks, not the absolute value which should be considered. Individual tidal constituents are visible in the Campechen spectrum at both the diurnal and semi-diurnal peaks. In contrast only select constituents appear in the Chichancanab spectrum and they appear to diminish as the frequency increases. At the diurnal frequency (0.0416 cycles per hour) there is a precise alignment at the primary tidal component, K_1, as well as at the secondary constituent, O_1. At the semi-diurnal frequency (0.0833 cycles per hour) the S_2 tide aligns precisely across the two locations, while the N_2 and M_2 constituents only appear as defined peaks at Campechen. This trend continues through the spectrum as peaks at the higher frequencies only show distinct spikes at the Campechen location.

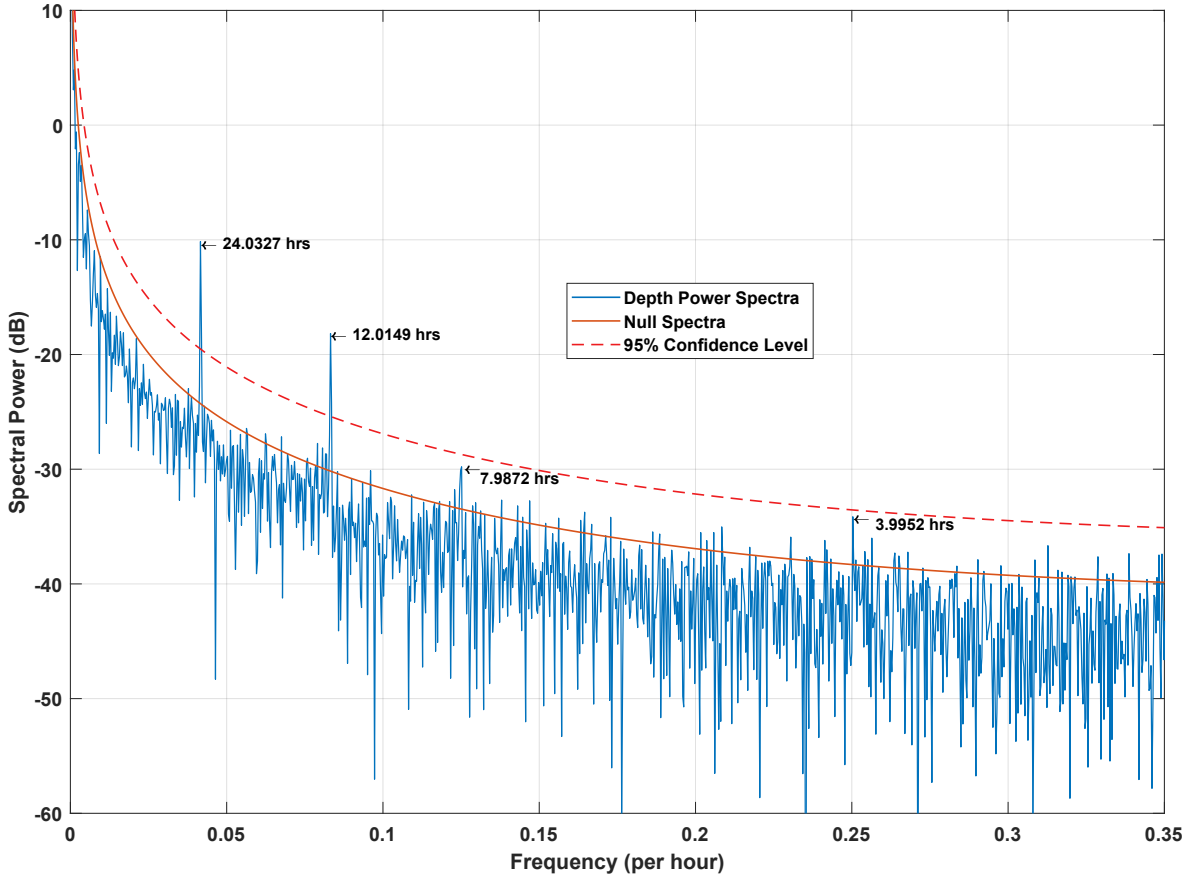

Figure 3.4: The power spectrum of the Chichancannab data. To verify the validity of the data a null spectra was created using an AR2 process which is shown in orange. The 95% confidence interval for the spectrum is then shown as a red dashed line. The diurnal and semi-diurnal peaks are well above the 95% confidence interval while the 8h and 4h peaks are above the null spectra.

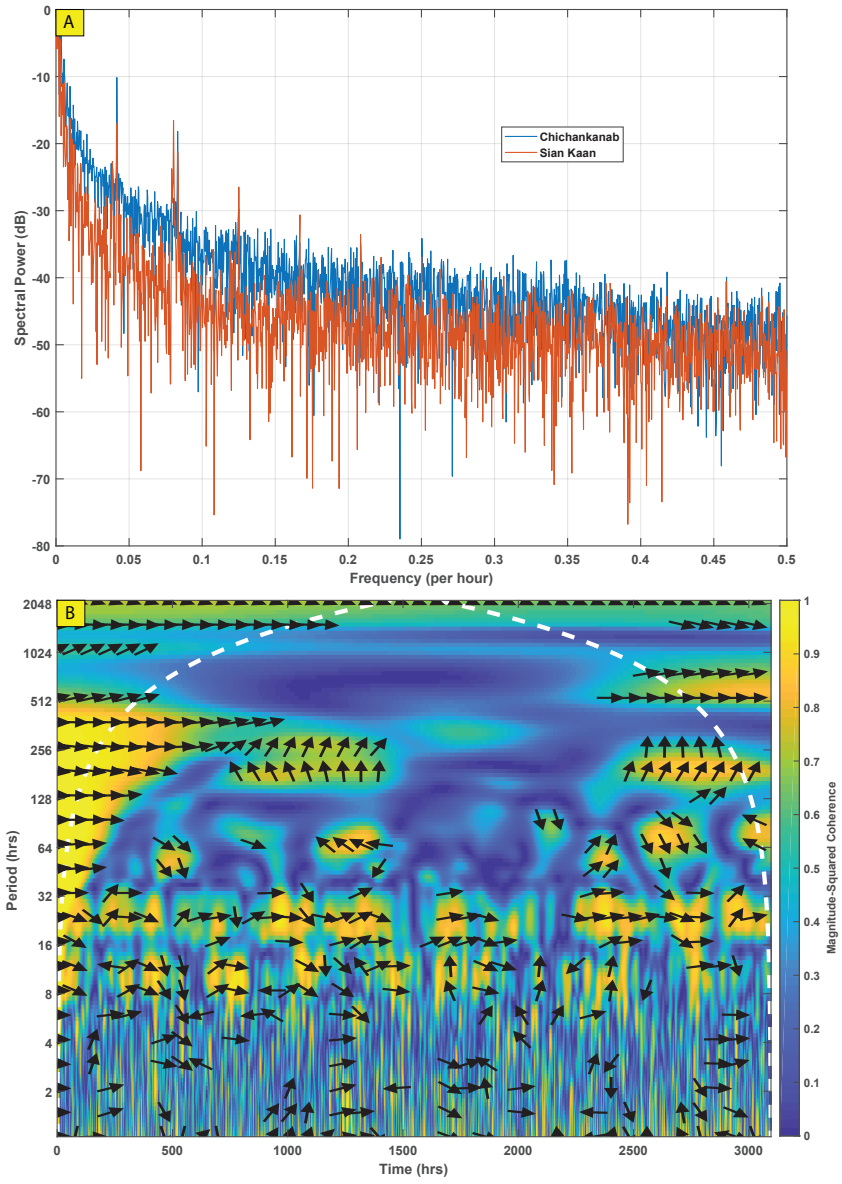

Figure 3.5: The top panel (A) shows the spectra for both Chichancannab and Campechen. Both appear to peak at similar values with small differences. The bottom panel (B) is the wavelet coherence which indicates the correlation between the signals at different periods. The arrows overlain indicate phase shifts in their coherence. Note the bands at 24h and 12h as well as the rightward facing arrows indicating that the signals are in phase.

3.4 Discussion

Figures 3.2 and 3.3 clearly indicate that tidal oscillations are present at all sampling locations. This is particularly impressive given the large distances that these locations are from the coast (from 100 m to 100 km). While traditional theory does not predict that tidal effects should be observable (Beddows, 2004), we would argue that the presence of large scale fractures, i.e. cave networks, allows for efficient and long distance transport of the tidal signals deep into the peninsula's interior. This is based on all the inland sites being located relatively close to large scale fracture zones, however more research is needed to determine if this is the case. Previous research in the geologically similar Florida Peninsula has shown that the presence of large scale conduits can decrease the decay rate and increase the propagation speed of the tidal oscillations by up to 100 times (Loper and Chicken, 2008; Loper and Eltayeb, 2010). Propagation of tides through the cave networks may also explain why studies that have taken measurements from boreholes within the karst matrix have not detected tidal oscillations (Šafanda et al., 2005; Gondwe et al., 2010). While not academically verifiable, it can be noted that the Wikipedia page for Lake Chichancanab records anecdotal evidence of a local legend that tells of a great sea serpent that is responsible for tides in the lake https://es.wikipedia.org/wiki/Laguna_Chichankanab, indicating that for the local population at least, tides within this lake are a known phenomenon. The longer term water level changes at all the geographically separated sites follow a seasonal (wet–dry) oscillation, with a minimum water level in September and a maximum in late November. This pattern corresponds to seasonal changes previously observed in the groundwater (Kovacs et al., 2018); a connection that was previously noted in the isolated context of Pac Chen (site (D)) (Krywy-Janzen et al., 2019).

The results of the bandpass filter (Figure 3.3) indicate that the locations can be separated into three groups, the relatively enclosed and less variable cenotes ((A) and (B)), the medium variation open lakes ((C) and (D)) and the highly variable open ocean/lagoon (E). These differences can be attributed to wind forcing on the free surface when comparing open locations ((C), (D) and (E)) to closed locations ((A) and (B)). As well, reduction in amplitude at the inland locations can be attributed to a weakening of the tidal signal through longer propagation in rough channels. It can be noted that despite these differences, all locations have the the same underlying signal, which can be seen in the spectrum (Figure 3.3; bottom panels).

From the statistical significance testing (Figure 3.4) it is clear that the diurnal and semi-diurnal signals are well above the 95% confidence level. This provides very strong and quantifiable evidence that the observations are due to oceanic tides. Other possible sources of the signal are considered in the commentary section. This is further strengthened

by the presence of higher tidal harmonics that, while not above the 95% confidence level, still provide evidence that these are tidal signals.

This result has a significant impact on our current understanding of the hydrology of the peninsula. Where previously geoscientists would consider in-land water bodies separate from the larger aquifer they must now consider this connection. For example, given current sea-level rise and the connection between these inland water bodies and the aquifer (and thus sea-level), it would appear likely that these water bodies will flood in accordance with projected sea-level rise. This connection can also function in the land-to-sea direction, and any contaminants released into one of these 'isolated' water bodies have potential to outflow to the coastal waters and impact water quality. More research is needed to understand the extent of the connection, and local implications (e.g. due to conduit outflows near reefs). Furthermore, it is likely that should tidal signals be propagating along fracture zones and areas of high permeability, that these regions would likely have lower water quality than lower permeable areas due to enhanced mixing. Again, further investigations are needed to confirm these effects on a landscape level.

While we are confident in our result that we have identified tides within all our locations, aspects of this tidal propagation still remain unknown. Based on the lag data (Table 3.3), it appears that the tide first occurs at the Pac Chen location and last at the Sotuta location. This does not appear to have any relation to distance from the coast. One relevant factor is that the tidal signal in this region propagates clockwise around the peninsula, with tide first rising in Campeche then along the northern coast, and finally down the eastern coast (see arrow in Figure 3.1). Moreover, in more permeable areas along the coast the tidal signal can reach further inland faster than in more impermeable areas (Loper and Eltayeb, 2010). Taken together the two lead to a complex pattern, that could explain the lack of a clear direction of tidal propagation inland. This especially complicates using previous research on homogeneous tidal propagation theory (Ferris, 1951; Jacob, 1950; Trefry and Johnston, 1998; Trefry and Bekele, 2004) in this region. A further issue with the lags is that should the lag period be longer than the period of the longest tidal constituent, it will not be possible to differentiate it from shorter lags. Once option could be to consider longer period signals such as spring-neap tides. Further research is needed to fully understand the tidal propagation within the peninsula.

The spectra of Chichancanab and Campechen (Figure 3.5 (A)) provide a fascinating comparison. Of interest is the difference in the overall shape of the spectra. Chichancanab has a much broader spectrum likely due to the smaller amplitude of oscillation leading to a more significant noise contribution compared to Campechen. It can be noted that while the diurnal band appears to stay in-phase for the whole record (always rightward facing arrows in the 24 hour band), the semi-diurnal band exhibits a changing lag (arrows change

angle over time in the 12 h band). Based on these results higher frequency signals appear to be lost or suppressed when propagating inland.

3.5 Conclusions

Based on the results presented in this article, tidal effects are expected throughout the inland waters of the Yucatan Peninsula. Even the most inland location (Lake Chichancanab) shows a distinct, statistically significant tidal signature, and we can state with confidence that these locations have some degree of larger scale groundwater connection.

This effect has important implications for various fields of study in the region, including paleoclimate reconstructions, geological investigation, engineering development and groundwater protection. Specifically, sediment core paleoclimate reconstruction studies have previously made the assumption that these inland water bodies are hydrologically isolated (Curtis et al., 1996; Douglas et al., 2015; Hodell et al., 1995, 2005a,b; Kennett et al., 2012; Medina-Elizalde et al., 2010). These previous results may have to be reinterpreted given the current results. It is possible that the interchange of these water-bodies with the aquifer, and thus marine water, is sufficiently limited to result in lake proxies accurately recording changes to evaporation / precipitation. However, a non-linear modulation is also a clear possibility. For example, it is possible that this connection is responsible for some of the differences in correspondence between proxy records of the Holocene that have been gathered from this region (Douglas et al., 2016). More site specific studies that quantify the degree of interchange between the water body and the aquifer are necessary to elucidate these effects and we leave this to future work.

We have quantified the lag times between the sampling sites and found that there is no clear relationship between distance in-land and lag time. A plausible explanation for this is that there are regions of high permeability in the peninsula that allow for enhanced propagation of the tidal signal, and that propagation of the tide along the coastline is not uniform (see arrow in Figure 3.1). More research is needed to better understand tidal propagation within the peninsula, and whether previous research on composite heterogeneity (Trefry and Bekele, 2004) is applicable in this region. Future work could also include extending sensor coverage across the peninsula to create a more granular map of lag times.

Future studies will continue to measure the extent of groundwater connection within the peninsula, mapping the extent of connectivity and its relationship to the large fracture networks. However, there is an important theoretical issue, since the traditional mathematical descriptions, whether based on Darcy's Law or Richards' Equation, do not apply to

open conduits with cross sectional areas on the order of meters squared. In these situations to correctly describe the dynamics a new approximate theory, based on the full stratified Navier-Stokes equations will need to be developed.

3.6 Commentary

The previous material in this Chapter has been accepted for publication in Geophysical Research Letters (GRL) as:

Coutino, A., Stastna, M., McNeill-Jewer, C., and Reinhardt, E. G. (2021). Inland tidal oscillations within the Yucatan Peninsula. Geophysical Research Letters, 2020GL092091.

The material in this chapter differs slightly from the submitted manuscript due to length limitations: in the submitted manuscript the discussion of Figure 3.3 was moved to an appendix and some wording was changed. These length limitations are also why much of the introductory and background material was not included in the article and is instead included in Chapter 2.1 of this thesis. As was highlighted in Section 3.5 the primary motivating factor for this research was its implications for paleoclimate proxies. Previous paleoclimate records from lakes in the northern lowlands of the Yucatan Peninsula have assumed that the lakes were closed or perhaps leaky basins (Curtis et al., 1996; Douglas et al., 2015; Hodell et al., 1995, 2005a,b). Proxy records including microfossils, isotopic and sediment composition have been used to document the effects of relative wet/dry periods spanning the Holocene and during the Classic Maya decline (Douglas et al., 2016). During dry periods evaporation would cause draw-down of the lake water levels which would be recorded in the δ^{18}O from microfossils (e.g. Punta Laguna; Curtis et al. (1996)) but also the precipitation of gypsum in Laguna Chicancanab (Hodell et al., 2005a). However, as Krywy-Janzen et al. (2019) has shown, water levels track Holocene sea-level rise. Instrumental water-level monitoring reported by the same authors showed a semi-diurnal tidal cycle, indicating that lake Pac Chen was connected to the aquifer. Currently the thermal stratification of the epliminion suggests that mixing between lake and aquifer water is incomplete, however this may have been different in the past with wetter or drier conditions and changing sea-level. Further research is required to understand this interaction between aquifer and lake water, but there does not appear to be a significant draw-down of lake levels during the Classic Maya droughts and lake water maybe buffered by the aquifer thereby affecting its isotopic composition. The current study, which includes more lakes in the northern lowlands, indicates that connectivity with the aquifer is more widespread than currently thought and that fractures and spatial variation in groundwater hydrology (i.e. permeabilities) may play a role in paleoclimate records from water bodies of

the Yucatan Peninsula. Showing a high degree of connectivity with the aquifer and ocean would not invalidate these previous findings but complicates the relationships between the sediment records and inferred climate records. Other novel contributions include the discussion of moving tidal input (i.e. the way in which the tides propagate around the Yucatan peninsula) which does not appear to have been discussed in the literature. This issue can only arise in large karstic platforms such as the Yucatan Peninsula or the Florida Peninsula that are porous enough to allow for deep tidal propagation and large enough that the timing of the tides is not uniform along the kart platform's boundary. This is in stark contrast with work such as Trefry and Bekele (2004), where due to the small size of the island, the tide can be assumed to occur simultaneously along the entire boundary.

On a smaller scale it is possible to only consider the tides from the closest coast to investigate tidal propagation. Unpublished work was done using the sensors from Yax Chen (the same sensor locations from Chapter 2.4). The sensors were located at a depth of 2 m and measured salinity, temperature and water level. The records that were used spanned from May 2016 to May 2017. See Figure 2.2 for sensor placement locations. The diurnal lag time was calculated using wavelet coherence between the locations, this was then used along with estimated distance between locations to calculate an approximate propagation speed. Estimates appeared to be consistent around 4 m/s. This matches estimates of 4.4 m/s calculated by Loper and Chicken (2008) for karst waves in Florida, as mentioned in the introduction this is despite the ill-posedness of their model.

We can attempt to account for the propagating nature of the tide, and thereby elucidate aspects of the connection between our locations and the coast. This can be accomplished by calculating the timing between tidal oscillations at our location and the closest coast. As tidal data at these closest points along the coast is not available, we will use the Campechen tidal data and phase shift the record back an appropriate amount of time to match where the signal would have been at closest approach. Using tidal data from Campeche and Cozumel, tidal oscillations occur 6 hours apart and the distance along the coast from these locations is roughly 600 km. This corresponds to a velocity of roughly 100 km/h in the clockwise direction around the peninsula. We can then calculate the delay for tidal peaks from Campechen at the locations around the coast of closest approach for each inland location. For example, the closest point along the coast to Pac Chen is between Tulum and Playa del Carmen located roughly 50 km in the counter-clockwise direction from Campechen. We thus need to shift our record by 0.5 h and then calculate the lag between this shifted record and the Pac Chen record. For the Chichancanab record the closest coast is past Campechen clockwise, we can then shift our record in the opposite direction. The lag time can also be combined with the distance to the coast to calculate a propagation speed. The calculated values for each locations are presented in Table 3.6. All

	Chukum	Sotuta	Chichancanab	Pac Chen
Distance Lag	-1.17 h	-0.85 h	-0.33 h	-0.42 h
Distance	90 km	60 km	100 km	40 km
Speed	77 km/h	71 km/h	300 km/h	95 km/h

Table 3.2: Lag times, distance from the coast, and propagation speed between inland locations and calculated tide at closest coast.

locations have a negative lag time indicating that the tide is occurring first along the coast (which should be expected). The northern locations (Chukum, Sotuta, and Pac Chen) all provide a relatively consistent, reasonable results. However there is a clear outlier in Chichancanab. Despite being the furthest inland location it had the lowest estimated lag time. This results in an unreasonable speed which either indicates an error in the method (which is somewhat naive) or that unlike the lowland locations the tide at Chichancanab is not driven by rate of change at the nearest coastal connection. Other confounding issues are that Chichancanab is located at the transition zone from the Mayan lowlands to the Mayan highlands, as well as the geological transition from Mio-pliocene limestone to Eocene limestone.

While not discussed in the main text, another possible explanation for the tidal signal measurements from the inland locations could be Earth tides (ET). These are tidal oscillations induced directly in the groundwater by the gravitational forcing from the Moon (McMillan et al., 2019). Generally these induced tides are very small with oscillations on the order of micrometers (McMillan et al., 2019). This does not match with the centimeter oscillations we have observed from our field locations but may account for part of the variation. However, ETs are an aquifer wide effect. This implies that even if we assumed that our observations were due to ETs, there would have to be a connection at our locations (and especially at the 'lake-like' locations) to the larger aquifer which is the conclusion we make. Thus while ETs may play a role in the water level variation at these inland locations, their presence or lack thereof, does not change the take home message of the article that some level of hydrologic connectivity exists between these inland water bodies and the larger aquifer.

Chapter 4

Mixing in the Cave Newtorks

4.1 Introduction

The Yucatan Peninsula (165,000 km^2) encompasses three Mexican states (Yucatan, Quintana Roo and Campeche) and is composed of Miocene to Late Pleistocene limestone which has undergone intense dissolution creating a karst topography (Weidie, 1985; Perry et al., 2003; Bauer-Gottwein et al., 2011). The high porosity of the limestone (14-23%) (Beddows et al., 2007) results in few surface water bodies as rainfall quickly infiltrates through the limestone and into the unconfined aquifer which flows towards the coast through networks of caves and fracture zones (Emblanch et al., 2003; Stoessell, 1995; Beddows et al., 2007).

The Yucatan aquifer has a stratified structure due to fresh rainwater percolation into the subsurface which creates a density-stratified fresh lens (the meteoric water mass, or MeWM) above the saltier marine water (the marine water mass, or MaWM) that intrudes inland from the coast (González-Herrera et al., 2002; Gondwe et al., 2010). The interface between the two water masses is a generally thin (1-3 m) mixed brackish layer of intermediate salinity called the halocline that increases in vertical extent as it approaches the coast (Bauer-Gottwein et al., 2011). This stratification is well-documented for many coastal systems especially given a porous coastal geology (Cooper et al., 1964), though the hydrodynamics of this system are still not fully understood. For example, there is little to no data on macro-scale dynamics occurring within larger caves and conduits. While several groundwater models exist for coastal-ocean geographies (Jones et al., 2000; Sanford and Konikow, 1989), they typically assume that the region of interest has a homogeneous porosity (Hubbert, 1940; Wilson, 2005). However, due to the presence of the fractures, and

in particular the large scale cave networks, this is not the case in the Yucatan Peninsula (Kambesis and Coke, 2013).

Understanding the hydrodynamics of the aquifer is particularly important for wastewater management given the exponential growth in tourism along the eastern coast and the growth of factory-style poultry and hog farms in the northwestern and central regions (Perry et al., 2009; Novelo et al., 2009). This increase in inland contaminant sources have already resulted in deteriorating coastal conditions (Herrera-Silveira et al., 2004). Of particular interest is the mixing that occurs between the MaWM and the MeWM, which was first documented in (Coutino et al., 2017). In this paper, the authors found that heavy rainfalls resulted in increases in salinity within the MeWM which indicated the energy injected into the system by this heavy rainfall entrains the halocline and pulls up the MaWM, thereby mixing the upper water column. While Coutino et al. (2017) focused on the dynamics of the mixing, the companion paper, Kovacs et al. (2017), focused on extending the results to more spatial locations, and outlining the implications of the observational results for the study of sedimentation. Mixing induced by heavy rainfall has been further verified by other studies (Brankovits et al., 2018). However, despite reporting of these mixing events, very little understanding has been developed for the fluid dynamics of mixing events that occur within the cave passages throughout the region. Previous studies have measured velocities within these passages, from 1 cm/s far inland to 12 cm/s near the discharge point on the coast (Moore et al., 1992; Metcalfe et al., 2011). Other studies have focused on point measurements within the cave systems, for example, specific electrical conductance (SEC) (Beddows et al., 2007) or passively collected sediment samples (McNeill-Jewer et al., 2019). On a larger scale, several studies have attempted to calculate regional coefficients for potential use in regional models (Steinich and Marín, 1997; Stoessell, 1995). More recently, MODFLOW-CFP (Conduit Flow Process; (Shoemaker et al., 2005)) has been used to model groundwater dynamics in the YP. Martínez-Salvador et al. (2019) used MODFLOW-CFP to estimate pollutant residence time in the vicinity of Merida, Mexico. According to the authors this is the first time that a groundwater model has been applied to that region. It remains to be seen how well the model works in other regions of the peninsula. This extension of MODFLOW couples the groundwater model with a pipe network that represents the conduits. The model has previously been used for sub-regional scales within the Florida aquifer (Gallegos et al., 2013) which has a similar geology to the Yucatan Peninsula.

The mixing that occurs within these passages is particularly interesting from a fluid dynamics perspective as the water in the cave is a double diffusive system. Double-diffusion refers to a system whose density depends on two parameters that have different diffusivities. In the majority of cases they are salt and heat (for examples of other types of double

diffusive systems see (Özgökmen et al., 1998; Boehrer et al., 2009)). These two components have very different diffusivities; κ_s the diffusivity of salt is only 1% the diffusivity of heat. As a result, the fluid may be stably stratified in one parameter, but unstably stratified in another. For example, when salinity, the less diffusive tracer, increases downwards, but temperature, the more diffusive tracer, increases downwards (less dense, cool, fresh water above denser, warm, salty water), if a small parcel of fluid from the lower layer is slightly perturbed upwards, it will lose heat to the fresh layer, while retaining its salinity. This causes the parcel to increase in density and sink back towards (and eventually overshoot) its initial state, resulting in an oscillation. This type of instability is often referred to as an oscillatory instability. This is also the primary regime within the cave systems as the MaWM is warmer than the rain-fed MeWM. In the opposite configuration, when a layer of lighter, hot, salty water rests over top of a layer of heavier, cool, fresh water, heat from the upper layer diffuses into the lower layer much more quickly than salt. As parcels of fluid just above the interface decrease in temperature, they increase in density, resulting in locally unstable density gradients. This causes the heavier, salty parcels to sink, forming long, thin convective cells called salt fingers. These fingers experience an additional lateral loss of heat to the fresh water, further increasing their density (Kundu et al., 2011).

The dynamics of double diffusion was first explained by Stern (1960) in the context of ocean thermo-haline circulation. Over time double diffusion has also been found to be relevant in thermosolutal convection for crystal growth (Kamotani et al., 1985), and in stellar convection (Rieutord and Espinosa Lara, 2013). Most observational studies of double diffusion have been in the context of the ocean's thermo-haline circulation (Williams, 1975; Schmitt et al., 1987; Schmitt, 1994; Stranne et al., 2017), however there have also been observational studies on double diffusion in deep meromictic lakes (Boehrer et al., 2009). Early experimental studies on double diffusion were done by (Turner, 1965, 1967) who proposed a possible mechanism for the formation of thermohaline staircases. Linden (1974) was responsible for discovering the organization of salt fingers into sheet-like structures arranged in the direction of imposed shear. Other experimental studies have examined various phenomena such as intrusions (Turner, 1973; Ruddick et al., 1999) and measuring various buoyancy fluxes and eddy diffusivity parameterizations (McDougall and Taylor, 2009; Wells and Griffiths, 2002, 2003).

Direct numerical simulation (DNS) allows for a more detailed analysis of flows that are difficult to measure in laboratory experiments. With DNS it is possible to analyze and probe the entire flow using any number of relevant quantities (e.g. tracers, velocity, density, vorticity) as opposed to measurements from a single probe, or an instrument chain. Numerical simulation also affords a greater degree of control on experimental parameters, and allows for the parameter space to be explored. However, the small-scale features that

form as a result of mixing require sufficiently fine grid spacing to ensure proper resolution, which necessitates a large number of grid points and significant computational resources. Several studies have explored double diffusion numerically (Piacsek and Toomre, 1980; Piacsek et al., 1988; Shen, 1997; Özgökmen et al., 1998; Ozgökmen and Esenkov, 1998; Radko, 2003; Sommer et al., 2014). However, many of the earlier studies could not afford sufficient grid resolution which may have resulted in numerical diffusion that affected the results, for example 201 $\times$ 201; over 1 m $\times$ 2 m for a minimum resolution of 4.9 mm (Özgökmen et al., 1998). In recent years, higher resolution simulations of these systems have been considered, Kimura and Smyth (2007) carried out simulations with a Prandtl number of 7 and a diffusivity ratio of 0.01, they had a resolution of 6144 $\times$ 144 $\times$ 3072, which given the size of the simulation domain gave a resolution of about 1.3 mm. Carpenter et al. (2012) considered simulations with Prandtl number 6.25 and diffusivity ratio of 0.01, and a resolution of 320 $\times$ 320 $\times$ 640 which, given the size of their simulation domain, gives a resolution of 1 mm per point. In general the numerical scheme for these models vary, Kimura and Smyth (2007) and Carpenter et al. (2012) used pseudospectral methods. For these methods the order of accuracy increases with increasing resolution (Trefethen, 2000), allowing for confidence in numerical accuracy. Earlier work generally used lower-order finite difference methods due to the computational resources at the time.

Another important aspect of analyzing DNS is quantifying the evolution of energy components, and thereby understanding how the dynamics are manifest through movement of energy. The traditional energy framework found in works such as Winters et al. (1995) was extended to double diffusive systems by Middleton and Taylor (2020). The authors developed a criteria to quantify the transfer of energy from the background potential energy (BPE) to available potential energy (APE) based on the angle between the gradients of temperature and salinity, and the diffusivity ratios. Transfer of energy from BPE to APE is not possible in a single-component fluid with a linear equation of state. The finding that BPE can be converted into APE within double diffusion implies the interpretation of the APE from Winters et al. (1995) does not hold for a double-diffusive fluid. In particular this complicates the definition of 'mixing efficiency' as it is commonly calculated Gregg et al. (2018). However one issue with this framework is that it only applies to a linear equation of state, should nonlinear effects become important (generally close to $4°C$) this framework would not be applicable.

The simulations that have been discussed above are primarily concerned with double diffusion in the oceans, there are a different set of problems that arise when considering double diffusion within cave conduits; for example the effect of the cave walls, the presence of strong shear flows and different temperature and salinity ranges. Our approach has been to focus on double diffusion with temperature and salinity values informed from

measurements. We focus on a region at the halocline away from any side walls and with no shear flow. While not entirely realistic, as the measurements we based the simulation parameters on were following a hurricane thus there likely is shear flow within the conduit, approximations must be made and this study can act as a building block for further investigations.

4.2 Methods

The initial conditions for our simulations were motivated by sensor measurements collected during 2013 (Coutino, 2016). For that study sensors were arranged in a vertical chain that intersected the halocline, see Figure 4.1. Two HOBO conductivity sensors were located above the halocline at 9 m depth and 10 m depth. Following a hurricane in September 2013 an unstable density stratification (the density was greater at 9 m than 10 m) was observed in the weeks following the event. Due to the persistence of this unstable density configuration for a significant amount of time it was hypothesised that this was likely due to some sort of sensor error. However it can be easily imagined that this type of density configuration could occur naturally, though how long it would persist before it would mix to a stable configuration remains an open question. We thus use this observation as motivation for the initial conditions in our set up.

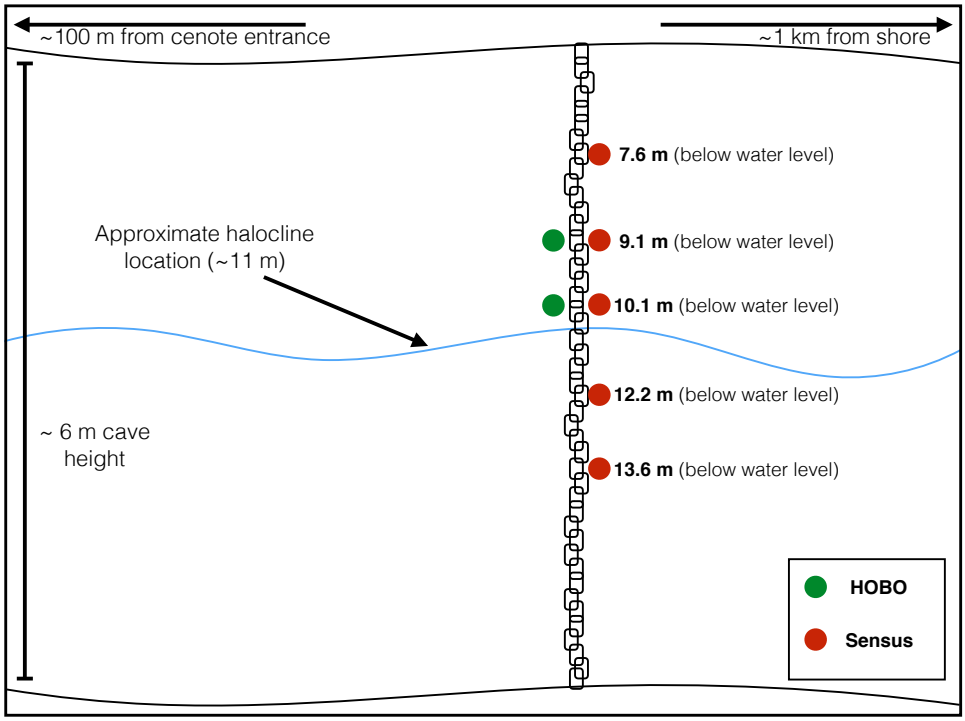

Figure 4.1: Schematic of the sensor chain within the cave system used in Coutino (2016)

As stated before, for the numerical simulations considered we will be restricting our focus to one of the many large conduits where we assume that the walls are sufficiently far away for boundary effects to be ignored (conduit diameters are typically on the order of meters to tens of meters). We further assume that the halocline is present within this cave section. These assumptions match the known cave passages at Isod 2 where the original measurements were taken (Figure 4.1). In this open section of the cave network, the governing equations are the Navier-Stokes equations. We adopt an idealized geometry, and since density variations are on the order of 1% or less, we make the Boussinesq approximation. The governing equations are written as

$$\frac{D\boldsymbol{u}}{Dt} = -\frac{1}{\rho_0}\nabla p - \frac{\rho g}{\rho_0}\hat{\boldsymbol{k}} + \nu\nabla^2\boldsymbol{u}, \tag{4.1}$$

$$\nabla \cdot \boldsymbol{u} = 0, \tag{4.2}$$

$$\frac{DT}{Dt} = \kappa_t \nabla^2 T, \tag{4.3}$$

$$\frac{DS}{Dt} = \kappa_s \nabla^2 S, \tag{4.4}$$

$$\rho = f(T, S), \tag{4.5}$$

where $\frac{D}{Dt} = \frac{\partial}{\partial t} + \boldsymbol{u} \cdot \nabla$ is the material derivative, $\boldsymbol{u}$ is the vector of velocities, T is the fluid temperature, S is the fluid salinity, ρ is the fluid density, ρ_0 is a constant reference density, p is the pressure, g is the acceleration due to gravity, μ is the dynamic viscosity, f is a non-linear equation of state given below

$$\rho(T, S) = c_1 + c_2 T + c_3 S + c_4 T^2 + c_5 ST + c_6 T^3 + c_7 ST^2 \tag{4.6}$$

where $c_1 = -9.20601 \times 10^{-2}$, $c_2 = 5.10768 \times 10^{-2}$, $c_3 = 8.05999 \times 10^{-1}$, $c_4 = -7.40849 \times 10^{-3}$, $c_5 = -3.01036 \times 10^{-3}$, $c_6 = -3.32267 \times 10^{-5}$, and $c_7 = -3.21931 \times 10^{-5}$ (Brydon et al., 1999). Note that the coefficients have different dimensions, though these are easily determined from the polynomial equation of state. κ_t (κ_s) is the thermal (saline) diffusivity (see (Kundu et al., 2011) for a derivation and further discussion). These equations were solved using the pseudospectral incompressible Navier Stokes equation solver (SPINS) (Subich et al., 2013). The solver is a fully-parallelized code which can solve the incompressible Navier-Stokes equations with spectral accuracy (i.e., the order of accuracy of the simulation scales with the resolution (Trefethen, 2000)).

For our specific numerical simulation, we imposed free-slip boundary conditions along all boundaries because of our interest in the dynamics of the interior of the fluid, and the pycnocline region in particular, as opposed to details of the boundary layer dynamics (which will be quite complex in the cave network). Periodic BCs in x were also tested. This was also done to ensure a reasonable computation time. The physical dimensions of the tank were chosen to be 0.512 m in the horizontal and 1.024 m in the vertical (2^9 and 2^{10} respectively). Since we are expecting mixing to occur, we chose to use a high resolution, namely 2048×4096 (same ordering as the physical dimensions). This number of points provides a resolution of 2.5×10^{-4} m in all directions. This is sufficient for a direct numerical simulation (DNS) where we have resolved all scales and does not require a separate model for turbulence below the grid scale. This was not the case in the Sc833 case which used the Sc100 case resolution (this simulation was performed to test the limits SPINS, it was apriori known to be under resolved and its results should be taken with a grain of salt). This value of Sc=833 was chosen to use physical values for diffusivity. The primary physical parameters and simulation parameters for all the cases are presented in Table 4.1. As this was a preliminary investigation 2D simulations were considered sufficient to test computational approximations such as reducing the diffusivities and 'fudge' factor, however future studies should consider how the reported dynamics differ in 3D.

Initial conditions were given by

$$T = T_0 + \frac{T_{tr}}{2}\left(1 - \tanh\left(\frac{z - L_{mid}}{\Delta z}\right)\right), \tag{4.7}$$

and

$$S = S_0 + \frac{S_{tr}}{2}\left(1 - \tanh\left(\frac{z - L_{mid}}{\Delta z}\right)\right), \tag{4.8}$$

where T_0 and S_0 are the minimum temperature and salinity values ($25.5°C$ and 9 ppt), T_{tr} and S_{tr} are the changes in temperature and salinity through the transition ($1.5°C$ and 0.5 ppt), L_{mid} is the mid depth (0.512 m), and Δz is the width of the transition (0.1 m). The salinity and temperature are oriented such that there is warm salty water on the bottom and cooler fresher water on top.

There are a number of non-dimensional numbers which govern the dynamics of this system, they are: the Schmidt number, the Prandtl number, the Atwood number, the Reynolds number and the Froude number. Definitions for these numbers are given below and a table of these values for our simulations is provided in Table 4.2.

The primary variable was the Schmidt Number which is defined as,

$$Sc = \frac{\nu}{\kappa_S}, \tag{4.9}$$

where ν is the kinematic viscosity and κ_S is the diffusivity of salt.The Atwood number is defined as

$$At = \frac{\rho_1 - \rho_2}{\rho_1 + \rho_2} = 6.46 \times 10^{-3}, \tag{4.10}$$

where ρ_1 is the denser fluid and ρ_2 is the less dense fluid. At can be considered a measure of hydrodynamic stability.

$$Pr = \frac{\nu}{\kappa_T}, \tag{4.11}$$

where ν is the kinematic viscosity and κ_T is the diffusivity of temperature. Pr is equivalent to Sc but for temperature thus it can be considered a comparison of the rate of viscous diffusion to the diffusion of heat.

$$Re = \frac{UL}{\nu}, \tag{4.12}$$

where U is a typical velocity scale, L is a typical length scale and ν is the kinematic viscosity. Re is the ratio of viscous forces to inertia.

$$Fr = \frac{U}{\sqrt{gL}}, \tag{4.13}$$

where U is a typical velocity scale, g is the acceleration due to gravity and L is a typical length scale. Fr can be considered a ratio of inertia to gravitational forcing.

As mentioned above, the primary variable to be changed is Sc, since our aim is to determine whether common numerical 'shortcuts' could be applied to this situation and still accurately represent the mixing process. Nevertheless, the question remains as to the correct way to choose the velocity and length scale. One way to represent the quiescent, but unstable initial state is to define an instability timescale, and use this, along with a choice of length scale, to define U.

Consider a domain of height L that is unstably and linearly stratified, with a dimensionless stratification

$$\bar{\rho}(z) = 1 - \alpha z.$$

The linearized vorticity equation written in terms of the streamfunction ψ reads

$$\nabla^2 \psi_{tt} = \psi_{xx} \alpha g$$

where subscripts denote partial derivatives. From this, a simple time scale for instability exponentially growing instabilities an be derived by scaling, as we do here, or by solving the full linear instability problem. We have confirmed that the latter gives the same result, but do not wish to expand this departure from the main argument of this chapter more than necessary. The result in either case is

$$T_i = \frac{1}{\sqrt{\alpha g}}$$

where the subscript i denotes a time scale based on instability. From this result we have the velocity scale

$$U = \frac{L}{T_i} = L\sqrt{\alpha g}.$$

It remains to decide how to choose L. While somewhat *ad hoc*, we can choose L as the thickness of the unstably stratified layer in our numerical experiments. $L = 2\Delta z = 0.2$ m is a reasonable estimate for all of our numerical experiments.

The Reynolds number can thus be rewritten as

$$Re = \frac{UL}{\nu} = \frac{L^2/T_i}{\nu} = \frac{L^2}{\nu\sqrt{\alpha g}}$$

so that the Reynolds number of a particular case is set by how unstable the initial state is. The Froude number follows analogously.

Assuming appropriate time scales (advective, thermal and saline) are chosen, in their non-dimensional form the equations can be written as,

$$\frac{D\boldsymbol{u}}{Dt} = -\nabla p - \frac{1}{Fr^2}\hat{\boldsymbol{k}} + \frac{1}{Re}\nu\nabla^2\boldsymbol{u}, \tag{4.14}$$

$$\nabla \cdot \boldsymbol{u} = 0, \tag{4.15}$$

$$\frac{DT}{Dt} = \frac{1}{PrRe}\nabla^2 T, \tag{4.16}$$

$$\frac{DS}{Dt} = \frac{1}{ScRe}\nabla^2 S, \tag{4.17}$$

For each case that we simulated the relevant simulation parameters are listed in Table 4.1. Name is the simulation name, ν is the kinematic viscosity, κ_T is the diffusivity of heat, κ_S is the diffusivity of salt, Nx is the number of points in the horizontal, Nz is the number of points in the vertical, Lx is the horizontal domain size, and Lz is the vertical dommain size Additionally, Table 4.2 lists the nondimensional numbers associated with each simulation. It can be seen that the parameter regime of our simulations is relatively modest in Reynolds number, though this still allows for vigorous growth of the instability. The Froude number is subcritical in all cases, as expected. Initial noise was added to the velocity field at a magnitude of 1×10^{-6}.

Name	ν	κ_T	κ_S	Nx	Nz	Lx	Lz
sc100	1e-6 m^2/s	0.14e-6 m^2/s	1e-8 m^2/s	2048	4096	0.512 m	1.024 m
sc40	1e-6 m^2/s	0.14e-6 m^2/s	2.5e-8 m^2/s	2048	4096	0.512 m	1.024 m
sc20	1e-6 m^2/s	0.14e-6 m^2/s	5e-8 m^2/s	2048	4096	0.512 m	1.024 m
sc833	1e-6 m^2/s	0.14e-6 m^2/s	0.12e-8 m^2/s	2048	4096	0.512 m	1.024 m
fudge2half	2.5e-6 m^2/s	0.35e-6 m^2/s	2.5e-8 m^2/s	2048	4096	0.512 m	1.024 m
fudge5	5e-6 m^2/s	0.70e-6 m^2/s	5e-8 m^2/s	2048	4096	0.512 m	1.024 m
T95p	1e-6 m^2/s	0.14e-6 m^2/s	1e-8 m^2/s	2048	4096	0.512 m	1.024 m
T90p	1e-6 m^2/s	0.14e-6 m^2/s	1e-8 m^2/s	2048	4096	0.512 m	1.024 m

Table 4.1: The various simulation parameters for the cases that were carried out.

Name	Sc	Pr	At	Re	Fr
sc100	100	7.14	6.46e-3	$\approx 8.6e2$	≈ 0.003
sc40	40	7.14	6.46e-3	$\approx 8.6e2$	≈ 0.003
sc20	20	7.14	6.46e-3	$\approx 8.6e2$	≈ 0.003
sc833	833	7.14	6.46e-3	$\approx 8.6e2$	≈ 0.003
fudge2half	100	7.14	6.46e-3	$\approx 3.4e2$	≈ 0.003
fudge5	100	7.14	6.46e-3	$\approx 1.7e2$	≈ 0.003
T95p	100	7.14	3.5e-3	$\approx 6.4e2$	≈ 0.002
T90p	100	7.14	6.23e-4	$\approx 2.6e2$	≈ 0.001

Table 4.2: The corresponding nondimensional numbers for each of the simulations carried out.

4.3 Results

4.3.1 Evolution

The evolution of the Sc100 case can be seen in Figure 4.2. Small oscillations can be seen by $t = 100$s (panel (b)). These oscillations begin to expand by $t = 200$s (panel (c)) forming fingers of opposing density which increase the surface area of the interface region. These protrusions are eventually stretched and folded to generate the extremely complex interface seen at $t = 300$s (panel (d)). The extremely thin protrusion of with large density gradients, relative to the initial density transition zone, are what eventually results in numerical instabilities and/or excessive filtering at these values for the diffusivities.

To better understand the formation of the protrusions Figure 4.3 show both the com-

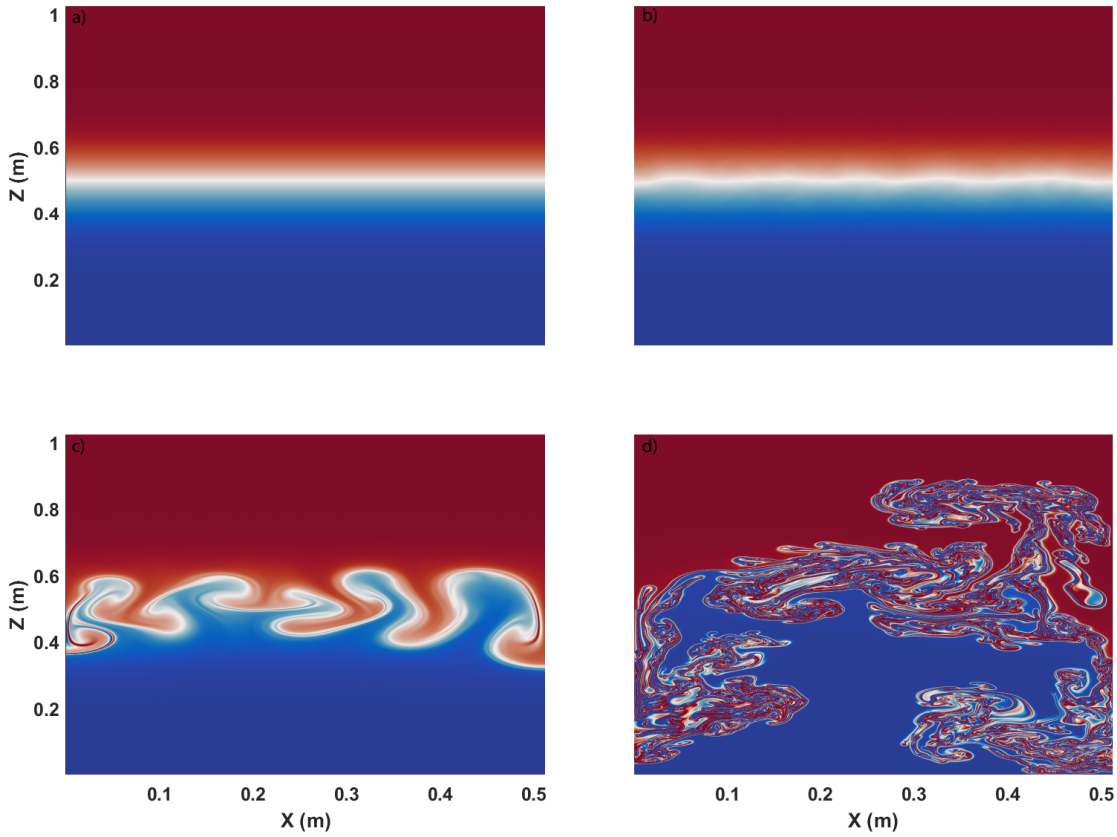

Figure 4.2: The density evolution for the Sc100 simulation (base case). The colour range has been set to between the initial max and min (3.6480 kg/m^3 and 3.6955 kg/m^3). (a) $t = 0$s, (b) $t = 100$s, (c) $t = 200$s and (d) $t = 300$s.

ponents of density, salinity (panel (a)) and temperature (panel (b)), in addition to the density (panel (c)). It can be noted that the salinity interfaces are markedly sharper than the temperature interfaces, due to the smaller diffusivity. It is also possible to identify regions of slight misalignment between the salinity and temperature field that result in the very sharp gradients in density.

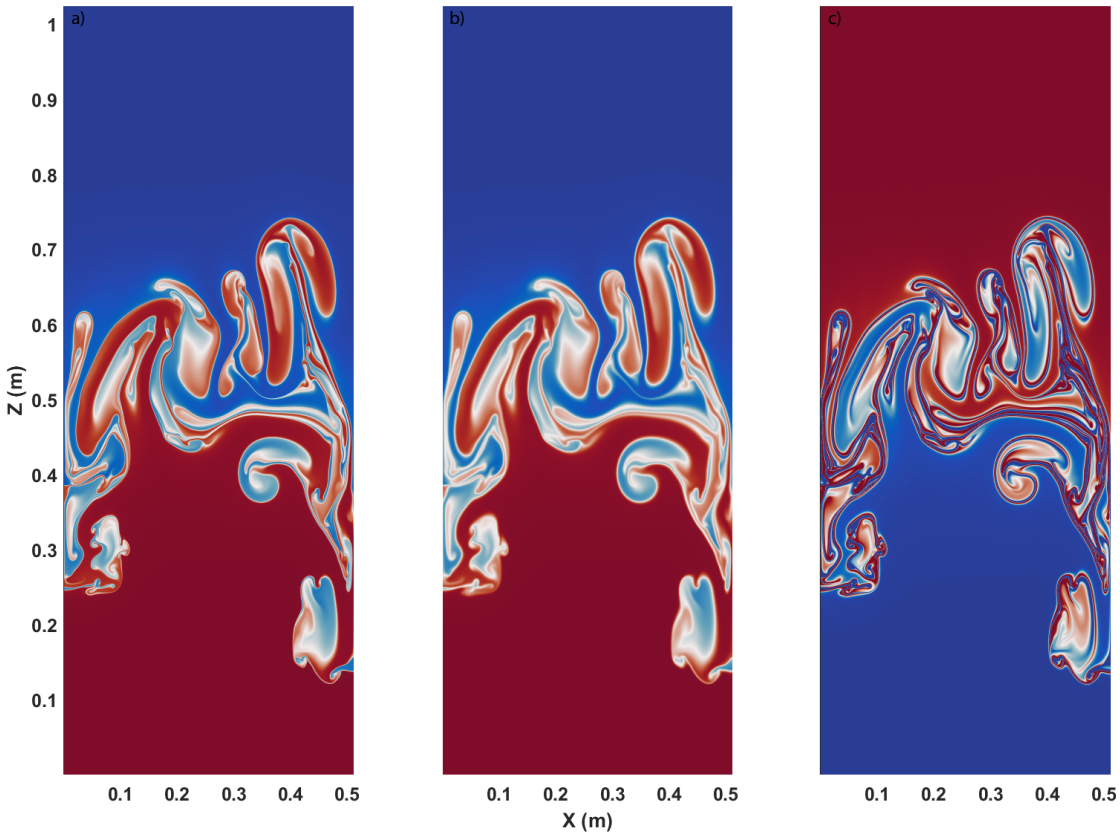

Figure 4.3: Salinity (a), temperature (b) and density (c) at $t = 250$s for the Sc100 case. The colour axis for each panel has been set by the initial variable range; 9 ppt to 9.5 ppt for salinity, 25.5°C to 27°C for temperature and 3.6480 kg/m^3 to 3.6955 kg/m^3 for density.

4.3.2 Sc Variation

The other Schmidt number cases follow the same evolution as case Sc100 (Figures **??**). The instability forms protrusions at the pycnocline, which eventually grow to create regions of higher or lower density surrounded by the opposite density perturbations. These fold, creating more gradients and eventually break down into turbulence. The effect of varying the Schmidt number can be most clearly observed at the density interfaces, which become more diffuse as the Schmidt number decreases. However by the final panel shown, the

interface breakdown appears very similar.

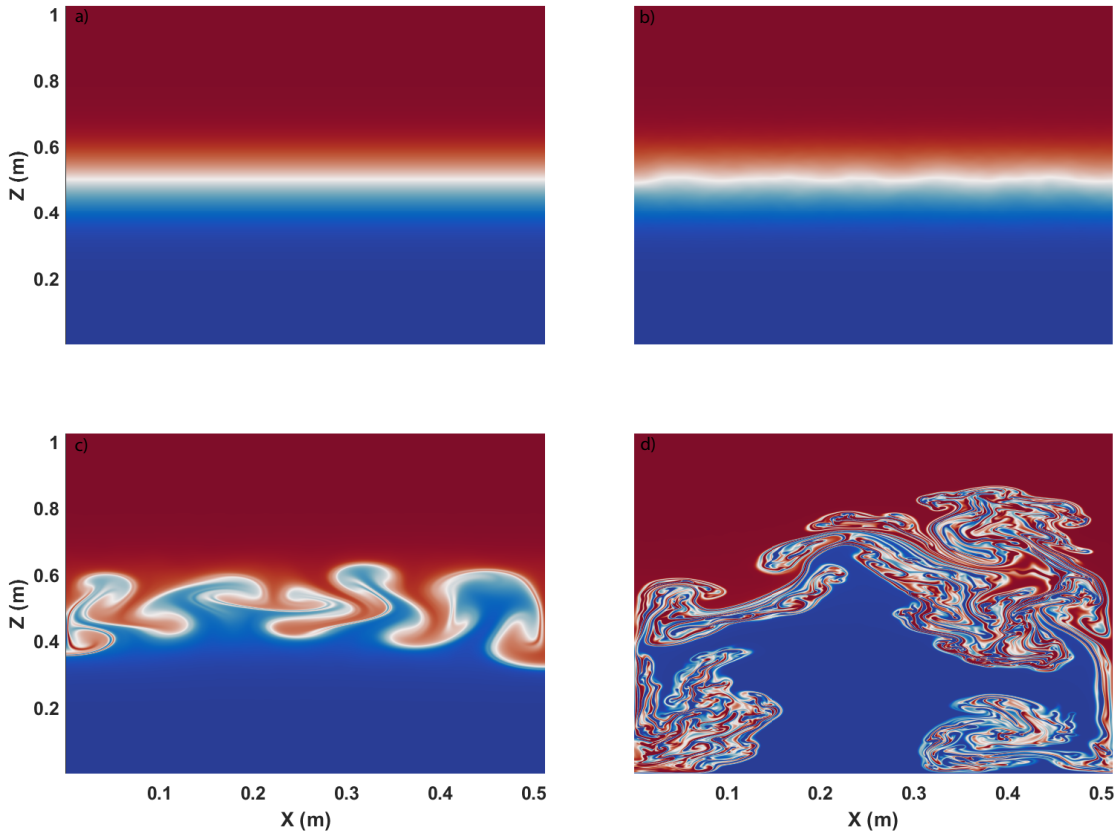

Figure 4.4: The density evolution for the Sc20 simulation. The colour range has been set to between (3.6480 kg/m^3 and 3.6955 kg/m^3). Panel (a) is $t = 0$s, panel (b) is $t = 100$s, panel (c) is $t = 200$s and panel (d) is $t = 300$s.

Dynamic differences can be observed when cases are compared at the same time. Figure 4.6 is the density field at $t = 250$ s for Sc20 (panel (a)), Sc40 (panel (b)) and Sc100 (panel (c)). While qualitatively similar, dynamically the lower Schmidt number cases are slightly further 'ahead' in their development. This is due to the change in timescales associated with salinity diffusion, though is complicated by the dynamics of the finite amplitude of the instabilities.

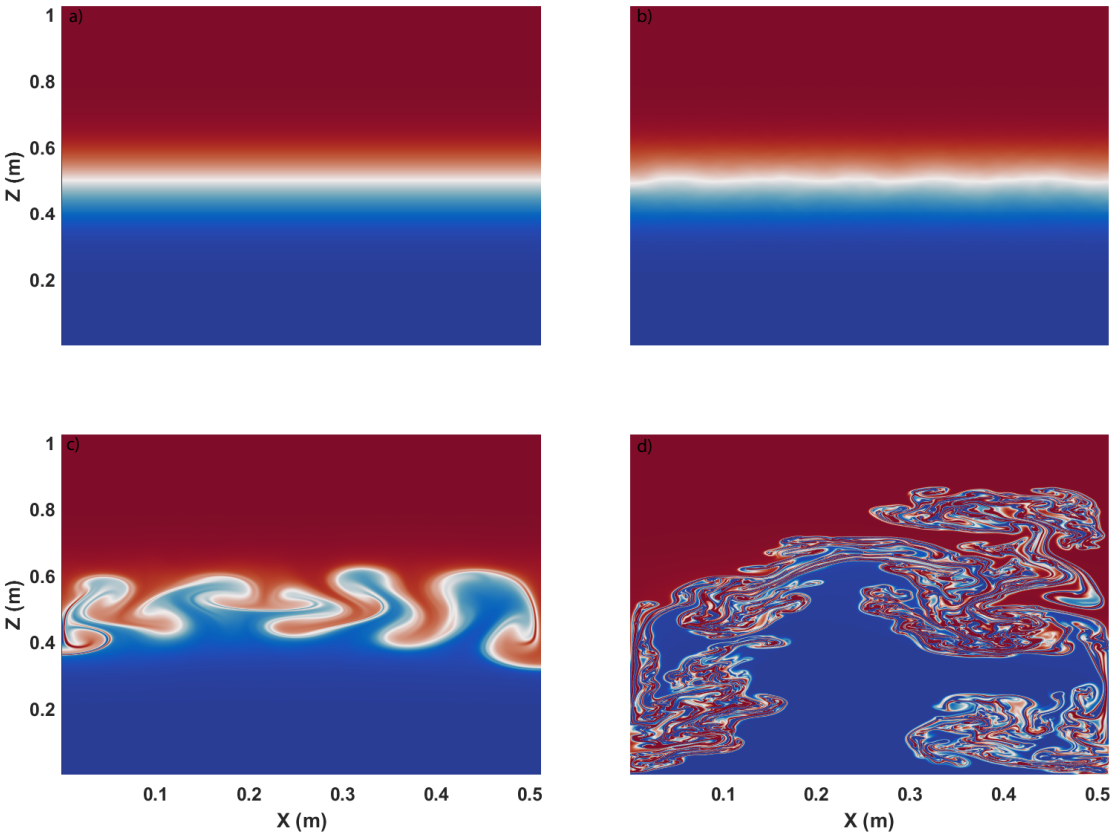

Figure 4.5: The density evolution for the Sc40 simulation. The colour range has been set to between (3.6480kg/m^3 and 3.6955kg/m^3). Panel (a) is t = 0s, panel (b) is t = 100s, panel (c) is t = 200s and panel (d) is t = 300s.

Figure 4.7 is a comparison of the horizontally integrated kinetic energy. The saturation of the colour axis has been set to 0.02 J/m^2 to show the relative intensity between thew cases. The vertical distribution of kinetic energy in all three cases appears very similar, the primary difference is in the intensity of kinetic energy. The lower Schmidt number cases exhibit a more energetic peak at t = 310 s near the bottom of the domain. This peak is associated with fluid being accelerated by gravitational forcing. Other slight differences can be observed in the vertical structure of kinetic energy near the final times. In the region above the mid-depth in both the Sc40 and Sc100 cases there are two local maxima,

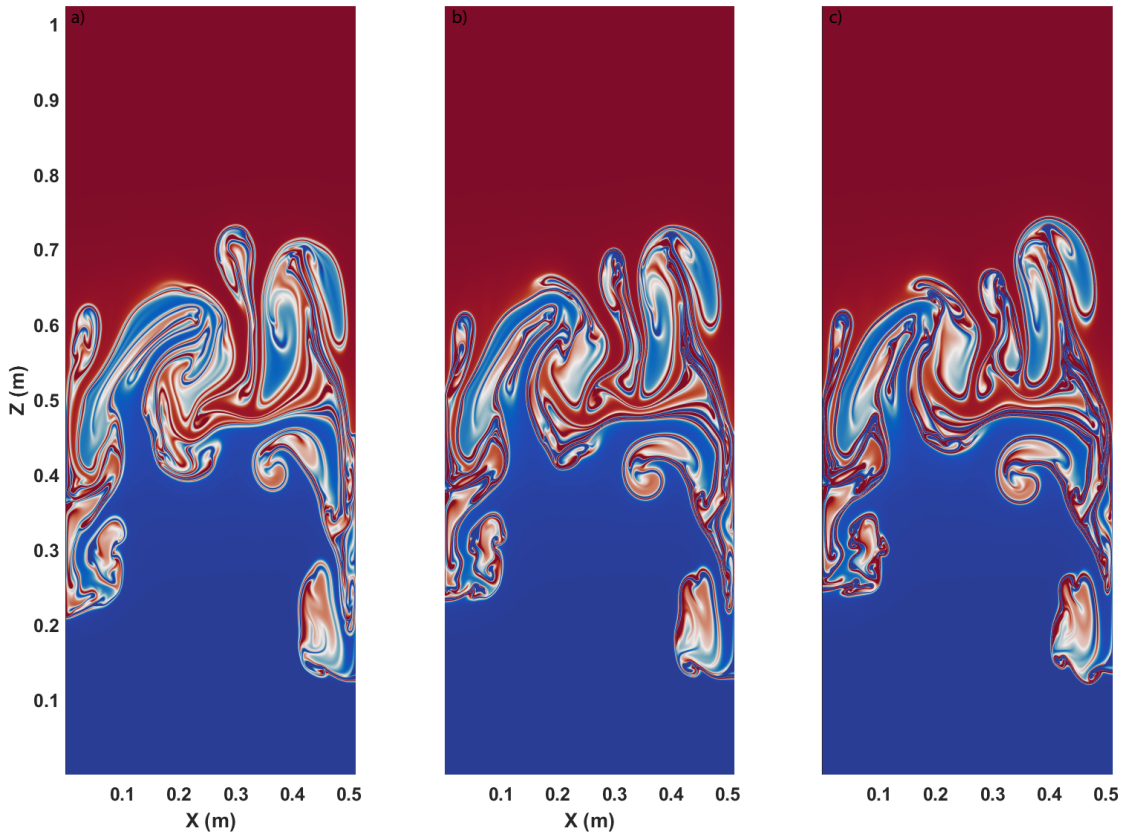

Figure 4.6: A comparison of the density field at $t = 250$s across Schmidt number cases. (a) Sc20, (b) Sc40, (c) Sc100. The colour axis for each panel has been set to the initial variable range (3.6480 kg/m^3 to 3.6955 kg/m^3).

while there is only one for the Sc=20 case, due to the increased diffusivity.

In contrast to the horizontally integrated kinetic energy, the vertically integrated kinetic (Figure 4.8) energy exhibits very few differences. The saturation of the colour axis has been set to 0.02 J/m^2 to show the relative intensity between thew cases. Again the dominant difference is in the intensity of kinetic energy with the lower Schmidt number cases exhibiting a more intense peak in kinetic energy. There are also small differences in the horizontal distribution of kinetic energy especially at late times.

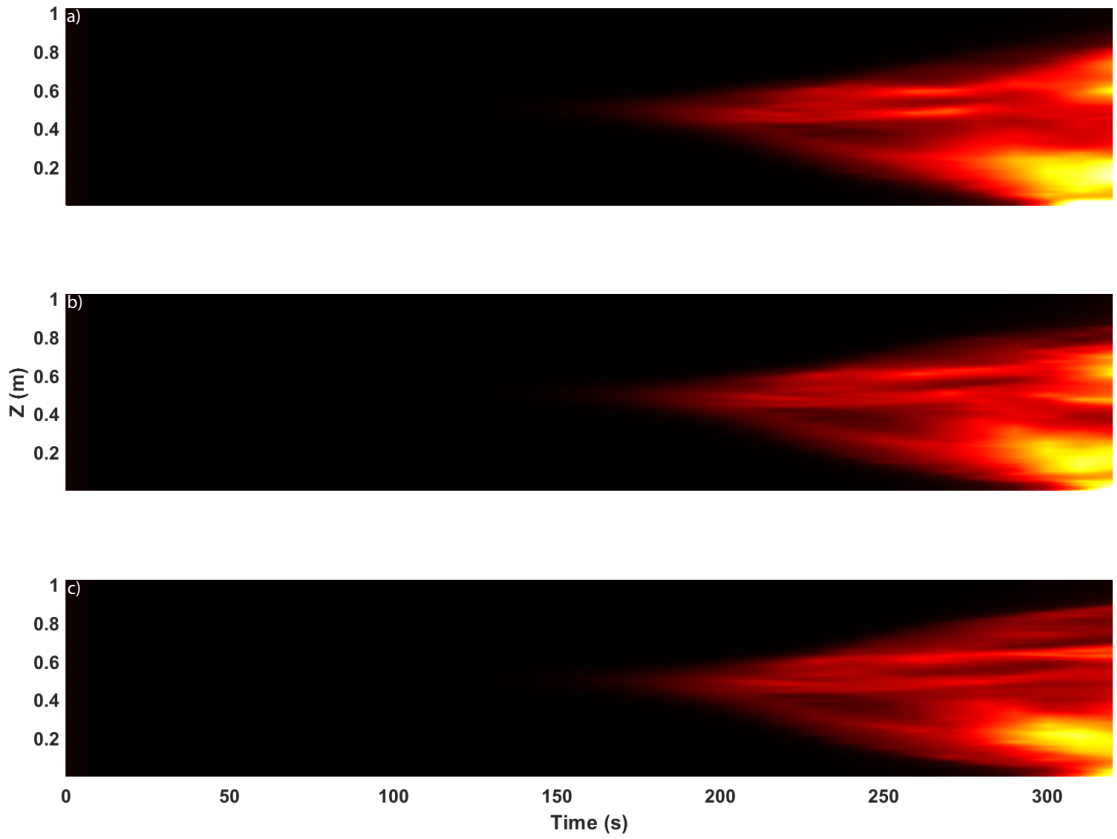

Figure 4.7: A space-time plot of the horizontally integrated kinetic energy across Schmidt number cases. (a) Sc20, (b) Sc40, (c) Sc100.

Differences between the cases become more apparent in the integrated energy components. The available potential energy (APE) was calculated following the procedures from Winters et al. (1995), from this the background potential energy (BPE) is readily calculated, similarly with the total potential energy (PE). The slight differences in kinetic energy (Figures 4.8 and 4.7) can be more clearly seen in the fully integrated kinetic energy time-series (Figure 4.9(d)). It is readily apparent that for late times, the Sc=100 case contains less kinetic energy than the other two. The Sc=833 case was stopped earlier than the other cases due to numerical instabilities due to under-resolution. While the Sc20 and Sc40 cases only differ by 8% by late times, the Sc100 case differed by 24%. The differences

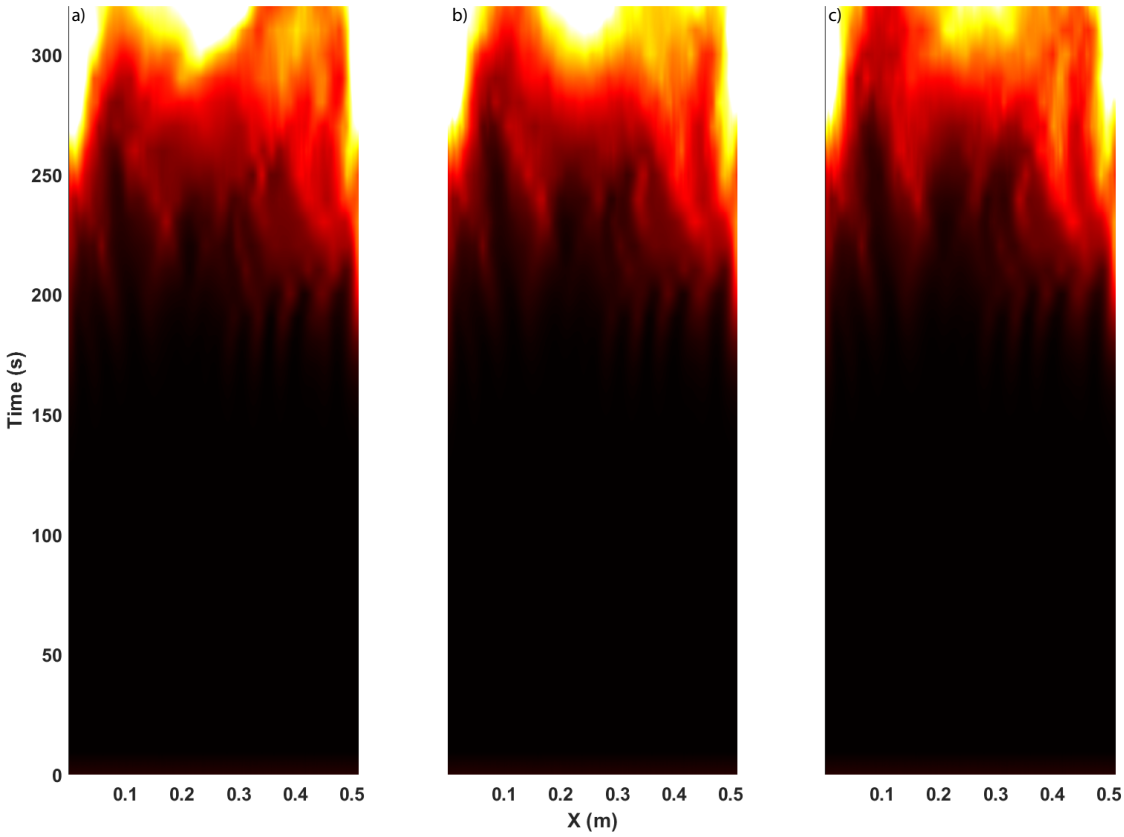

Figure 4.8: A space-time plot of the vertically integrated kinetic energy across Schmidt number cases. (a) Sc20, (b) Sc40, (c) Sc100.

between the cases are most visible in the APE and BPE. There is a substantial difference in both the value and the shape of the curves. As the Schmidt number is increased more energy is converted to APE and it takes longer to begin declining, with the Sc100 and Sc833 case never beginning to decline. This is also seen in the BPE where increasing the Schmidt number results in a much steeper slope.

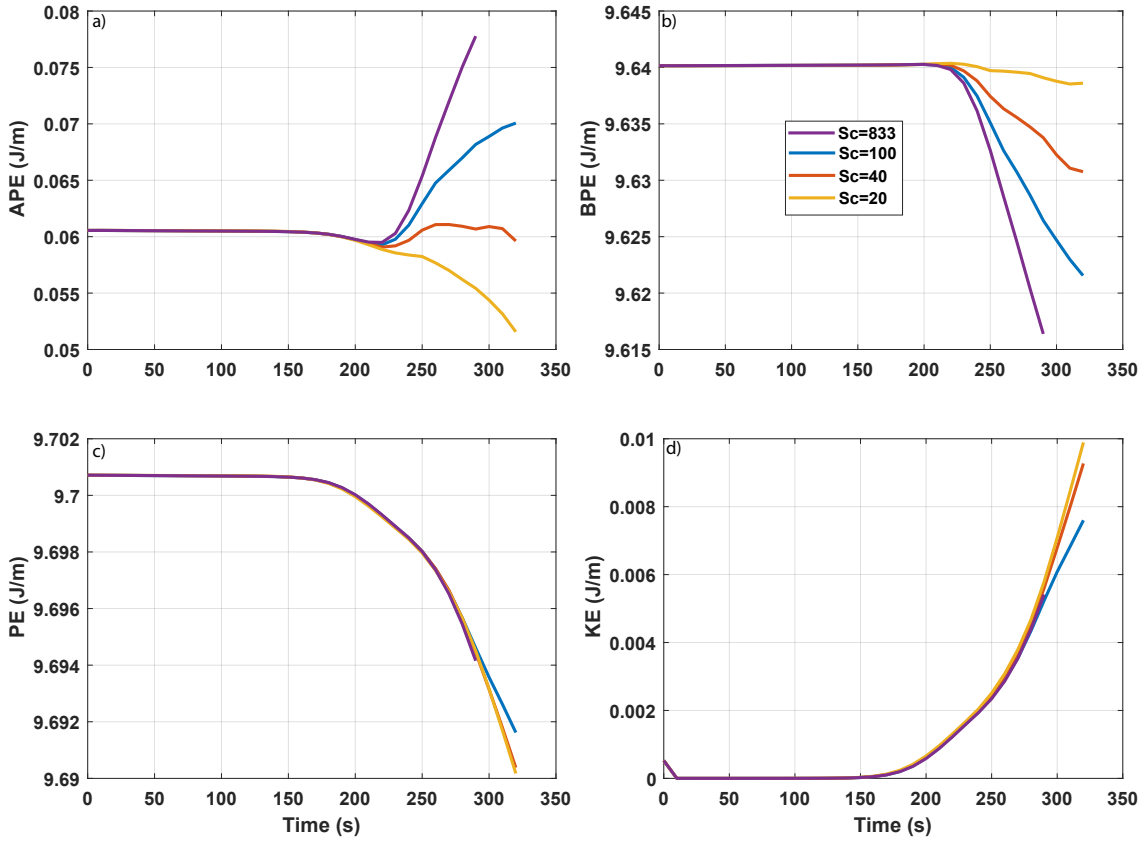

Figure 4.9: The integrated energy components for different Schmidt number cases. Panel (a) is the APE, panel (b) is the BPE, panel (c) is the PE, and panel (d) is the kinetic energy.

4.3.3 'Fudge' Variation

A common approach to stabilizing the numerical simulation is to introduce a "fudge" factor whereby the viscosity and the diffusivities are multiplied by a consistent factor. These increased values result in a more diffuse simulation that while less physical, is more numerically stable and maintains the same scaling for the non-dimensional parameter of interest, Sc.. Two cases were run with a 'fudge' factor, one at 2.5 (fudge2half) times normal and one (fudge5) at 5 times normal (see Table 4.1). Figure 4.10 are the integrated

energy component time-series for the two 'fudge' cases and the Sc100 case. Throughout all four energy components the primary effect of the 'fudge' factor is to increase the timescale of mixing. Each increase in 'fudge' factor delays the time before all fields begin changing, as well changing the rate of change. This is particularly evident in the APE (panel (a)).

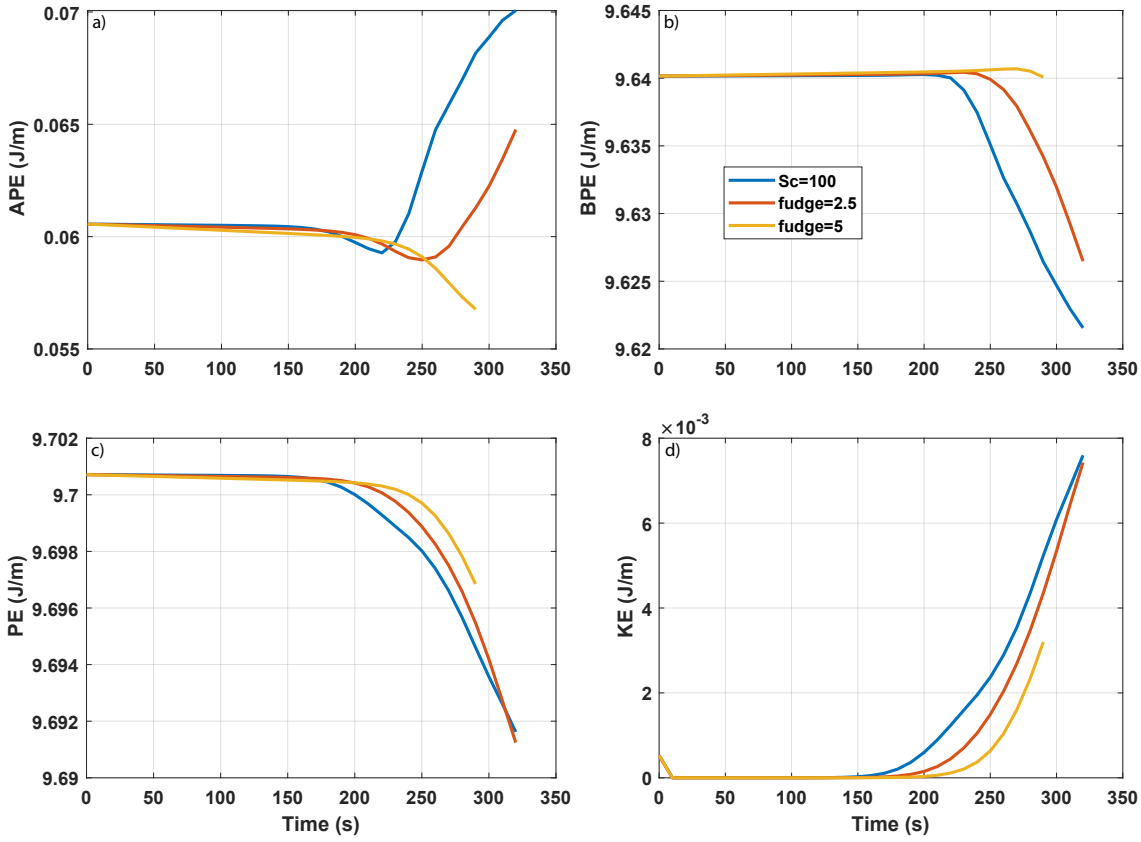

Figure 4.10: The integrated energy components for different fudge cases. Panel (a) is the APE, panel (b) is the BPE, panel (c) is the PE, and panel (d) is the kinetic energy.

4.3.4 Density Beyond Initial Range

Comparisons of the final sorted density field also provide interesting comparisons between the cases (Figure 4.11). Compared to the original profile (black dashed line) the most

glaring feature is the creation of over-shoot regions near the top and bottom of the domain that are beyond the original profile. These are the result of double diffusive effects creating densities beyond the initial range. The densities beyond the initial range appear to be grouped in pairs with the Sc100 and Sc833 cases paired, the fudge2half and Sc40 cases paired and the Sc20 and fudge5 cases paired. In the central density range, the Sc20 cases diffused the interface the most, while the Sc833 made the interface thinner.

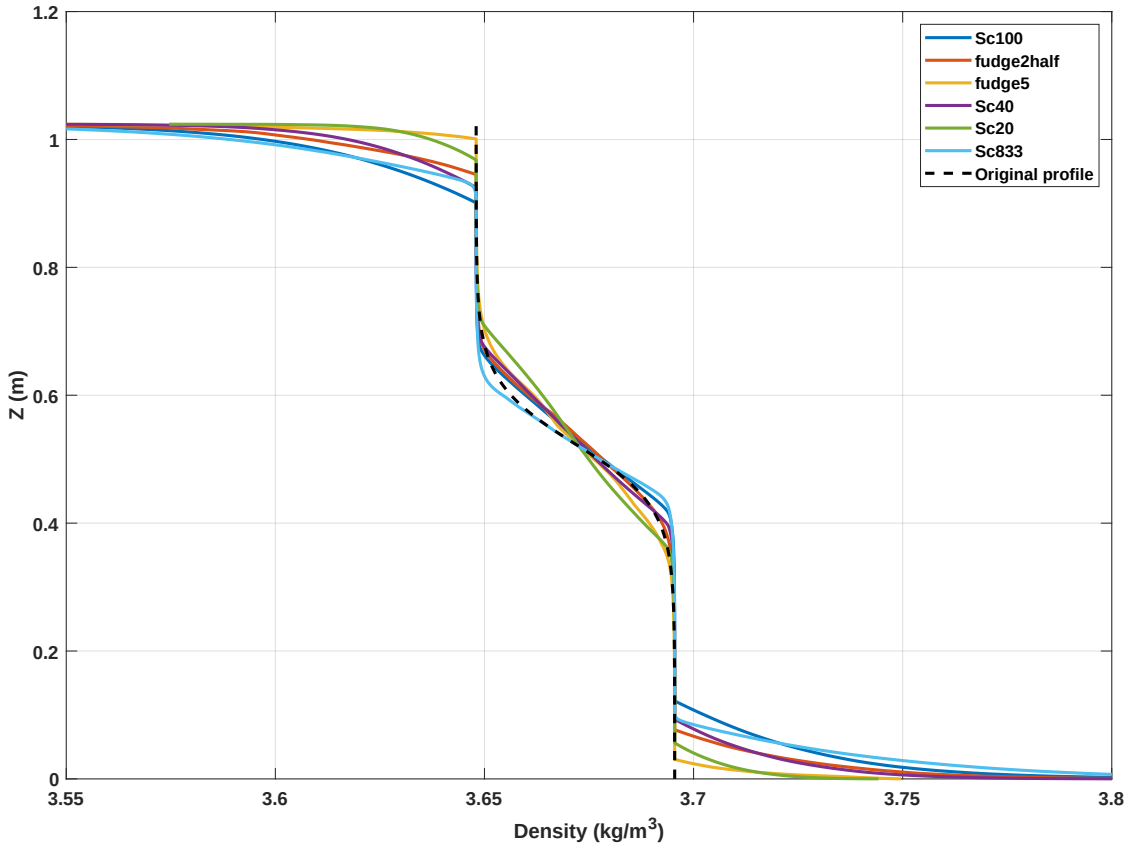

Figure 4.11: The final time sorted density profiles for all the cases compared to the original profile. The key feature is the creation of densities beyond the initial range through double diffusive effects. Note the $Sc = 833$ is separated from the other Sc variations since this case has numerical issues.

Figure 4.12 quantifies the the areas of density beyond the initial range for six cases.

Panel (a) is the total percentage of the domain beyond the initial density range, while (b) is the density above the initial range and (c) is the density below the initial range. The Sc100 and Sc833 cases are clearly superior at creating excess density with a more than 5% increase in percentage of domain compared to the next comparable cases (Sc=20 and f2.5). As the Schmidt number decreases and the 'fudge' factor increases, less of the excess density is created, less than half the amount of the previous cases (Sc20 compared with sc100). Comparisons of the positive and negative excess density reveal that there is a preference for the production of negative densities, approximately 3% more.

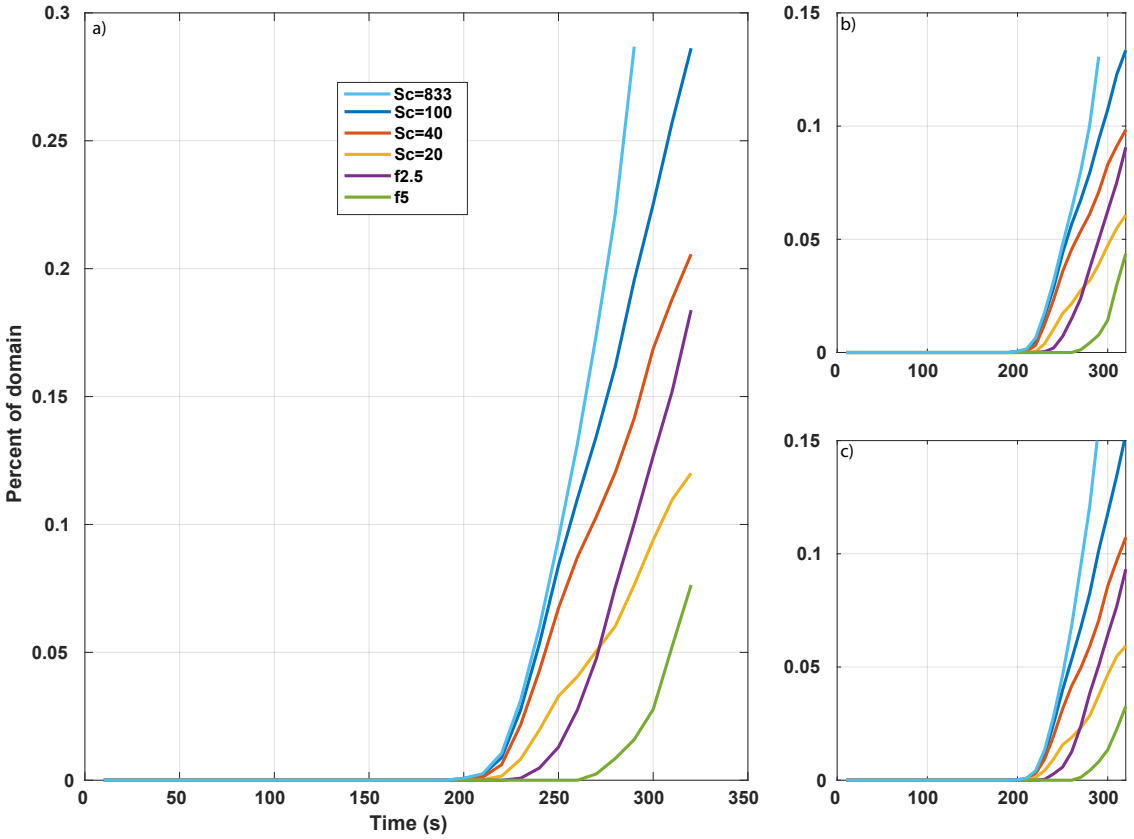

Figure 4.12: Time-series of percentage of domain with density beyond the initial range. (a) total percentage beyond initial range. (b) density above the initial range. (c) density below the initial range.

4.3.5 Reduction in Initial Temperature Difference

To test the sensitivity of our results to changes in the field situation, we computed two cases that maintain the same initial salinity stratification but reduce the temperature difference. This means we are reducing the density change. The initial temperature difference was reduced by 5% and 10%, (cases T95p and T90p respectively) since this proved enough to yield a qualitative change in dynamics. The evolution of these simulations is presented in Figure 4.13 and Figure 4.14. In contrast to the previous cases, the time between each panel was increased to 150 seconds (Figure 4.13) and 200 seconds (Figure 4.14). The T95p case appears to closely align with the dynamics of the previous cases, instabilities begin to grow at the pycnocline which develop into larger fingers which trap extreme densities along the interface, these then fully break down into turbulence. The T90p case begins similarly to the others but rather than develop large fingers which then create high gradient regions along their edges, small instabilities appear to pull apart the pycnocline which eventually begin trapping larger density variations and creating a high gradient region which protrudes downward. Both the shape of the instability and its development are different than all the other cases considered.

These qualitative differences and similarities between the reduced temperature cases and the other cases has a manifestation in the total energy, as shown in Figures 4.15 and 4.16. The T95p case appears to follow the same general pattern as the Sc=100 case, but with change over a longer time scale and over a larger magnitude. There are small differences in the precise shape of the T95p curves but in general it is very similar to the Sc=100 case. The T90p cases follows the same pattern of increase in energy when mixing begins to occur, but the rate and the amount of increase is reduced severely. Despite only a reduction of 10% in initial temperature range, the kinetic energies decreased by 95%. The relative increase in APE appears to be of the same magnitude as previous cases.

Similarly Figure 4.16 shows that the T95p case is nearly identical to the Sc=100 case in the amount of excess density that was created, the primary difference being when the production occurs. Another small difference is that the fraction of density below the initial range appears to level off at 3% in contrast to density above the initial range which reaches around 5% at the same time. This asymmetry is mirrored by the T90p case which does not produce any density below the initial range. Already by the end of the simulation time the T90p case had more excess density than the Sc=20 case and indeed excess density would continue to be produced if the simulation was continued.

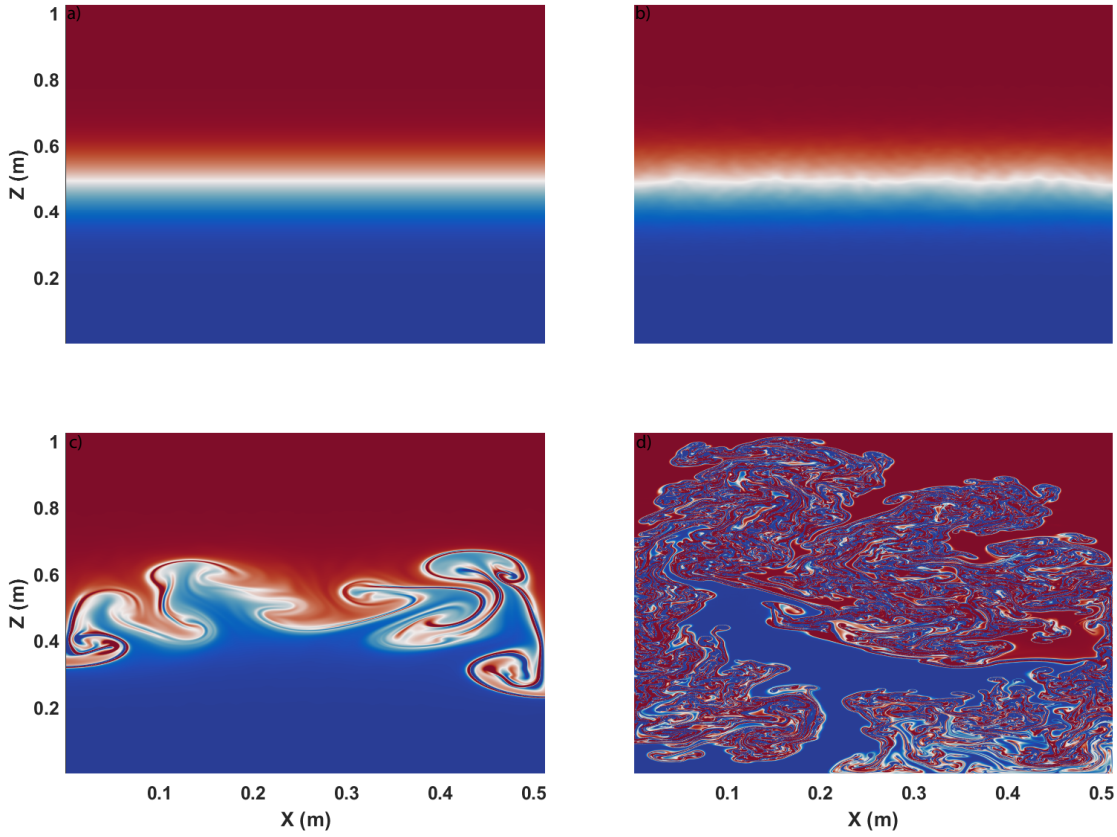

Figure 4.13: The density evolution for the T95p simulation. The colour range has been set to between (3.6696 kg/m^3 and 3.6955 kg/m^3). (a) $t = 0$s, (b) $t = 150$s, (c) $t = 300$s and (d) $t = 450$s.

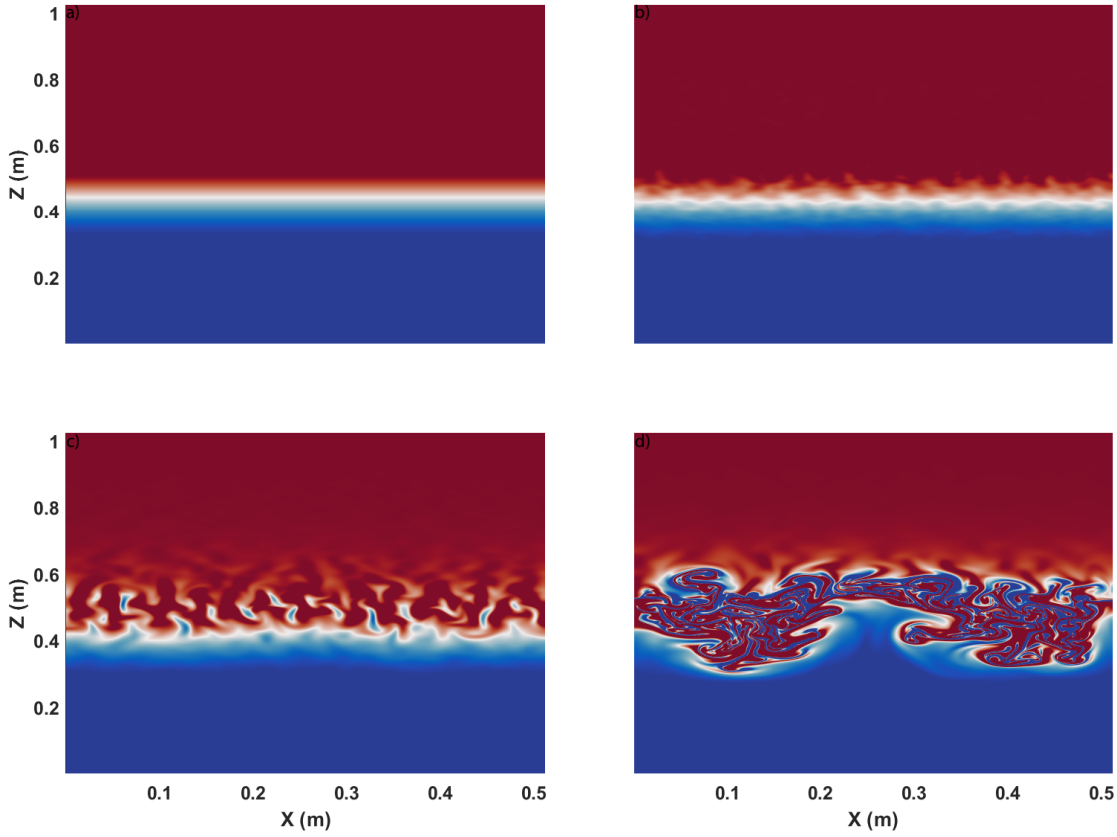

Figure 4.14: The density evolution for the T90p simulation. The colour range has been set to between (3.6915 kg/m^3 and 3.6955 kg/m^3). (a) $t = 0$s, (b) $t = 200$s, (c) $t = 400$s and (d) $t = 600$s.

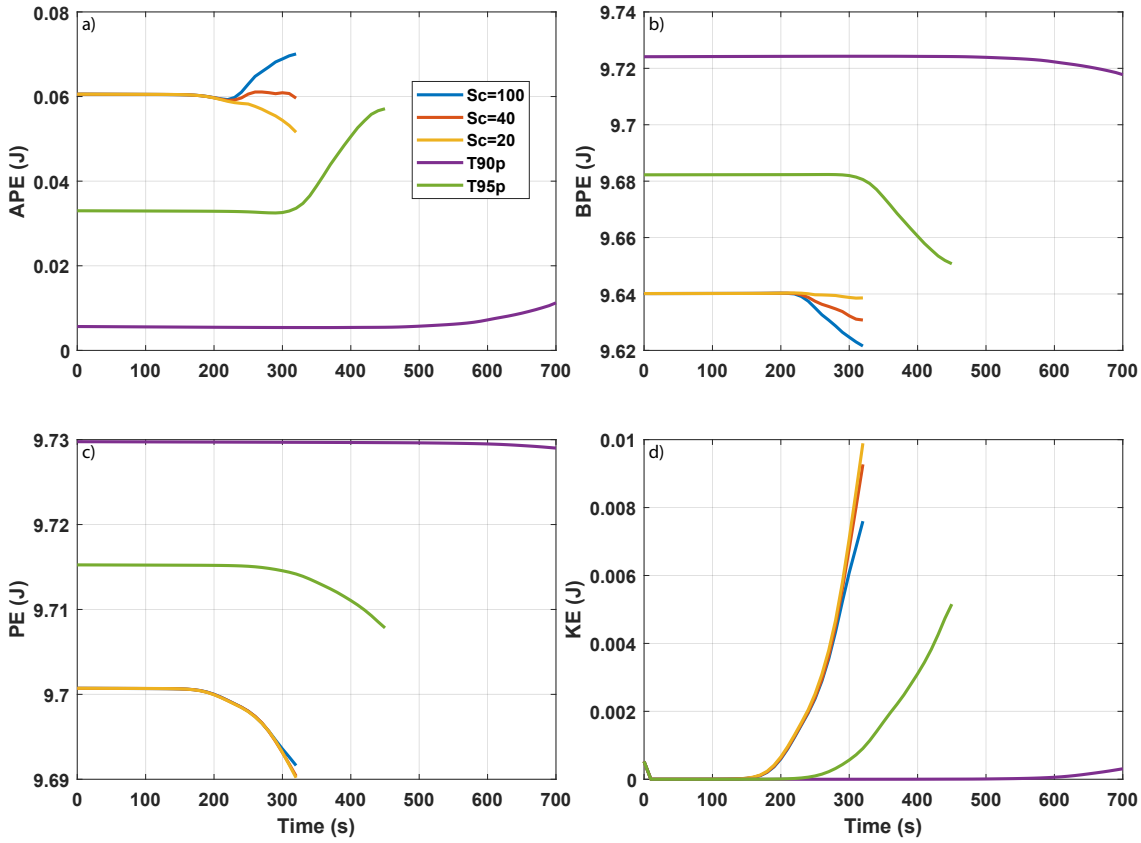

Figure 4.15: The integrated energy components for different Sc number cases and the reduced temperature difference cases. (a) APE, (b) BPE, (c) PE, and (d) KE.

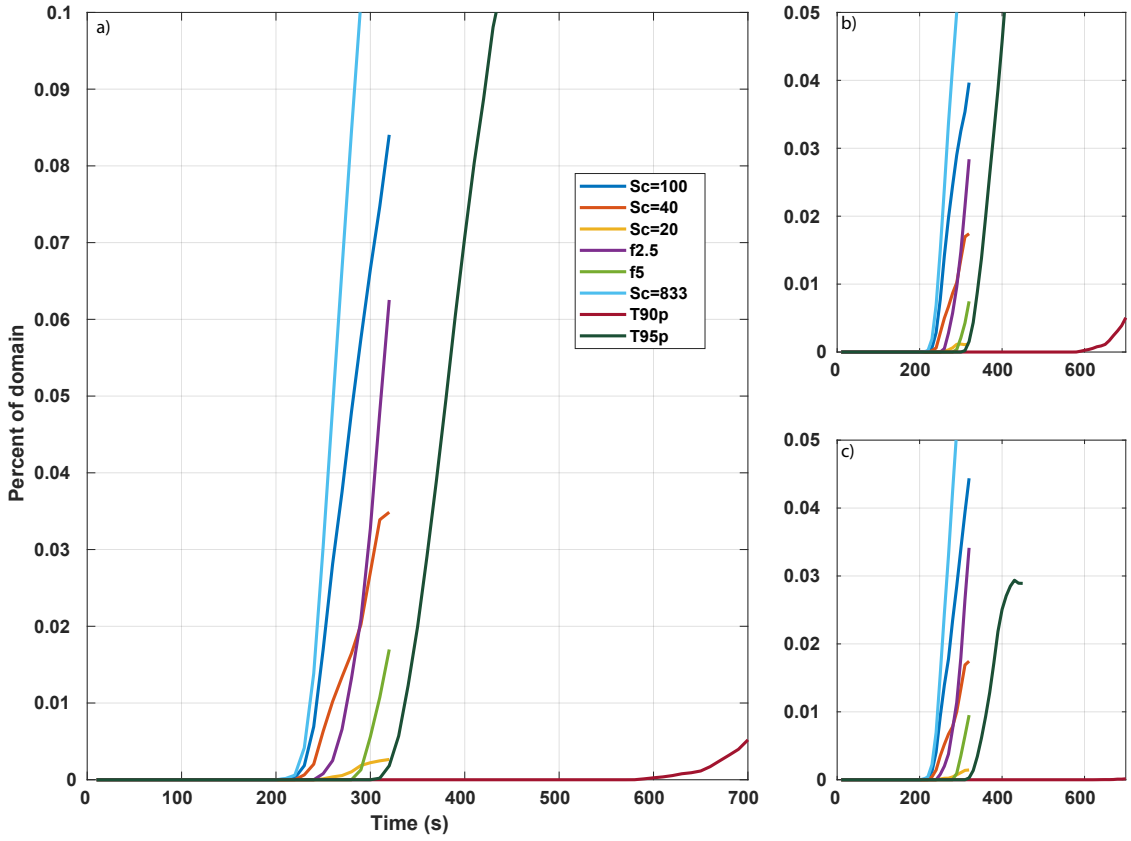

Figure 4.16: Time-series of percentage of domain with density beyond the initial range. (a) Total percentage beyond initial range. (b) Density above the initial range. (c) Density below the initial range. Note the $Sc = 833$ is separated from the other Sc variations since this case has numerical issues.

4.4 Discussion

It is clear from Figures 4.2 to 4.6 that there key differences between different Schmidt number cases. Increasing Sc results in much sharper density gradients as well as increasing the dynamic timescale. These effects are a result of the increased difference between the diffusivities of salt and heat. Furthermore while the high Sc cases are more 'physical' it is possible to observe numerical issues (e.g. excessive filtering) within the simulation once the field becomes turbulent. These lead to uncertainty in calculations at late times, however the general trends appear to be consistent. The effect of changing the Sc number is most visible in the integrated energy plots (Figure 4.9), increasing the Sc number significantly changes the shape of APE and BPE. In the Sc100, Sc40, and Sc20 cases APE evolution maintains a similar shape with the primary difference being the direction of APE growth during the mixing event (the Sc20 case actually only decreases in APE). In contrast the Sc833 case appears to grow linearly and does not decrease. It is possible that the growth in this case will eventually level off and even decrease in the same fashion as the other cases, but the time for this to occur is significantly longer than what was run and would likely run into numerical issues (issues were already arising in this case at the final time). A long time simulation at Sc=200 or Sc=400 would be possible however it would take a very long time to compute. The changes in BPE are a consequence of these changes in APE with the Sc833 case quickly removing energy from the background state while the Sc20 case hardly changes. In addition to differences in integrated energy components, differences are present in the spatial distribution of the KE. Both Figures 4.8 and 4.7 show slightly spatial differences in the intensity of the kinetic energy. However as the integrated kinetic energies (Figure 4.9) indicate, there is very little bulk difference between the cases, with slight differences only appearing after 290 s.

Changes in 'fudge' factor change the time-scale and magnitude of the changes in the different energy components. It appears that increasing the factor increases the time before energy begins to change significantly. The Sc=100 case dips in APE (Figure 4.10(a)) at 220 seconds, the f2.5 case dips at 250 seconds and the f5 case had not reached the dip before the simulation ended. By extrapolating we could hypothesize that this simulation would reach the dip at roughly 320 seconds.

The unique aspect of the double diffusive systems is the creation of densities beyond the initial range (what we refer to as "extended densities"). For example, in a heat-salt system, if enough heat is transferred from the hot, salty layer to the cool, fresh layer, the increase in heat to the cold layer along the interface can be enough to decrease its density below the initial density of the hot, salty layer. Similarly, this loss of heat can increase the density in the salty layer above the initial density of the fresh layer. The creation of

these extended densities can be clearly seen in Figure 4.11. The two most physically correct simulations (Sc=833 and Sc=100) are the most efficient at creating these extended densities while the least physical (Sc=20 and 5f) cases create the least; this is more clearly visible in Figure 4.12. Schmidt number variation appears to decrease the rate of excess density creation with lower Schmidt number cases having a lower slope. Figure 4.12 indicates that increasing 'fudge' factor also decreases the amount of excess density created, though it does not appear to change the rate of creation in contrast to Schmidt number variation. All these cases create both negative and positive density excesses with a slight preference for negative excesses

Decreasing the initial temperature difference by only 10% appears to dramatically change the dynamics of the mixing event. This is visible in Figure 4.14 and Figure 4.15. Small changes appear when temperature is reduced by 5%, primarily in the fraction of density below the initial range, but dynamically responds the same. This is in contrast with the T90p simulation which appears to be in a different dynamic regime as many of features from the other cases do not appear in this case (e.g. different time-scales, different type of instability, no negative density excess, etc...). This is particularly interesting given the increased likely-hood of a smaller density inversion occurring. We also note that the smaller density difference stays stable more than twice as long as the other cases.

4.5 Conclusions

To help elucidate the dynamics of known mixing events within the case systems of the Yucatan peninsula a series of numerical simulations were carried out using observed salinity and temperature profiles (i.e. measured density inversions). While these simulations are limited to the central portion of the cave passage and do not take into account boundary effects, they provide insight into potential mixing dynamics of this severely understudied system. Furthermore, simulations fully accounting for the complex geometries of the cave systems at physical parameters are not currently computationally possible. Thus some approximations will always have to be made, and we have made clear what approximations we have made. Through varying Schmidt number and 'fudge' factor we quantified the effects of making approximations to increase computational speed and reduce storage requirements. We have calculated how these changes effect the different energy components, dynamics, and particularly the unique feature of double diffusive systems, the creation of densities beyond the initial range. As compromises that reduce the viscous of double diffusive instabilities are made in the fudge factor and Schmidt number simulations, less energy is put into mixing and thus less excess density is created. While some compromises need

to be made to make the problem computationally tractable, there are issues with too much of an approximation. Based on the results presented here, we would not suggest using a Sc¡40 or a "fudge" factor ¿ 2.5 as these cases were close enough to the more physical cases to follow the same dynamics but still increased computational efficiency.

We investigated the effect of reducing the density difference between the two layers by reducing the the initial temperature difference by 5% and 10%. We showed that the density difference can control the dynamics of the instability. The 90% case exhibited different flow structures than all the other cases, however this did not appear to fundamentally changes the shape of the energy components. Where differences were reflected was in the generation of density less than the initial range. As the initial density difference was reduced less of the lower density was generated. As smaller density differences can remain stable for longer it is more likely for these types of inversions to occur in the field. It should also be noted that in this regime the Sc value will play a vital role in controlling the dynamics, but this needs to be further investigated.

Based on the results of this study it appears that density inversions of the magnitude that were observed in the sensor data go unstable relatively quickly. Even in simulations with reduced density differences the fluid went unstable in under 10 minutes. However, we acknowledge that we are not accounting for the entire situation. It is well known that during, and following the rainfall-induced mixing events, the MeWM begins flowing out to the coast (Moore et al., 1992; Metcalfe et al., 2011). This current would generate a shear within the water column which could act to stabilize the instability. Future research in this area is needed.

This is the first study of its kind, looking at the dynamics of mixing and unstable mixing events within a cave-like parameter regime. There is very little research on the hydrodyanmics within these cave systems despite the prevalence in the region. We hope this study can serve as a starting block for a more in-depth analysis of this important and highly interesting system. Future research directions include: 3D simulations, shear flow, addition of tracers, and boundaries.

4.6 Commentary

This chapter was written with the intent of submitting it for publication. The purpose of this research was to simulate the kinds of mixing processes that might occur within the cave conduits using the correct dynamical equations. However we understand that a larger scale simulation using the Navier-Stokes equations would not be computationally

feasible. For this reason we focused on common numeric short cuts that are used to improve computability and compared how they change the dynamics. This research was not meant to reproduce what was observed in the sensor data, the data was merely used as motivation to study the fluid dynamics of the system. The cave conduits are an extremely complicated physical system made especially difficult by the presence of a halocline which necessitates the inclusion of a vertical dimension. Martínez-Salvador et al. (2019) used MODFLOW-CFP (Conduit Flow Processes) to estimate pollutant residence time in the vicinity of Merida, Mexico. According to the authors this is the first time that a groundwater model has been applied to the region. However the model only has a vertical resolution of 4 boxes with thicknesses of 10 m to 50 m, which is insufficient to resolve the dynamics we are concerned with. Furthermore, in their model they explicitly assume that the saline interface does not play an important role, which is what we are particularly concerned with. Both directions require further investigation. Another aspect that makes the conduit flow especially complicated are the effects of wall roughness. It is well known that karst conduits have particularly high relative roughness (ratio of roughness height to conduit diameter) with values above 0.25 (Jeannin, 2001; Atkinson, 1977; Giese et al., 2018). Worthington and Soley (2017) analyzed turbulent flow in a variety of karst aquifers and concluded that turbulent flow increases hydraulic head and therefore that it needs to be considered on catchment scales. This has been the contribution of MODFLOW-CFP (Shoemaker et al., 2005), which included turbulent flow within the conduits. However, as explained in Shoemaker et al. (2008), the way that the turbulence is implemented is as an adjustment of the laminar hydraulic conductivity $K_{turb} = F_{adj} K_{lam}$. While this may be useful for catchment scale modelling, this implementation does not allow for the dynamics within the conduit to be investigated. True modelling of the turbulent dynamics within the conduits is beyond current computing capabilities but work has been done on modelling the dynamics of rough river beds. Rameshwaran et al. (2011) performed numerical simulations of the Reynolds-averaged Navier-Stokes equations for different sized gravel grain sizes. The techniques used in the article provide a possible framework for implementing karst conduit parameters.

Chapter 5

Conclusions and Future Work

The work presented in this thesis has attempted to elucidate the hydrodynamics of the very important and complicated karst groundwater system of the Yucatan Peninsula, Mexico.

In my first paper (Chapter 3; published) we attempted to understand the dynamics of groundwater entering the aquifer through simplified modelling. Understanding that we cannot fully model all the details of such a complicated system, we focused on the primary question: namely what effect does the surrounding mangrove and peat have on how water enters the groundwater system, and whether this effect can explain features observed in the measured water level and temperature. Based on the results of the paper, during a large storm the mangrove coverage acts as an aquitard not allowing the rainwater to percolate through the limestone, this then leads to water pooling above the peat and warming due to solar radiation. The warmed water is then pulled into the local sinkholes as the water table returns to its pre-event level. If there is insufficient rainfall to fully saturate the mangrove peat and allow for solar heating, we do not observe this effect.

In my second paper (Chapter 4; under review) we reported on tidal observations throughout the Yucatan peninsula at far-inland locations. Null hypothesis testing was used to verify that these signals were significant. All sites exhibited some level of tidal fluctuations. As the locations are too small to generate their own tides, they must be connected to the MaWM which does exhibit tidal oscillations. While traditional theory would not expect tidal oscillations so far inland, we argue that the presence of such large fracture zones allows for these tidal oscillations to propagate over large distances inland.

In my final paper (Chapter 5; in preparation) we considered the fluid dynamics of a mixing event near the halocline within one of the coastal cave systems. Based on reasonable initial conditions, we heavily simplified the situation to allow for numerical computation

using the correct governing equations for regions away from the walls. Various parameters were varied to better understand the dynamics of this system and how common approximations made for the sake of computational efficiency effect the dynamics. We found that while there is some leeway with the numerical choice of Schmidt number and 'fudge' factor (constant factor increasing all diffusivities), making large changes to these values leads to growing differences in energy calculations which are particularly important for mixing. So while there is some room for making approximations to these values, to maintain field-relevant energetics a relatively realistic value is needed. Reductions in initial density difference (i.e. temperature profile) showed a significant dynamical difference compared to the base case. Particularly differences in how the instability manifests and its effects on the density beyond the initial range created were observed.

It is worth revisiting the list of areas that the three main Chapters of this thesis make contributions to (which we reproduce from the Introduction for the reader's convenience):

1. The representation of landscape variations in hydrological models.
2. Fundamental questions concerning the connectivity of the peninsula, and the assumption of the hydrological isolation of the inland waters used for paleoclimate reconstructions.
3. The ability of modern numerical models to represent mixing in the cave networks.

Of these three, the strongest contribution has been made to point two. As one of the reviewers of the manuscript based on the thesis Chapter points out, connectivity of the peninsula is expected for hydrogeologists, but perhaps less so for those interested in paleoclimate reconstructions. Moreover, a detailed measurement is different than a logically sensible hypothesis. This assertion can apply to point one as well. The box model developed in this work is not a landscape scale model, but it is a first quantitative step to confirm existing hypotheses in the literature. Point three is a somewhat more negative result, since the work presented in Chapter 4 showed rather clearly that the detailed representation of mixing within the cave networks is too expensive for modern computational resources. Nevertheless, as is common in computational fluid dynamics, the work presented is able to quantify some of the ways in which cutting corners in resolution manifests itself in simulations. Subsequent practitioners can thus make rational decisions on what to do based on their goals. As a thematic link between chapters, we have identified consistent gaps between the measurement of hydrological variables and the quantitative theories, especially 'first-principles' theories, available to describe them. This thesis has also demonstrated the

utility of wavelet analysis in hydrology, something that was also identified by a reviewer for the manuscript based on Chapter 3 as important to the hydrology community.

There are many avenues for future work as this is a very broad collection of projects. Follow-up work for all three papers could be considered along with new investigations into this under studied system. For the first paper, the next step lies in better understanding the mangrove interactions. In the field, we would place sensors within the mangrove to quantify the heating and water level within this layer. Another avenue for new research is more complete modeling of cenote systems, rather than considering the mangrove-cenote system, create a box model of the cenote with boxes for the MeWM and MaWM. This could allow for comparison with previously recorded sensor data. There is significant possibility for future work based on the second paper as there are many outstanding questions in regards to tidal propagation inland, while we feel confident in our observations, the actual dynamics of this process remain unknown. We proposed the fracture hypothesis as it appears logical, but this must be further investigated. There are also important implications from this study that must be considered, particularly in the paleo-archeology context. There is also a lot of room for future work based on the third paper, now that parameter ranges have been investigated, 3D simulations become the next logical step. Another avenue is to consider the effect of shear flows, this is known to occur within these systems and may act to stabilize the fluid. A more difficult, but none the less important, avenue of future work is considering the effect of conduit wall roughness on flow. A schematic of these possible influences is presented in Figure 5.1. The rough walls along with the increased flow rates will likely lead to turbulence and enhanced mixing, however as the walls are extremely heterogeneous and complicated this poses a large computational problem.

I hope that the work presented in this thesis can act as a building block to a better understanding of this important groundwater system. In researching this project it has become abundantly apparent that this system is severely under investigated. There are many basic hydrodynamic questions which have no answers, especially from within the vast cave conduits. Furthermore the dual porosity nature of the geology in this region makes many traditional models unfeasible, requiring either heavy modifications of existing models or the creation of new ones. My hope is that I have answered a few of these outstanding questions and have paved the way for more difficult questions to be investigated.

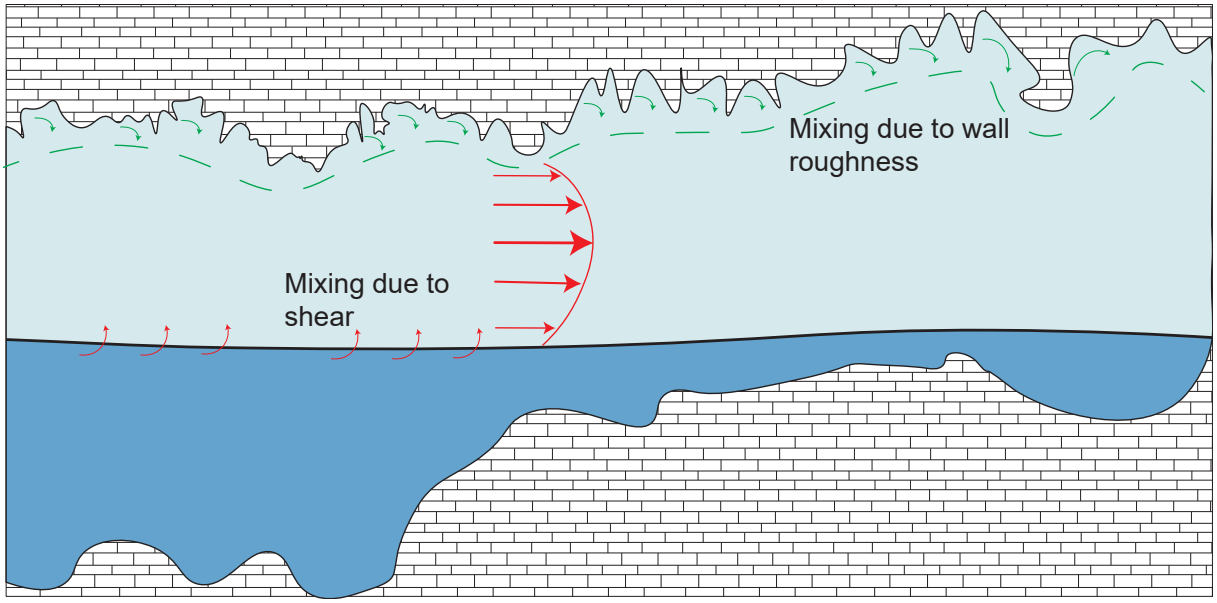

Figure 5.1: A diagram of possible dynamic effects within cave conduits for future studies to consider.

References

Atkinson, T. (1977). Diffuse Flow and Conduit Flow in Limestone Terrain in the Mendip Hills, Somerset (Great Britain). *Journal of Hydrology*, 35:93–110.

Back, W., Hanshaw, B. B., Pyle, T. E., Plummer, L. N., and Weidie, A. E. (1979). Geochemical significance of groundwater discharge and carbonate solution to the formation of Caleta Xel Ha, Quintana Roo, Mexico. *Water Resources Research*.

Bair, E. S. (2016). Applied Groundwater Modeling-Simulation of Flow and Advective Transport. *Groundwater*.

Bakalowicz, M. (2005). Karst groundwater: A challenge for new resources. *Hydrogeology Journal*, 13(1):148–160.

Bauer-Gottwein, P., Gondwe, B. R. N., Charvet, G., Marin, L. E., Rebolledo-Vieyra, M., and Merediz-Alonso, G. (2011). Review; The Yucatan Peninsula karst aquifer, Mexico. *Hydrogeology Journal*, 19(3):507–524.

Bayen, S. (2012). Occurrence, bioavailability and toxic effects of trace metals and organic contaminants in mangrove ecosystems: A review. *Environment International*, 48:84–101.

Beddows, P. A. (2004). *Groundwater Hydrology of a Coastal Conduit Carbonate Aquifer : Caribbean Coast of the Yucatán Peninsula , México*. PhD thesis, University of Bristol.

Beddows, P. A., Smart, P. L., Whitaker, F. F., and Smith, S. L. (2007). Decoupled fresh-saline groundwater circulation of a coastal carbonate aquifer: Spatial patterns of temperature and specific electrical conductivity. *Journal of Hydrology*, 346(1-2):18–32.

Berkowitz, B. (2002). Characterizing flow and transport in fractured geological media : A review. *Advances in Water Resources*, 25:861–884.

Boehrer, B., Dietz, S., Von Rohden, C., Kiwel, U., Jöhnk, K. D., Naujoks, S., Ilmberger, J., and Lessmann, D. (2009). Double-diffusive deep water circulation in an iron-meromictic lake. *Geochemistry, Geophysics, Geosystems*, 10(6).

Brankovits, D., Pohlman, J. W., Ganju, N. K., Iliffe, T. M., Lowell, N., Roth, E., Sylva, S. P., Emmert, J. A., and Lapham, L. L. (2018). Hydrologic Controls of Methane Dynamics in Karst Subterranean Estuaries. *Global Biogeochemical Cycles*, pages 1759–1775.

Brenner, M., Rosenmeier, M. F., Hodell, D. A., and Curtis, J. H. (2002). Paleolimnology of the Maya Lowlands: Long-term perspectives on interactions among climate, environment, and humans. *Ancient Mesoamerica*.

Brutsaert, W. (2008). *Hydrology: an introduction. 3rd ed.*

Brydon, D., Sun, S., and Bleck, R. (1999). A new approximation of the equation of state for seawater, suitable for numerical ocean models. *Journal of Geophysical Research*, 104(1):1537–1540.

Budyko, M. I. (1969). The effect of solar radiation variations on the climate of the Earth. *Tellus*, 21(5):611–619.

Byers, H. R., Moses, H., and Harney, P. J. (1949). Measurement of Rain Temperature. *Journal of Meteorology*, 6(1):51–55.

Carpenter, J. R., Sommer, T., and Wüest, A. (2012). Simulations of a double-diffusive interface in the diffusive convection regime. *Journal of Fluid Mechanics*, 711:411–436.

Charvet, G. (2009). *Exploration, modeling and management of groundwater resources in northern Quintana Roo, Mexico.* PhD thesis, Technical University of Denmark.

Chavez, M. and Cazelles, B. (2019). Detecting dynamic spatial correlation patterns with generalized wavelet coherence and non-stationary surrogate data. *Scientific Reports*, 9(1):1–9.

Clark, M. W., McConchie, D., Lewis, D. W., and Saenger, P. (1998). Redox stratification and heavy metal partitioning in Avicennia-dominated mangrove sediments: a geochemical model. *Chemical Geology*, 149(3-4):147–171.

Collins, S. V., Reinhardt, E. G., Werner, C. L., Le Maillot, C., Devos, F., and Meacham, S. S. (2015). Regional response of the coastal aquifer to Hurricane Ingrid and sedimentation flux in the Yax Chen cave system (Ox Bel Ha) Yucatan, Mexico. *Palaeogeography, Palaeoclimatology, Palaeoecology*, 438:226–238.

Cooper, H., Kohout, F., Henry, H., and Glover, R. (1964). *Sea water in coastal aquifers*. US Government Printing Office.

Coutino, A. (2016). *Halocline mixing due to heavy rainfall in the cenote's of the Yucatan Peninsula.* PhD thesis.

Coutino, A., Stastna, M., Kovacs, S., and Reinhardt, E. (2017). Hurricanes Ingrid and Manuel (2013) and their impact on the salinity of the Meteoric Water Mass, Quintana Roo, Mexico. *Journal of Hydrology*, 551:715–729.

Curtis, J. H., Hodelle, D. A., and Brenner, M. (1996). Climate Variability on the Yucatan Peninsula (Mexico) during the Past 3500 Years , and Implications for Maya Cultural Evolution. *Quaternary Research*, 47(1):37–47.

Deepwell, D. (2018). *High resolution simulations of mode-2 internal waves : transport , shoaling , and the influence of rotation by*. PhD thesis, University of Waterloo.

Defew, L. H., Mair, J. M., and Guzman, H. M. (2005). An assessment of metal contamination in mangrove sediments and leaves from Punta Mala Bay, Pacific Panama. *Marine Pollution Bulletin*, 50(5):547–552.

Douglas, P., Brenner, M., and Curtis, J. (2016). Methods and future directions for paleoclimatology in the Maya Lowlands. *Global and Planetary Change*.

Douglas, P., Pagani, M., Canuto, M., Brenner, M., Hodell, D., Eglinton, T., and Curtis, J. (2015). Drought, agricultural adaptation, and sociopolitical collapse in the Maya Lowlands. *Proceedings of the National Academy of Sciences*, 112(18):5607–5612.

Emblanch, C., Zuppi, G. M., Mudry, J., Blavoux, B., and Batiot, C. (2003). Carbon 13 of TDIC to quantify the role of the unsaturated zone: The example of the Vaucluse karst systems (Southeastern France). *Journal of Hydrology*, 279(1):262–274.

Farthing, M. W. and Ogden, F. L. (2017). Numerical Solution of Richards' Equation: A Review of Advances and Challenges. *Soil Science Society of America Journal*.

Ferris, J. G. (1951). Cyclic fluctuations of water level as a basis for determining aquifer transmissibility. In *International Union of Geodesy and Geophysiscs*.

Fetter, C. (2001). *Applied Hydrogeology*.

Fine, R. A. and Millero, F. J. (1973). Compressibility of water as a function of temperature and pressure. *The Journal of Chemical Physics*, 59(10):5529–5536.

Fofonoff, N. P. and Millard Jr., R. C. (1983). Algorithms for the computation of fundamental properties of seawater. Technical report, UNESCO, Paris.

Ford, D. and Williams, P. (2013). *Karst Hydrogeology and Geomorphology*.

Gabor, D. (1946). Theory of communication. Part 1: The analysis of information. *Electrical Engineers-Part III: Radio and ...*, 93(26):429–441.

Gallegos, J. J., Hu, B. X., and Davis, H. (2013). Simulating flow in karst aquifers at laboratory and sub-regional scales using MODFLOW-CFP. *Hydrogeology Journal*.

Garcia-Flores, F., Pérez-Cirera, V., World Wildlife Fund, Martin, P., Alanis, G., Centro Mexicano de Derecho Ambiental, and Guadarrama, L. (2008). Tourism, Trade and the Environment: Tourism and Coastal Development in the Mexican Portion of the Mesoamerican Reef. In *Fourth North American Symposium on Assessing the Environmental Effects of Trade Research Paper*, volume 8, pages 1–19.

Giannini, A., Cane, M. A., and Kushnir, Y. (2001). Interdecadal changes in the ENSO Teleconnection to the Caribbean Region and the North Atlantic Oscillation. *Journal of Climate*, 14(13):2867–2879.

Giannini, a., Kushnir, Y., and Cane, M. a. (2000). Interannual variability of the Carribbean rainfall, ENSO, and the Atlantic Ocean. *J. Climate*, 13:297–311.

Giese, M., Reimann, T., Bailly-Comte, V., Maréchal, J. C., Sauter, M., and Geyer, T. (2018). Turbulent and Laminar Flow in Karst Conduits Under Unsteady Flow Conditions: Interpretation of Pumping Tests by Discrete Conduit-Continuum Modeling. *Water Resources Research*, 54(3):1918–1933.

Gill, A. E. (1976). Adjustment under gravity in a rotating channel. *Journal of Fluid Mechanics*, 77(03):603–621.

Gilman, D. L., Fuglister, F. J., and Mitchell, J. M. (1963). On the Power Spectrum of "Red Noise". *Journal of the Atmospheric Sciences*.

Gondwe, B. R., Lerer, S., Stisen, S., Marín, L., Rebolledo-Vieyra, M., Merediz-Alonso, G., and Bauer-Gottwein, P. (2010). Hydrogeology of the south-eastern Yucatan Peninsula: New insights from water level measurements, geochemistry, geophysics and remote sensing. *Journal of Hydrology*, 389(1-2):1–17.

González-Herrera, R., Sánchez-y Pinto, I., and Gamboa-Vargas, J. (2002). Groundwater-flow modeling in the Yucatan karstic aquifer, Mexico. *Hydrogeology Journal*, 10(5):539–552.

Grace, A., Stastna, M., and Poulin, F. J. (2019). Numerical simulations of the shear instability and subsequent degeneration of basin scale internal standing waves. *Physical Review Fluids*, 4(1):14802.

Gregg, M. C., Asaro, E. A. D., Riley, J. J., and Kunze, E. (2018). Mixing Efficiency in the Ocean. *Annual Review of Marine Science*, 10:443–73.

Grinsted, A., Moore, J. C., and Jevrejeva, S. (2004). Application of the cross wavelet transform and wavelet coherence to geophysical time series. *Nonlinear Processes in Geophysics*, 11(5/6):561–566.

Grossmann, A. and Morlet, J. (1984). Decomposition of Hardy functions into square integrable wavelets of constant shape. *SIAM Journal on Mathematical Analysis*, 15(4):723–736.

Guenther, R. and Lee, J. (1988). *Partial differential equations of mathematical physics and integral equations*. Courier Corporation.

Gutiérrez, F., Parise, M., De Waele, J., and Jourde, H. (2014). A review on natural and human-induced geohazards and impacts in karst. *Earth-Science Reviews*, 138:61–88.

Haberman, R. (2004). *Applied partial differential equations: with Fourier series and boundary value problems*. Pearson, fourth edition.

Heath, R. C. (1983). BASIC GROUND-WATER HYDROLOGY. *US Geological Survey Water Supply Paper*.

Herrera-Silveira, J. A., Comin, F. A., Aranda-Cirerol, N., Troccoli, L., and Capurro, L. (2004). Coastal water quality assessment in the Yucatan Peninsula: Management implications. *Ocean and Coastal Management*, 47(11-12 SPEC. ISS):625–639.

Hodell, D. A. (2001). Solar Forcing of Drought Frequency in the Maya Lowlands. *Science*, 292(5520):1367–1370.

Hodell, D. A., Brenner, M., and Curtis, J. H. (2005a). Terminal Classic drought in the northern Maya lowlands inferred from multiple sediment cores in Lake Chichancanab (Mexico). *Quaternary Science Reviews*.

Hodell, D. A., Brenner, M., Curtis, J. H., Medina-González, R., Ildefonso-Chan Can, E., Albornaz-Pat, A., and Guilderson, T. P. (2005b). Climate change on the Yucatan Peninsula during the Little Ice Age. *Quaternary Research*.

Hodell, D. A., Curtis, J., H., and Brenner, M. (1995). Possible role of climate in the collapse of Classic Maya civilization. *Nature*, 375(6530):391–394.

Hubbert, M. (1940). The theory of ground-water motion. *The Journal of Geology*, pages 785–944.

Jacob, C. (1950). *Engineering Hydraulics. Flow of ground water*. John Wiley and Sons, New York.

Jeannin, P. Y. (2001). Modeling flow in phreatic and epiphreatic karst conduits in the Hölloch cave (Muotatal, Switzerland). *Water Resources Research*, 37(2):191–200.

Jiménez, J. (2004). Turbulent flows over rough walls. *Annual Review of Fluid Mechanics*.

Jones, G., Whitaker, F., Smart, P., and Sanford, W. (2000). Numerical modelling of geothermal and reflux circulation in Enewetak Atoll: implications for dolomitization. *Journal of Geochemical Exploration*, 69:71–75.

Kambesis, P. N. and Coke, J. G. (2013). Overview of the Controls on Eogenetic Cave and Karst Development in Quintana Roo, Mexico. *Coastal Karst Landforms*, 5(2002):347–373.

Kamotani, Y., Wang, L. W., Ostrach, S., and Jiang, H. D. (1985). Experimental study of natural convection in shallow enclosures with horizontal temperature and concentration gradients. *International Journal of Heat and Mass Transfer*.

Kathiresan, K. and Bingham, B. L. (2001). Biology of mangroves and mangroves ecosystems. *Advances in Marine Biology*, 40(01):81–251.

Kennett, D., Breitenbach, S., Aquino, V., Asmerom, Y., Awe, J., Baldini, J., Bartlein, P., Culleton, B., Ebert, C., Jazwa, C., Macri, M., Marwan, N., Polyak, V., Prufer, K., Ridley, H., Sodemann, H., Winterhalder, B., Haug, G., and et.al. (2012). Development and disintegration of Maya political systems in response to climate change. *Science*, 338(6108):788–91.

Kimura, S. and Smyth, W. (2007). Direct numerical simulation of salt sheets and turbulence in a double-diffusive shear layer. *Geophysical Research Letters*, 34(21):1–5.

Kovacs, S. E., Reinhardt, E. G., Werner, C., Kim, S. T., Devos, F., and Le Maillot, C. (2018). Seasonal trends in calcite-raft precipitation from cenotes Rainbow, Feno and Monkey Dust, Quintana Roo, Mexico: Implications for paleoenvironmental studies. *Palaeogeography, Palaeoclimatology, Palaeoecology*.

Kovacs, S. E. S., Reinhardt, E. G. E., Stastna, M., Coutino, A., Werner, C., Collins, S. V. S., Devos, F., Le, C., and Le Maillot, C. (2017). Hurricane Ingrid and Tropical Storm Hanna's effects on the salinity of the coastal aquifer , Quintana Roo , Mexico. *Journal of Hydrology*, 551:703–714.

Krywy-Janzen, A., Reinhardt, E., McNeill-Jewer, C., Coutino, A., Waltham, B., Stastna, M., Rissolo, D., Meacham, S., and van Hengstum, P. (2019). Water-level change recorded in Lake Pac Chen Quintana Roo, Mexico infers connection with the aquifer and response to Holocene sea-level rise and Classic Maya droughts. *Journal of Paleolimnology*, 62(4):373–388.

Kumar, P. and Foufoula-Georgiou, E. (1994). Wavelet analysis in geophysics: An introduction. In *Wavelets in geophysics*, chapter Wavelet An, pages 1–43. Academic Press.

Kundu, P. K., Cohen, I. M., and Dowling, D. R. (2011). *Fluid Mechanics*. Academic Press, fifth edition.

Lamb, K. and Nguyen, V. (2009). Calculating energy flux in internal solitary waves with an application to reflectance. *Journal of Physical Oceanography*, 39(3):559–580.

Lechleitner, F. A., Breitenbach, S. F., Rehfeld, K., Ridley, H. E., Asmerom, Y., Prufer, K. M., Marwan, N., Goswami, B., Kennett, D. J., Aquino, V. V., Polyak, V., Haug, G. H., Eglinton, T. I., and Baldini, J. U. (2017). Tropical rainfall over the last two millennia: Evidence for a low-latitude hydrologic seesaw. *Scientific Reports*.

Levanon, E., Yechieli, Y., Gvirtzman, H., and Shalev, E. (2017). Tide-induced fluctuations of salinity and groundwater level in unconfined aquifers – Field measurements and numerical model. *Journal of Hydrology*, 551:665–675.

Li, L., Barry, D. A., Cunningham, C., Stagnitti, F., and Parlange, J. Y. (2000). A two-dimensional analytical solution of groundwater responses to tidal loading in an estuary and ocean. *Advances in Water Resources*.

Li, L., Jeng, D. S., and Barry, D. A. (2002). Tidal fluctuations in a leaky confined aquifer: Localised effects of an overlying phreatic aquifer. *Journal of Hydrology*.

Linden, P. F. (1974). Salt fingers in a steady shear flow. *Geophysical Fluid Dynamics*.

List, F. and Radu, F. A. (2016). A study on iterative methods for solving Richards' equation. *Computational Geosciences*, 20(2):341–353.

Loper, D. and Chicken, E. (2008). Analysis and discussion of Karst conduit waves. *Geotechnical Special Publication*, 41003(183):454–466.

Loper, D. and Eltayeb, I. (2010). A linear model of conduit waves in karstic aquifers. *Geophysical and Astrophysical Fluid Dynamics*, 104(4):309–322.

Magaña, V., Amador, J. A., and Medina, S. (1999). The midsummer drought over Mexico and Central America. *Journal of Climate*, 12(6):1577–1588.

Magana, V. O., Vázquez, J. L., Párez, J. L., and Pérez, J. B. (2003). Impact of El Niño on precipitation in Mexico. *Geofisica Internacional*, 42(3):313–330.

Mallat, S. (1999). *A wavelet tour of signal processing*. Academic Press, London, second edition.

Marchand, C., Allenbach, M., and Lallier-Vergès, E. (2011). Relationships between heavy metals distribution and organic matter cycling in mangrove sediments (Conception Bay, New Caledonia). *Geoderma*, 160(3-4):444–456.

Marin, L. E. (1990). *Field investigations and numerical simulation of groundwater flow in the karstic aquifer of northwestern Yucatan, Mexico*. PhD thesis, Northern Illinois University.

Marín, L. E., Perry, E. C., Essaid, H. I., and Steinich, B. (2004). Hydrogeological investigations and numerical simulation of groundwater flow in the karstic aquifer of northwestern Yucatan, Mexico. In *Coastal aquifer management: monitoring, modeling and case studies*.

Martínez-Salvador, C., Moreno-Gómez, M., and Liedl, R. (2019). Estimating Pollutant Residence Time and NO 3 Concentrations in the Yucatan Karst Aquifer; Considerations for an Integrated Karst Aquifer Vulnerability Methodology. *Water*, 11(1431).

McDougall, T. J. and Taylor, J. R. (2009). Flux measurements across a finger interface at low values of the stability ratio. *Journal of Marine Research*.

McMillan, T. C., Rau, G. C., Timms, W. A., and Andersen, M. S. (2019). Utilizing the Impact of Earth and Atmospheric Tides on Groundwater Systems: A Review Reveals the Future Potential. *Reviews of Geophysics*, 57(2):281–315.

McNeill-Jewer, C. A., Reinhardt, E. G., Collins, S., Kovacs, S., Chan, W. M., Devos, F., and LeMaillot, C. (2019). Seasonal rainfall and its effect on nutrient input and biological productivity in the Yax Chen cave system (Ox Bel Ha), Quintana Roo, Mexico; implications for XRF core studies and paleohydrological reconstructions. *Palaeogeography, Palaeoclimatology, Palaeoecology*, 534(109289).

Medina-Elizalde, M., Burns, S. J., Lea, D. W., Asmerom, Y., von Gunten, L., Polyak, V., Vuille, M., and Karmalkar, A. (2010). High resolution stalagmite climate record from the Yucatan Peninsula spanning the Maya terminal classic period. *Earth and Planetary Science Letters*, 298(1-2):255–262.

Méndez, M. and Magaña, V. (2010). Regional aspects of prolonged meteorological droughts over Mexico and central America. *Journal of Climate*.

Mendoza-González, G., Martínez, M. L., Rojas-Soto, O. R., Vázquez, G., and Gallego-Fernández, J. B. (2013). Ecological niche modeling of coastal dune plants and future potential distribution in response to climate change and sea level rise. *Global Change Biology*.

Metcalfe, C. D., Beddows, P. A., Bouchot, G. G., Metcalfe, T. L., Li, H., and Van Lavieren, H. (2011). Contaminants in the coastal karst aquifer system along the Caribbean coast of the Yucatan Peninsula, Mexico. *Environmental Pollution*, 159(4):991–997.

Middleton, L. and Taylor, J. R. (2020). A general criterion for the release of background potential energy through double diffusion. *Journal of Fluid Mechanics*, pages 1–12.

Moore, Y. H., Stoessel, R., and Easley, D. (1992). Fresh water/sea-water relationship within a groundwater system, northeastern coast of the Yucatán Peninsula. *Ground Wat.*, 30(3):343–350.

Mutchler, T., Dunton, K. H., Townsend-Small, A., Fredriksen, S., and Rasser, M. K. (2007). Isotopic and elemental indicators of nutrient sources and status of coastal habitats in the Caribbean Sea, Yucatan Peninsula, Mexico. *Estuarine, Coastal and Shelf Science*, 74(3):449–457.

Novelo, M., Borges, C., Borges, V., Pérez, B., Peraza, C., and Vivas, R. G. (2009). Estimación del potencial contaminante de las granjas porcinas y avícolas del estado de Yucatán. *Ingeniería*, 13(2):13–21.

Olsthoorn, J., Baglaenko, A., and Stastna, M. (2013). Analysis of asymmetries in propagating mode-2 waves. *Nonlinear Processes in Geophysics*, 20(1):59–69.

Ozgökmen, T. M. and Esenkov, O. E. (1998). Asymmetric salt fingers induced by a nonlinear equation of state. *Physics of Fluids*.

Özgökmen, T. M., Esenkov, O. E., and Olson, D. B. (1998). A numerical study of layer formation due to fingers in double-diffusive convection in a vertically-bounded domain. *Journal of Marine Research*.

Pachepsky, Y. A., Timlin, D. J., and Rawls, W. J. (2003). Generalized Richards' equation to simulate water transport in unsaturated soils. *Journal of Hydrology*, 272(1-4):290.

Padilla, C., Gutierrez, D., Lara, M., and Garcia, C. (1993). Coral reefs of the Biosphere Reserve of Sian Ka'an, Quintana Roo, Mexico,. In *Proceedings of the 7th International Coral Reef Symposium*, volume 2, pages 986–992.

Pelas, H. R. (2011). *Tourism development in Cancun, Mexico: An analysis of state-directed tourism initiatives in a developing nation*. PhD thesis, Georgetown University.

Perry, E., Paytan, A., Pedersen, B., and Velazquez-Oliman, G. (2009). Groundwater geochemistry of the Yucatan Peninsula, Mexico: Constraints on stratigraphy and hydrogeology. *Journal of Hydrology*.

Perry, E., Velazquez-Oliman, G., and Marin, L. (2002). The hydrogeochemistry of the karst aquifer system of the northern yucatan peninsula, Mexico. *International Geology Review*, 44(3):191–221.

Perry, E., Velazquez-Oliman, G., and Socki, R. (2003). Hydrogeology of the Yucatán Peninsula. In *The Lowland Maya: Three Millennia at the Human–Wildland Interface*, pages 115–138.

Piacsek, S. A., Brummell, N. H., and McDonald, B. E. (1988). Numerical Experiments on Thermohaline Convective Motions Across Interfaces of Intrusions. *Elsevier Oceanography Series*.

Piacsek, S. A. and Toomre, J. (1980). Nonlinear evolution and structure of salt fingers. *Elsevier Oceanography Series*.

Pinsky, M. (2009). Introduction to Fourier analysis and wavelets.

Radko, T. (2003). A mechanism for layer formation in a double-diffusive fluid. *Journal of Fluid Mechanics*.

Rahmstorf, S. (1995). Bifurcations of the Atlantic thermohaline circulation in response to changes in the hydrological cycle. *Nature*, 378(6553):145.

Rameshwaran, P., Naden, P. S., and Lawless, M. (2011). Flow modelling in gravel-bed rivers: Rethinking the bottom boundary condition. *Earth Surface Processes and Landforms*, 36(10):1350–1366.

Rieutord, M. and Espinosa Lara, F. (2013). Studying Stellar Rotation and Convection. *Studying Stellar Rotation and Convection*.

Ruddick, B. R., Phillips, O. M., and Turner, J. S. (1999). A laboratory and quantitative model of finite-amplitude thermohaline intrusions. In *Dynamics of Atmospheres and Oceans*.

Šafanda, J., Heidinger, P., Wilhelm, H., and Čermák, V. (2005). Fluid convection observed from temperature logs in the karst formation of the Yucatán Peninsula, Mexico. *Journal of Geophysics and Engineering*, 2(4):326–331.

Sakai, K. and Peltier, W. R. (1997). Dansgaard-Oeschger oscillations in a coupled atmosphere-ocean climate model. *Journal of Climate*.

Sakai, K. and Peltier, W. R. (1999). A dynamical systems model of the Dansgaard-Oeschger oscillation and the origin of the bond cycle. *Journal of Climate*.

Sanford, W. and Konikow, L. (1989). Simulation of Calcite Dissolution and Porosity Changes in Saltwater Mixing Zones in Coastal Aquifers. *Water Resources Research*, 25(4):655–667.

Schmitt, R. W. (1994). Double diffusion in oceanography. *Annual Review of Fluid Mechanics*.

Schmitt, R. W., Perkins, H., Boyd, J. D., and Stalcup, M. C. (1987). C-SALT: An investigation of the thermohaline staircase in the western tropical North Atlantic. *Deep Sea Research Part A, Oceanographic Research Papers*.

Schmitter-Soto, J. J., Comín, F. A., Escobar-Briones, E., Herrera-Silveira, J., Alcocer, J., Suárez-Morales, E., Elías-Gutiérrez, M., Díaz-Arce, V., Marín, L. E., and Steinich, B. (2002). Hydrogeochemical and biological characteristics of cenotes in the Yucatan Peninsula (SE Mexico). *Hydrobiologia*, 467:215–228.

Schultz, G. and Ruppel, C. (2002). Constraints on hydraulic parameters and implications for groundwater flux across the upland-estuary interface. *Journal of Hydrology*.

Sebben, M. L., Werner, A. D., and Graf, T. (2015). Advances in Water Resources Seawater intrusion in fractured coastal aquifers : A preliminary numerical investigation using a fractured Henry problem. *Advances in Water Resources*, 85:93–108.

Series, M. E. (1991). Determining the Mean Hydraulic Gradient of Ground Water Affected by Tidal Fluctuations. *Groundwater*.

Shen, C. Y. (1997). Numerical simulation of two-dimensional salt fingers. *Journal of Geophysical Research C: Oceans*.

Shoemaker, W. B., Cunningham, K. J., Kuniansky, E. L., and Dixon, J. (2008). Effects of turbulence on hydraulic heads and parameter sensitivities in preferential groundwater flow layers. *Water Resources Research*, 44(3):1–11.

Shoemaker, W. B., Kuniansky, E. L., Birk, S., Bauer, S., and Swain, E. D. (2005). Documentation of a Conduit Flow Process (CFP) for MODFLOW-2005. Technical report.

Smart, P. L., Beddows, P. A., Coke, J., Doerr, S., and Whitaker, F. F. (2006). Cave Development on the Caribbean coast of the Yucatan Peninsula, Quintana Roo, Mexico. *Geological Society of America*, 2404(10):105–128.

Smart, P. L., Dawans, J. M., and Whitaker, F. (1988). Carbonate dissolution in a modern mixing zone. *Nature*.

Smith, A. J. (1999). Application of a tidal method for estimating aquifer diffusivity: Swan River, Western Australia. Technical report.

Sommer, T., Carpenter, J. R., and Wüest, A. (2014). Double-diffusive interfaces in Lake Kivu reproduced by direct numerical simulations. *Geophysical Research Letters*, 41(14):5114–5121.

Soontiens, N., Stastna, M., and Waite, M. L. (2015). Topographically generated internal waves and boundary layer instabilities. *Physics of Fluids*, 27(8).

Spiegel, E. A. and Veronis, G. (1960). On the Boussinesq Approximation for a Compressible Fluid. *The Astrophysical Journal*, 131:442.

Stastna, M. and Peltier, W. R. (2007). On box models of the North Atlantic thermohaline circulation: Intrinsic and extrinsic millennial timescale variability in response to deterministic and stochastic forcing. *Journal of Geophysical Research: Oceans*, 112(10):1–15.

Stein, E. M. and Shakarchi, R. (2011). *Fourier analysis: An introduction*.

Steinich, B. and Marín, L. E. (1996). Hydrogeological Investigations in Northwestern Yucatan, Mexico, Using Resistivity Surveys. *Ground Water*, 34(4):640–646.

Steinich, B. and Marín, L. E. (1997). Determination of flow characteristics in the aquifer of the Northwestern Peninsula of Yucatan, Mexico. *Journal of Hydrology*, 191(1-4):315–331.

Stern, M. E. (1960). The "Salt-Fountain" and Thermohaline Convection. *Tellus*.

Stoessell, R. K. (1995). Dampening of Transverse Dispersion in the Halocline in Karst Limestone in the Northeastern Yucatan Peninsula. *Ground Water*, 33(3):366–371.

Stoessell, R. K. and Coke, J. G. (2006). An Explanation for the Lack of a Dilute Freshwater Lens in Unconfined Tropical Coastal Aquifers : Yucatan Example. *Gulf Coast Association of Geological Societies Transactions*, 56:785–792.

Stoessell, R. K., Ward, W. C., Ford, B. H., and Schuffert, J. D. (1989). Water chemistry and CaCO 3 dissolution in the saline part of an open-flow mixing zone, coastal Yucatan Peninsula, Mexico. *Geological Society of America Bulletin*.

Stommel, H. (1961). Thermohaline Convection with Two Stable Regimes of Flow. *Tellus*, 13.

Stouffer, R. J. and et al. (2006). Investigating the Causes of the Response of the Thermohaline Circulation to Past and. *Journal of Climate*, 19:1365–1387.

Stranne, C., Mayer, L., Weber, T. C., Ruddick, B. R., Jerram, K., Weidner, E., Nilsson, J., and Gårdfeldt, K. (2017). Acoustic Mapping of Thermohaline Staircases in the Arctic Ocean. *Nature*, 7(15192):1–9.

Subich, C. J., Lamb, K. G., and Stastna, M. (2013). Simulation of the Navier-Stokes equations in three dimensions with a spectral collocation method. *International Journal for Numerical Methods in Fluids*, 73(2):103–129.

Sun, H. (1997). A two-dimensional analytical solution of groundwater response to tidal loading in an estuary. *Water Resources Research*.

Torrence, C. and Compo, G. P. (1998). A Practical Guide to Wavelet Analysis. *Bulletin of the American Meteorological Society*, 79(1):61–78.

Trefethen, L. N. (2000). *Spectral Methods in Matlab*, volume 10. Siam.

Trefry, M. G. and Bekele, E. (2004). Structural characterization of an island aquifer via tidal methods. *Water Resources Research*, 40:1–21.

Trefry, M. G. and Johnston, C. D. (1998). Pumping test analysis for a tidally forced aquifer. *Ground Water*.

Turner, J. S. (1965). The coupled turbulent transports of salt and and heat across a sharp density interface. *International Journal of Heat and Mass Transfer*.

Turner, J. S. (1967). Salt fingers across a density interface. *Deep-Sea Research and Oceanographic Abstracts*.

Turner, J. S. (1973). *Buoyancy effects in fluids*. Cambridge University Press.

Twilley, R. R. and Chen, R. (1998). A water budget and hydrology model of a basin mangrove forest in Rookery Bay, Florida Robert. *Marine and Freshwater Research*, 49(4):309.

Weidie, A. E. (1985). Part I: Geology of Yucatan Platform. In *Geology and hydrogeology of the Yucatan and Quaternary geology of northeastern Yucatan Peninsula.*, pages 1–19. New Orleans Geological Society.

Wells, M. G. and Griffiths, R. W. (2002). Localized stirring in a field of salt-fingers. *Dynamics of Atmospheres and Oceans*.

Wells, M. G. and Griffiths, R. W. (2003). Interaction of salt finger convection with intermittent turbulence. *Journal of Geophysical Research: Oceans*.

Werner, A. D., Bakker, M., Post, V. E. A., Vandenbohede, A., Lu, C., Ataie-ashtiani, B., Simmons, C. T., and Barry, D. A. (2013). Advances in Water Resources Seawater intrusion processes , investigation and management : Recent advances and future challenges. *Advances in Water Resources*, 51:3–26.

Werner, A. D. and Simmons, C. T. (2009). Impact of Sea-Level Rise on Sea Water Intrusion in Coastal Aquifers. *Ground Water*, 47(2):197–204.

Whitaker, F. and Smart, P. (1990). Active circulation of saline ground waters in carbonate platforms: Evidence from the Great Bahama Bank. *Geology*, 18(3):200–203.

Wilks, D. (2007). *Statistical Methods in the Atmospheric Sciences Second Edition*.

Williams, A. J. (1975). Images of ocean microstructure. *Deep-Sea Research and Oceanographic Abstracts*.

Wilson, A. (2005). Fresh and saline groundwater discharge to the ocean: a regional perspective. *Water Resources Research*, 41(2).

Winters, K. B., Lombard, P. N., Riley, J. J., and D'Asaro, E. A. (1995). Available potential energy and mixing in density-stratified fluids. *Journal of Fluid Mechanics*, 289(C5):115–128.

Worthington, S. R. and Soley, R. W. (2017). Identifying turbulent flow in carbonate aquifers. *Journal of Hydrology*, 552:70–80.

Worthington, S. R. H., Ford, D. C., and Beddows, P. A. (2001). Porosity and permeability enhancement in unconfined carbonate aquifers as a result of solution. In *Speleo Brazil 2001 - 13th International Congress of Speleology*.

Wu, H. C., Felis, T., Scholz, D., Giry, C., Kölling, M., Jochum, K. P., and Scheffers, S. R. (2017). Changes to Yucatán Peninsula precipitation associated with salinity and temperature extremes of the Caribbean Sea during the Maya civilization collapse. *Scientific Reports*.

Xu, C. and Stastna, M. (2019). Internal waves in a shear background current: Transition from solitary-wave regime to dispersive-wave regime. *Physical Review Fluids*.

Xu, C., Stastna, M., and Deepwell, D. (2019). Spontaneous instability in internal solitary-like waves. *Physical Review Fluids*, 4(1):1–21.

Zhang, Z. and Moore, J. (2011). New significance test methods for Fourier analysis of geophysical time series. *Nonlinear Processes in Geophysics*, 18(5):643–652.

APPENDICES

Appendix A

Contributions

This thesis is the culmination of a project that has defined my graduate career. It began with a collaboration with Prof. Eduard Reinhardt and the McMaster University Core Scanning Facility (MUCSF), working on quantitative and mathematical aspects of the work in the eastern Yucatan Peninsula. This project has focused heavily on interdisciplinary research. Prof. Marek Stastna and I were the only mathematicians or physicists working on the project which included micropaleontologists, paleontologists and archaeologists. This has provided me with many insights regarding how to effectively communicate my mathematical knowledge to those who do not have a background in it, and how to effectively work with other scientists. Through this project I have also gained many secondary skills, for example becoming a technical SCUBA diver, as well as learning how to take and analyse sediment cores. I have also been to the grand majority of the locations that we have mathematically modelled providing insights that are not possible to attain behind a computer screen.

A.1 Field Work

Since 2014 I have travelled to Tulum, Quintana Roo, Mexico in May and in December often for a week to ten days to complete fieldwork. During this week our partner organization, El Centro Investigador del Sistema Acuífero de Quintana Roo A.C. (CINDAQ) coordinates a science week during which volunteer cave divers travel from around the world to participate in the Mexico Cave Exploration Project which is intended to map and catalogue the extensive cave and cenote systems in the region. For the projects relating to my primary work, these volunteers assisted us in placing various data sensors in locations that I would

not otherwise be able to reach. Through my participation in these scientific collaborations, I learned how to coordinate scientific projects with volunteers from different backgrounds and varying understanding of the technical goals. It was also through these trips that I successfully learned to SCUBA dive at a technical level. This was done through the Global Underwater Explorers (GUE) organization where I attained a Fundamentals (Technical) certification, which will enable me to become certified in cave diving or technical diving. I assisted and participated in many projects for the McMaster University Core Scanning Facility such as sediment trap processing or algae and water sample collection.

A.2 Assisted Projects

This thesis contains three papers of which I was primary author, however during this time I also contributed to other published papers within the (Waterloo) Research group and the MUCSF research group. The following are a list of articles which I contributed to and a brief description of my part in each.

- Kovacs, S.E., Reinhardt, E.G., Stastna, M., Coutino, A., Werner, C., Collins, S.V., Devos, F., and LeMaillot, C. "Hurricane Ingrid and Tropical Storm Hanna's effects on the salinity of the coastal aquifer, Quintana Roo, Mexico". Journal of hydrology 551 (2017): 703-714.

  In this publication I performed all the spectral analysis on the various sensor time-series that were collected. I also performed wavelet analysis to identify dominant frequencies. I wrote and edited the corresponding portions of the text as well.

- Krywy-Janzen, A., Reinhardt, E., McNeill-Jewer, C., Coutino, A., Waltham, B., Stastna, M., Rissolo, D., Meacham, S., and van Hengstum, P.Water-level change recorded in Lake Pac Chen Quintana Roo, "Mexico infers connection with the aquifer and response to Holocene sea-level rise and Classic Maya droughts". J Paleolimnol 62, 373–388 (2019)

  For this publication I performed all the wavelet and spectral analysis that were used. I then wrote and edited the portions of the text that related to these analyses.

- Shaw, J., Stastna, M., Coutino, A., Walter, R.K., and Reinhardt, E.G. "Feature identification in time series data sets". Heliyon 5, no. 5 (2019): e01708.

  In this publication I performed various testing on field data of the new analysis technique developed in this paper. I then wrote and edited the section of the paper using the data we provided.

- McNeill-Jewer, C., Reinhardt, E.G., Krywy-Janzen, A., Coutino, A., Stastna, M., Rissolo, D., and Meacham, S. "Salinity changes during the Maya Terminal Classic droughts documented through calibrated μ-XRF-CS Cl in sediment cores from Quintana Roo". Quaternary Science Reviews. In Review. (2020).

  I performed spectral and wavelet analysis on the sediment core records which highlighted periods of drought during the Mayan Terminal Classical period. I then wrote and edited the corresponding portions of the text.

- McNeill-Jewer, C., Reinhardt, E.G., Coutino, A., Stastna, M., Devos, F., Meacham, S., and LeMaillot, C. "Mixing-induced salinity change in deep coastal Yucatan aquifer caused by hurricanes over the past 4 KY". Prepared for submission. (2020).

  I performed wavelet and gamma analysis of the sediment core records which highlighted regions of enhanced halocline mixing. I then wrote the explanations of the analysis and edited the paper.

In addition to the specific activities outlined above, for all these paper I additionally contributed through discussions of the papers with the other authors as well as personally with the lead author.